Combining in-beam γ-ray and conversion electron spectroscopy

The SAGE spectrometer

Thesis submitted in accordance with the requirements of the University of Liverpool for the degree of Doctor in Philosophy

by

Philippos Papadakis

Oliver Lodge Laboratory

June 2010

To my family and friends;
to all those who stood by me in this endeavour.

And to Prof. Spyros Dedousis
who left us forever on Easter day this year.
Αιωνία η μνήμη.

Σα βγεις στον πηγαιμό για την Ιθάκη,
να εύχεσαι νάναι μακρύς ο δρόμος,
γεμάτος περιπέτειες, γεμάτος γνώσεις.

'Ιθάκη'
Κωνσταντίνος Καβάφης
Greek poet 1863-1933

A physicist is just an atom's way of looking at itself

Niels Bohr
Danish physicist 1885-1962

Abstract

In-beam γ-ray and electron spectrometers are some of the most valuable tools in the study of excited states of nuclei; the latter particularly in the case of very heavy nuclei. However, if used separately they can provide only partial information of the nuclear deexcitation processes and consequently of nuclear structure. This becomes increasingly problematic in heavy nuclei, especially at low transition energies and high multipolarities, where internal conversion competes strongly with γ-ray emission.

To provide the means for a more complete spectroscopy in the superheavy nuclei region the Silicon And GErmanium (SAGE) spectrometer was designed and commissioned by a collaboration from the Universities of Liverpool in the UK and Jyväskylä in Finland and the STFC Daresbury Laboratory.

SAGE combines the JUROGAM II germanium-detector array with a highly-segmented silicon detector and allows efficient cross-coincidence measurements between γ rays and conversion electrons. It uses digital front-end electronics and is coupled with the RITU gas-filled recoil separator and the GREAT focal-plane spectrometer for recoil-decay tagging studies.

Simulations and tests were performed to optimise the spectral response and electron transmission efficiency of SAGE. The spectrometer employs magnetic fields, to transport electrons to the silicon detector, electric fields to reduce the low energy background and a silicon detector coupled with high-gain preamplifiers to measure the electron energies. The electron part of the spectrometer is designed so it does not affect the performance of JUROGAM II.

In this thesis the individual parts of the spectrometer are presented and analysed. The different design criteria and limitations are described in such a way that the reasoning behind every component of SAGE is made clear.

Acknowledgements

The first thank you has to go to my supervisor Prof. Rodi Herzberg for offering me his valuable help, support and advice throughout my PhD. It is greatly appreciated. I would also like to thank Prof. P.J. Nolan for giving me this opportunity at the University of Liverpool and the EPSRC, for providing financial support.

A special thank you goes to Dr. Janne Pakarinen for the endless times he advised and helped me during these three and a half years. Thanks a lot mate!

Thanks to all the students and postdocs in the Department for the great times we've spent together. Special thanks to Pete and Jon for the many inspiring conversations, physics related or not.

To Danielle, Craig, Eddie, Daniel and Lisa for making the trips to Jyväskylä a lot more fun, a big thank you.

Thank you everyone at the Physics Department of the University of Jyväskylä and especially Pauli, Ulrika, Juha and Steffen for all the fun times I had there.

My gratitude to everyone from the SAGE collaboration and especially Janne, Paul and Juha for the long hours they've spent in the cave or the lab working on the setup and doing a lot of the work presented in this thesis.

A big thank you goes to Jim Thornhill, Dave Wells and Dave Seddon for the great work they did on SAGE and especially for explaining to me so many mechanics and electronics related mysteries.

A thank you goes to Dr. Marcus Scheck and Ms. Janet Sampson for proof-reading my thesis and giving me many useful tips.

I would also like to thank Prof. Christos Touramanis for his support and guidance and especially the many interesting discussions inside and outside the Department.

I shouldn't forget Dr. Metaxia Manolopoulou, Prof. Maria Zamani-Valasiadou and Dr. Spyridon Dedousis of the Aristotle University of Thessaloniki for giving me the chance to take my first steps in nuclear structure research and for helping me get this PhD position.

A very special thank you to my housemate and all my Greek and Cypriot friends here

in Liverpool (δεν θα βάλω ονόματα γιατί αν ξεχάσω κάποιον θα μου μουρμουρά μετά) and the Greek-Cypriot community of Liverpool for bringing a piece of home to these foreign lands. And also to all my friends and relatives in Cyprus for the great times I had when I was visiting home and when they were visiting me. The last but most important thank you goes to my family, which I believe deserve to hear it in their own language.

Ευχαριστώ τους γονείς μου για την άμετρή τους υποστήριξη, που ποτέ τους δεν με εμπόδισαν, αλλά αντιθέτως πάντα με ωθούσαν να κάνω αυτό που ήθελα και να βρω το δικό μου δρόμο. Που μου έδωσαν γερές βάσεις και σωστή παιδεία.

Ευχαριστώ κόρη αρφή για ούλλες τες πλάκες, για τες υπέροχες στιγμές που ακόμα περνούμε μαζί. Όσο και αν σε λυπεί, η παρουσία εσένα και του Μάκη έκαναν τα χρόνια του προπτυχιακού πολύ πιο ωραία.

Contents

List of Figures

List of Tables

Abbreviations

AHO	Anisotropic harmonic oscillator
BGO	Bismuth Germanium Oxide
CFD	Constant Fraction Discriminator
CMOS	Complementary Metal Oxide Semiconductor
CPCI CPU	Compact Peripheral Component Interconnect Central Processing Unit
DSSD	Double-sided Silicon Strip detector
EM	Electromagnetic
FET	Field-effect transistor
FPGA	Field-programmable gate array
FWHM	Full Width at Half Maximum
GO-box	Gain and Offset box
GREAT	Gamma Recoil Electron Alpha Tagging focal plane spectrometer
GRT4	Gamma-Ray Tracking 4 channel card
ICC	Internal Conversion Coefficient
ICE	Internal Conversion Electron
LDM	Liquid Drop Model
LGO-card	Liverpool Gain and Offset card
MCA	Multi Channel Analyser
MHO	Modified harmonic oscillator
mic-mac	Microscopic-macroscopic method
MWPC	Multiwire Proportional Counter

PCB ..... Printed Circuit Board

PIN ..... P-type - Intrinsic - N-type semiconductor

RITU ..... Recoil Ion Transport Unit

SAGE ..... Silicon And GErmanium array

SGO-card ..... SmartPET Gain and Offset card

spec-amp ..... Spectroscopy amplifier

TDR ..... Total Data Readout

TDRi card ..... Total Data Readout interface card

TNT2 ..... Tracking Nuclear Treatment card

VHS-ADC ..... Very High Speed Analog-to-Digital converter

Vpp ..... Peak-to-peak voltage

Chapter 1

Introduction

The main motivation of constructing the SAGE spectrometer is the investigation of nuclear properties at the extremes of atomic mass and atomic number, where internal conversion becomes as important as γ-ray emission. SAGE will also allow studies of E0 transitions which proceed via internal conversion only [Pa09a].

One very interesting, yet unanswered question regarding the superheavy nuclei region is the location of the next spherical proton shell closure above Z=82. Some models, like the liquid drop model (see Subsection 2.1.1), predict that nuclei with Z>104 cannot exist as they should fission instantly [Kr00]. According to theoretical predictions where shell structure is considered, a superheavy doubly magic nucleus will have enhanced stability [Ni68, Ni69, Ćw05]. This should lead to the formation of the so-called "island of stability", the precise limits of which are yet unknown [Og00, St06].

The different theoretical approaches give varying estimates on the magic proton and neutron numbers in the superheavy nuclei region. Microscopic-macroscopic models (see Subsection 2.1.3), using various parameterisations of the potential (Yukawa plus-exponential with the Strutinsky shell correction, Woods-Saxon with the Strutinsky shell correction etc), predict the next doubly magic nucleus to have Z=114 and N=184 [Me67, Ni68, Ni69, Mo69, Pa89, Pa91, Mö92, Mö94, Ćw96, Sm97, Ch97, Pa04, Pa05].

Calculations using self-consistent nuclear structure models mainly disagree with the microscopic-macroscopic predictions. Only one potential parameterisation (SkI4) gives agreeable results [Be99] between the two, however, it does so at the cost of an unphysically large spin-orbit interaction. Comparisons of the mean-field calculations [Kr00, Be01] indicate that most of the non-relativistic mean-field models [Ćw96, Ru97, Be99] give Z=124, 126 and N=184 whereas relativistic ones favour Z=120 and N=172 [La96, Ri96, Ru97, Be99, Be03, Af03]. For reviews on theoretical results see e.g. [Be03, Af03, Bü04, De06, Re06, Se06, So07] and references therein. A review of experimental studies relevant to these calculations is made in [He08].

The heaviest nucleus produced experimentally so far is $^{294}_{176}118$ in JINR [Og06]. Only three decay chains of this isotope were observed in the experiment over a period of 45 days. The extremely low production cross-sections of 1 pb or less for superheavy nuclei (such as element 118) [Ar00] make their in-beam spectroscopic study impossible with present day setups.

However the single-particle orbitals determining the stability of these elements can be probed through in-beam spectroscopic studies of lighter nuclei. Theoretical predictions indicate that the single-particle Nilsson orbitals near the Fermi surface in nuclei in the vicinity of the deformed nobelium, originate from spherical single-particle levels above the possible shell gap at Z=114 [He06]. A Nilsson diagram showing how the same orbitals are involved in the creation of the Z=114 and Z=102 shell gaps is presented in Figure 1.1.

^{254}No and its neighbouring nuclei are found to be ideal for spectroscopic studies as they have reasonable cross-sections of the order of 2 μb [He06]. As well as the information obtained from in-beam and focal plane experiments in this region, the masses of three nobelium isotopes were established from direct mass measurements [Bl10] using the Penning-trap mass spectrometer SHIPTRAP [Bl07]. These measurements allow calculation of the binding energy.

In-beam studies, where γ rays and electrons were studied independently, have led to important results on the rotational structure, deformation and stability against

fission of the even-even nuclei ^{254}No [He02, He06] and ^{250}Fm [Ba06, Gr08, Ro09]. γ-ray experiments have also been performed on ^{252}No [He01] ^{246}Fm and ^{248}Fm.

Odd-mass nuclei provide a more sensitive probe into the single-particle structure of superheavy nuclei. These nuclei pose a great experimental challenge when studied in independent conversion electron or γ-ray experiments. Such experiments were performed in the past for ^{253}No (γ-ray spectroscopy [Re04, Re05, Ee06, Pa03a, Mo07, He09] and conversion electron spectroscopy [He02, Pa03a, He09]), for ^{255}Lr [Ke09] and for ^{251}Md [Ch07].

In the spectroscopic studies of ^{253}No a level scheme of two sequences of intra-band E2 transitions with M1 inter-band transitions was established. The highly converted M1 transitions were not observed in the first γ-ray experiments [Re04, Re05] but were observed in a conversion electron study [He02, He09]. In the higher statistics γ-ray experiments that followed, M1 transitions with higher transition energy were observed but the low energy transitions still remained undetected. An in-beam experiment that would simultaneously study both conversion electrons and γ rays would yield a more complete level scheme.

In the case of ^{251}Md the odd proton ground state is predicted to occupy the $\pi[521]1/2^-$ orbital stemming directly from the spherical $2f_{5/2}$ subshell, with excited states derived from the spherical $1i_{13/2}$, $1h_{9/2}$ and $2f_{7/2}$ orbitals. The spin-orbit splitting between the $2f_{5/2}$ and $2f_{7/2}$ orbitals is critical for the creation of a possible spherical shell closure at Z=114 (see Figure 1.1).

Establishing the relative position of the $2f_{5/2}$ and $2f_{7/2}$ orbitals provides information as to whether the theoretical prediction of a closed spherical shell at Z=114 is true and helps to locate the "island of stability". This can be done either through studies of single-particle excitations in odd-mass nuclei described above or multiparticle-multihole excitations in even-even nuclei, where the latter are considered to populate states involving the $2f_{5/2}$ orbital.

The configurations of the experimentally observed bands can be deduced from the B(M1)/B(E2) reduced transition probabilities ratios. These are sensitive to the

g-factors of the orbitals involved and according to the geometric model are [Bo75]:

$$\frac{B(M1)}{B(E2)} \propto \frac{K^2(g_K - g_R)^2}{{Q_o}^2}, \tag{1.1}$$

where g_R and g_K are the gyromagnetic ratios of the rotating core and the single-particle respectively (see Section 2.3), K is the projection of the total angular momentum on the nuclear symmetry axis (see Section 2.2) and Q_o is the intrinsic electrical quadrupole moment. B(M1)/B(E2) are easily measured if the electrons and γ rays are observed in the same experiment to provide accurate branching ratios.

Another region of interest for the SAGE spectrometer can be found in the light lead and mercury region. Here the deformed multiparticle-multihole structures intrude down in energy close to the spherical ground state, when approaching the neutron mid-shell at N=104. A triplet of low-lying 0^+ states associated with different macroscopic shapes is observed. The properties of these low-lying 0^+ states and the inter-band transitions between the same spin-parity states of rotational oblate and prolate bands can be investigated through simultaneous conversion electron and γ-ray spectroscopy [An00, Pa07].

Nuclei in this region have been studied in the past in α-decay fine structure measurements, in-beam γ-ray studies and in some cases internal conversion electron (ICE) measurements. Simultaneous γ-ray and ICE experiments performed with SAGE will measure the conversion electron strengths of the inter-band transitions (oblate to prolate) and the location and feeding of the low-lying 0^+ states. The measurements of the E0 matrix elements in neutron mid-shell isotopes of lead and mercury will provide direct information on configuration mixing and shape changes in these nuclei.

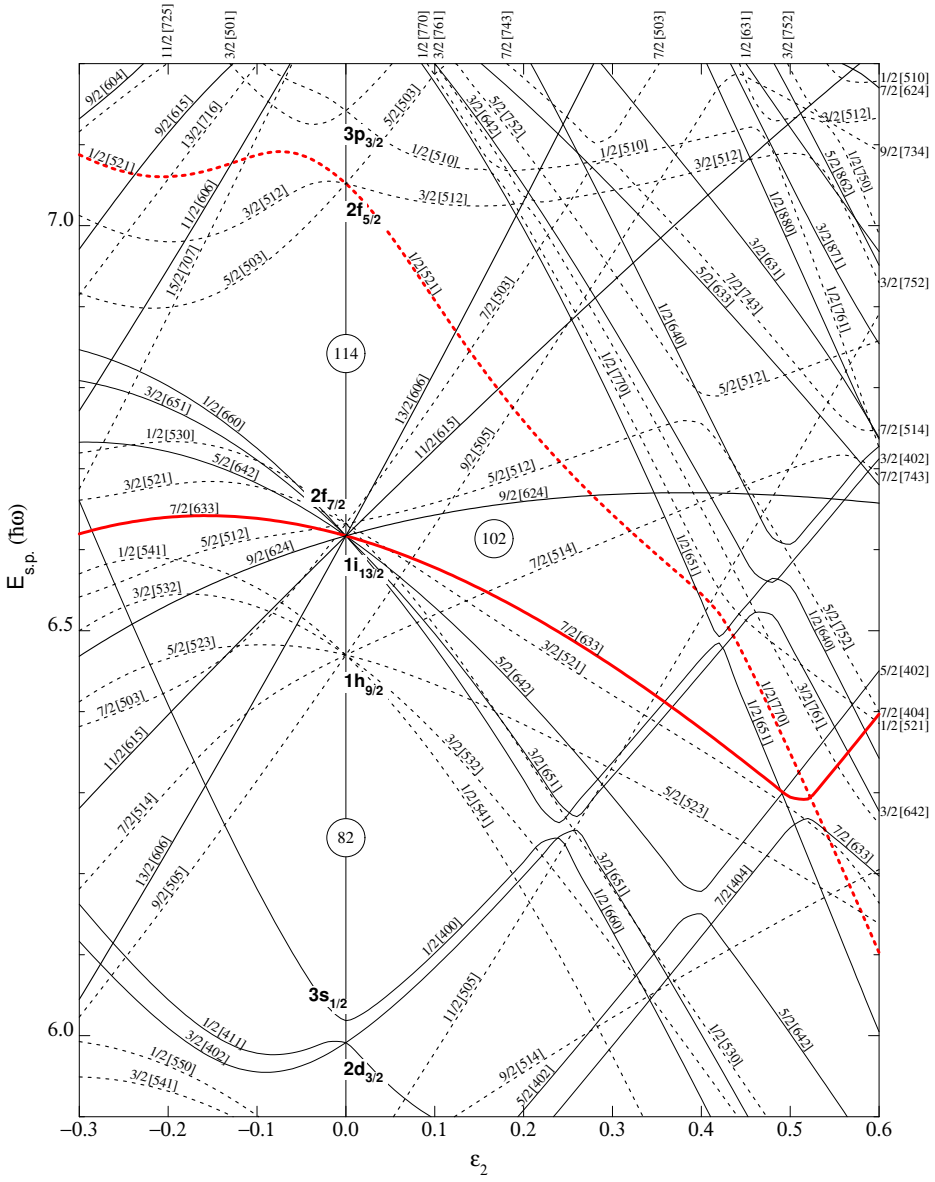

Figure 1.1: Nilsson level diagram for protons with Z≥82 ($\epsilon_4 = \epsilon_2^2/6$), taken from [Fi96]. Calculations are made within the cranked Nilsson-Strutinsky framework as described in [Be85].

Chapter 2

Theoretical framework

2.1 Nuclear models

2.1.1 The liquid drop model (LDM)

One of the first models to successfully describe nuclear properties was the LDM, introduced in [Bo37]. Observations that the nuclear forces saturate and the nucleus has low compressibility and a well defined surface, led to the treatment of the nucleus as an incompressible nuclear fluid with the nucleons held together by the strong interaction [He94].

The LDM parametrises the energy using a volume term, a surface term and a Coulomb interaction term, based on the concept of a charged nuclear fluid. Including an isospin and a pairing term derived from the shell model, this leads to the Bethe-Weizsäcker mass equation [Kr88]:

$$BE(A,Z) = \alpha_v A - \alpha_s A^{2/3} - \alpha_c Z(Z-1)A^{-1/3} - \alpha_i (A-2Z)^2 A^{-1} + \delta. \qquad (2.1)$$

The coefficients α_v, α_s, α_c and α_i refer to the volume, surface, Coulomb and isospin terms respectively. δ is the pairing energy term and it is $+\alpha_p A^{-3/4}$ for even-even nuclei, $-\alpha_p A^{-3/4}$ for odd-odd nuclei and zero for odd A nuclei. The LDM does not make any predictions on the values of the coefficients included in the mass formula but they are obtained by fitting Equation 2.1 to experimental data.

The LDM successfully predicts fission (not for superheavy nuclei), fusion and α decay. Because in the LDM the coefficients are fitted phenomenologically, the model describes well the average trends of nuclear binding energies. For the same reason though, the predictions made using the LDM have large uncertainties when extrapolating to exotic nuclei [Be03]. Additionally, because the model does not take into account shell structure, it fails to replicate many observables like the magic numbers, the discontinuities in neutron binding energies etc.

One of the major predicaments of the LDM is its inability to calculate fission barriers for the heaviest elements. According to this model elements with Z>104 should fission instantly due to their large electric charge [Kr00]. In these nuclei stability arises solely due to shell effects. In order to do any realistic calculations in the superheavy nuclei region, shell structure must be taken into account.

2.1.2 The spherical shell model

The shell model [Ma49] considers the nucleons to move in almost unperturbed single-particle orbits, due to the Pauli exclusion principle, within the uniform average potential created by the nucleons themselves. Different approaches can be taken when describing the nuclear potential such as the square well, Gaussian well, exponential well, Yukawa well, harmonic oscillator and Wood-Saxon (see Figure 2.1). In addition to the nuclear potential a spin-orbit term is introduced to the Hamiltonian in order to express the interaction between the intrinsic spin and the orbital momentum and also an $\hat{l}^2$ term, where l is the orbital angular momentum, in order to flatten the effective radial shape of the potential.

The shell model reproduces the experimentally observed shell gabs, the so called magic numbers, at proton and neutron numbers 8, 20, 28, 50 and 82. For neutrons, 126 is a magic number as well. It also explains spin and magnetic moments of nuclei close to the magic numbers. On the other hand it does not explain some of the bulk properties that are successfully described by the LDM.

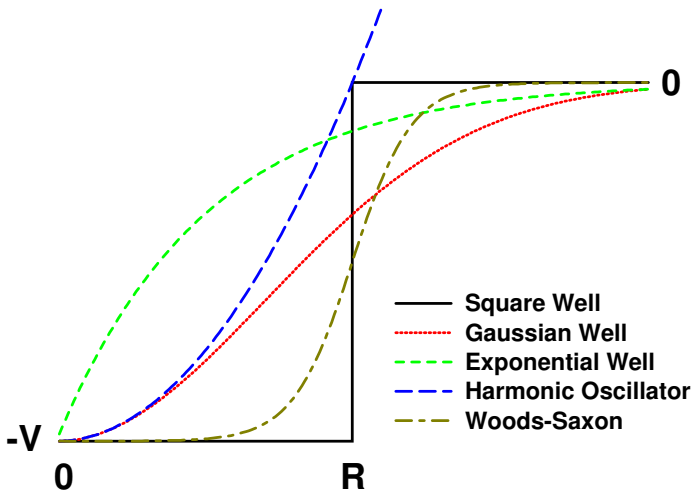

Figure 2.1: Some of the potential wells that can be used to describe the nucleus. Figure adapted from [Pa10].

2.1.3 The Strutinsky shell correction

By combining the macroscopic LDM with microscopic shell corrections the much more precise microscopic-macroscopic (mic-mac) method is produced. Considering that a nuclear property, such as the total ground-state energy, consists of a smooth and an oscillatory part as shown in Figure 2.2, then in order to calculate it correctly both these parts need to be considered. In the case of the mic-mac method the Strutinsky shell correction [St67, St68] is used to extract the oscillatory part of a nuclear property and then combine it with the smooth part derived using a macroscopic model (e.g. LDM).

Using the Strutinsky procedure the energy is written as:

$$E = E_{LDM} + E_{SHELL}, \tag{2.2}$$

where

$$E_{SHELL} = \sum_{i=1}^{A} \epsilon_1(\delta) - \tilde{E}_{SHELL}, \tag{2.3}$$

with $\tilde{E}_{SHELL}$ used to subtract the part of the energy that was already included in E_{LDM}. $\epsilon_1(\delta)$ denotes the eigenvalues of the Nilsson potential and δ is a deformation

parameter [He94].

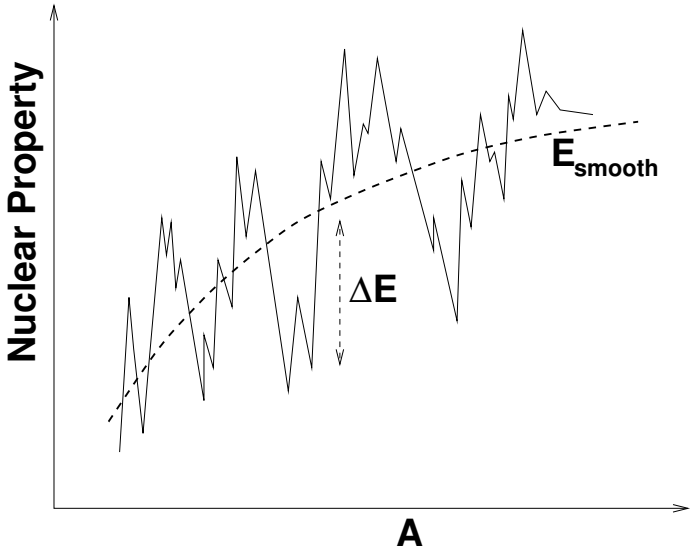

Figure 2.2: Plot of a nuclear property showing the smooth and oscillatory parts. Figure adapted from [Pa10].

One important outcome of the mic-mac method, relevant to this work, is the prediction of enhanced stability against fission of superheavy elements. This is shown in Figure 2.3 where fission barriers for uranium, californium and hassium were calculated with and without taking shell structure into account. According to the LDM calculations hassium should be completely unbound and have a half-life of about 10^{-19} s. On the other hand when shell-model corrections are applied the fission barrier increases dramatically and the calculated half-life of the element increases by several orders of magnitude, even up to 10^{15} s for ^{292}Hs.

2.1.4 The deformed shell model

Nuclei in the vicinity of closed shells are near spherical and can be described very well by a spherical potential. However when moving away from close shells sphericity is no longer valid and strong evidence, such as the existence of rotational bands and large intrinsic quadrupole moments, show that nuclei are deformed in the regions between

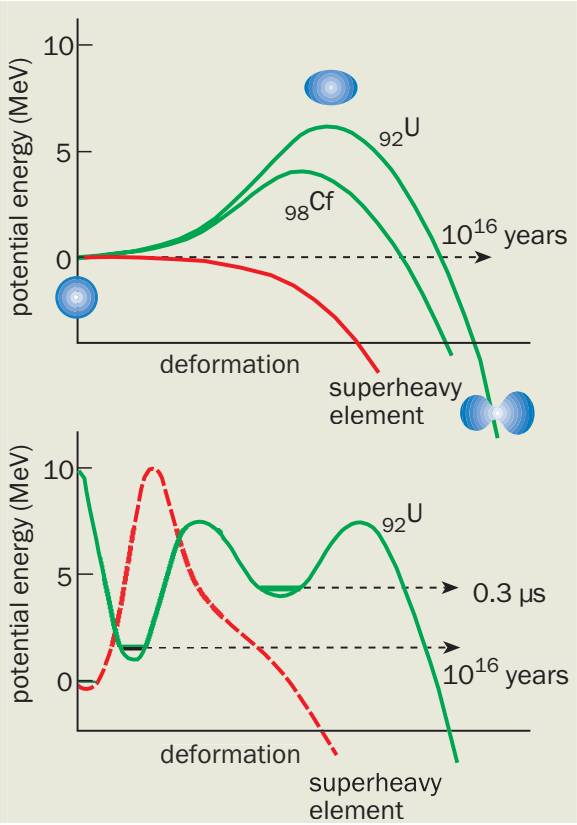

Figure 2.3: Fission barriers for U, Cf and Hs calculated with the LDM (top) and with the mic-mac method (bottom) [Og04].

the closed shells.

Deformed nuclei cannot be described within the spherical shell model, but a deformed potential needs to be used in the Hamiltonian. The simplest Hamiltonian that can be adopted employs the anisotropic harmonic oscillator (AHO) potential:

$$H_{def} = -\frac{\hbar^2}{2m} + \frac{1}{2}m\left(\omega_x^2 x^2 + \omega_y^2 y^2 + \omega_z^2 z^2\right), \tag{2.4}$$

where ω_i defines the frequency of the potential at the i^{th} direction. For axially symmetric nuclei $\omega_x = \omega_y = \omega_\perp$, with $\omega_\perp$ being the frequency perpendicular to the symmetry axis z [He94].

The eigenstates of the AHO are conventionally labelled using the asymptotic Nils-

son quantum numbers:

$$[Nn_z\Lambda]\Omega^\pi, \tag{2.5}$$

where N is the total number of oscillator quanta, n_z the number of oscillator quanta along the symmetry axis z, Λ is the projection of the orbital angular momentum l onto the symmetry axis and takes values $\Lambda = N, N-2...1$ or 0, Σ is the projection of spin $s = \pm\frac{1}{2}$ on the symmetry axis, $\Omega = \Lambda \pm \Sigma$ is the projection of the total angular momentum j onto the symmetry axis (see Figure 2.4) and π is the parity of the level.

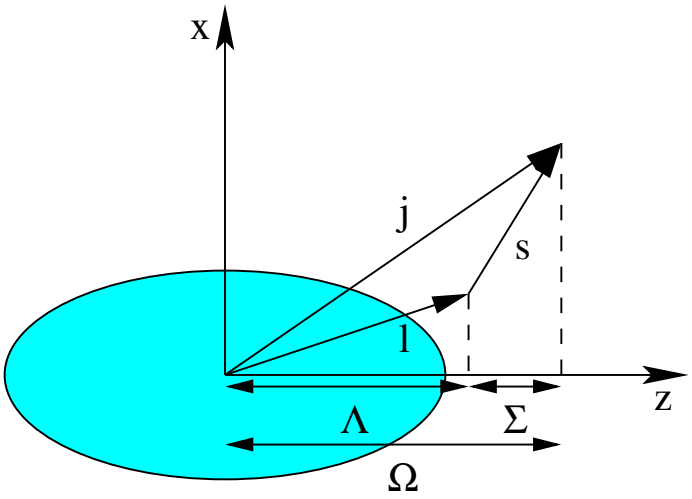

Figure 2.4: Schematic representation of the coupling of orbital angular momentum and spin in a deformed nucleus.

Nilsson [Ni55] modified the AHO potential to include a spin-orbit term to allow derivation of a more realistic single-particle spectrum. He also added an $\hat{l}^2$ term to flatten the radial shape of the potential. This potential is called Nilsson potential or modified harmonic oscillator (MHO) potential. The Nilsson Hamiltonian is:

$$H_{Nilsson} = \underbrace{\hbar\omega_0(\delta)\left(-\frac{1}{2}\Delta' + \frac{r'^2}{2} - \beta r'^2 Y_{20}(\hat{r}')\right)}_{AHO} - k\hbar\,\mathring{\omega}_0\left[2\hat{l}\cdot\hat{s} + \mu\left(\hat{l}^2 - \langle\hat{l}^2\rangle_N\right)\right], \tag{2.6}$$

where $\omega_0(\delta)$ arises when one considers a deformation dependent oscillator length with

the deformation parameter δ, $\omega_0(\delta) = \mathring{\omega}_0 \left(1 + \frac{2}{3}\delta^2\right)$, $\beta = \frac{1}{3}\sqrt{16\pi/5}\delta$, $2k$ is the spin-orbit strength and $k\mu$ the $\hat{l}^2$ orbit energy shift [He94].

Other potential parametrisations, such as the deformed Woods-Saxon potential can be used instead of the MHO to calculate properties of deformed nuclei. Different potentials might work better in different areas of the nuclear chart but in general the potential to be used is a matter of personal preference.

As mentioned above for the case of superheavy elements shell effects lead to increased stability. Especially in the case of the superheavy nuclei that are far from the spherical closed shells stability arises solely from deformation. An example of this would be the deformed shell gap at the region of nobelium (Z=102) [He06].

To illustrate the effect of deformation on the magic numbers a single-particle level spectrum plotted as a function of quadrupole deformation, ϵ_2, is shown in Figure 2.5. To keep the figure as simple as possible the axially deformed harmonic oscillator potential without the use of a spin-orbit and an $\hat{l}^2$ term was used in the calculations. Because these terms were omitted, the model does not reproduce the correct magic numbers but is still good enough in order to illustrate the effect of deformation on them. The quadrupole deformation is defined as $\epsilon_2 = (\omega_\perp - \omega_z)/\omega_0$, with $\omega_0 = \frac{1}{3}(2\omega_\perp + \omega_z)$.

From Figure 2.5 it becomes obvious that with increasing deformation single-particle levels shift forming shells gabs at different proton or neutron numbers than in the case of the spherical nucleus. This explains the presence of the deformed proton shell at Z=102 which should not exist if the nucleus was spherical. In more realistic calculations the produced single-particle spectra are more complicated but can reproduce the observed shell gabs accurately. An example of this is the calculations made within the cranked Nilsson-Strutinsky framework presented in Figure 1.1. In this figure the deformed shell gab in the vicinity of nobelium can be clearly seen.

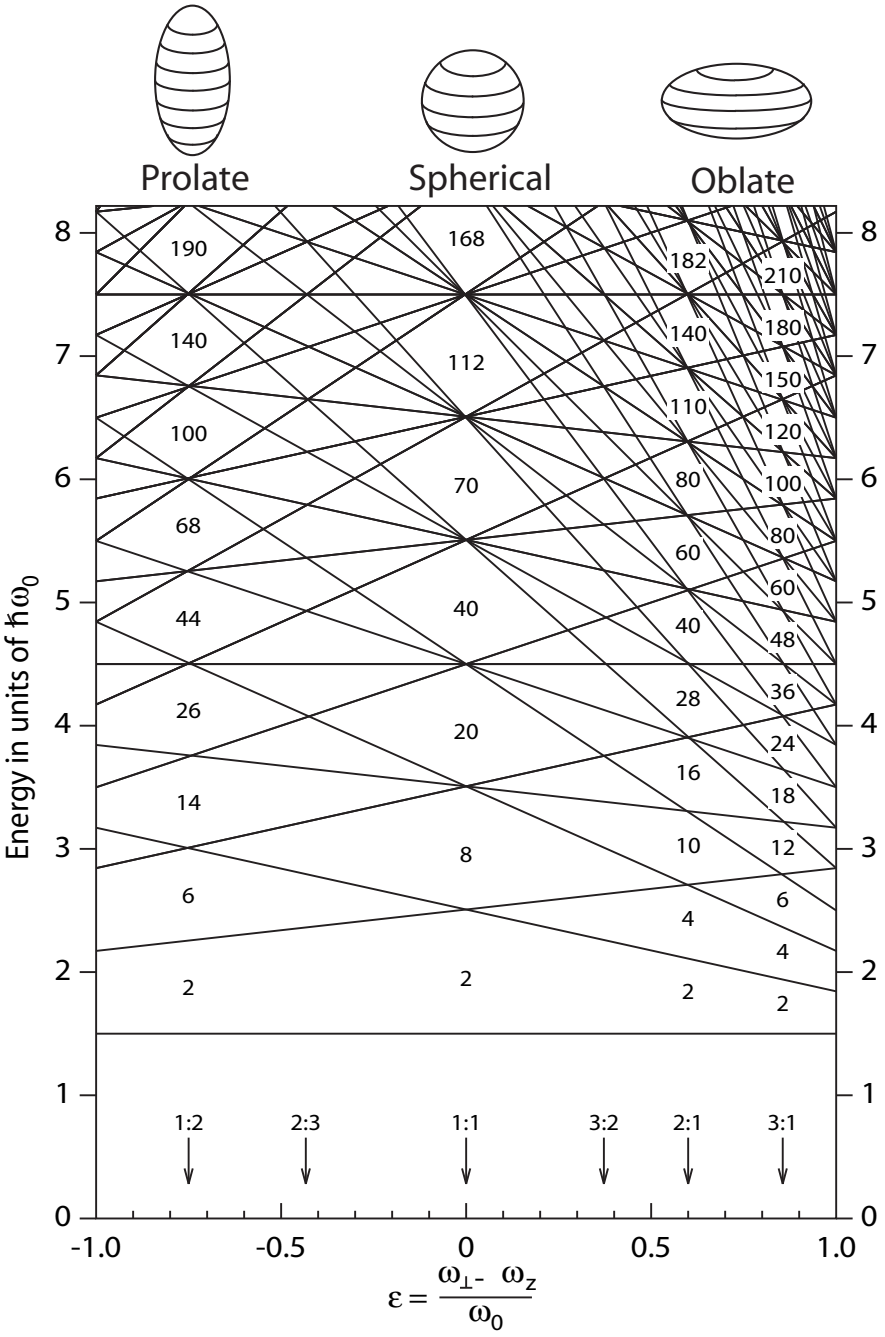

Figure 2.5: Single-particle level spectrum calculated using the axially deformed harmonic oscillator potential without the use of a spin-orbit and an $\hat{l}^2$ term. The arrows indicate deformations corresponding to the ratios of $\omega_\perp : \omega_z = 1:2, 2:3, 1:1,$ $3:2, 2:1$ and $3:1$. The figure is adapted from [Wo92].

2.2 Nuclear rotation

In the case of spherical nuclei it is impossible to distinguish their orientation, due to axial symmetry, so rotation is forbidden. Deformation though introduces an anisotropy allowing the definition of orientation and making nuclear rotation possible.

The nucleus can be described as a core surrounded by the valence nucleons with the axis of rotation perpendicular to the symmetry axis. The total angular momentum, I, of the rotating nucleus is defined as the sum of the collective angular momentum, R, generated by the collective rotation of the nucleus and the intrinsic angular momentum, J, created by the motion of valence nucleons,

$$I = R + J. \tag{2.7}$$

Figure 2.6 shows how the collective angular momentum couples to the total intrinsic angular momentum produced by two valence single particles with intrinsic angular momenta j_1 and j_2.

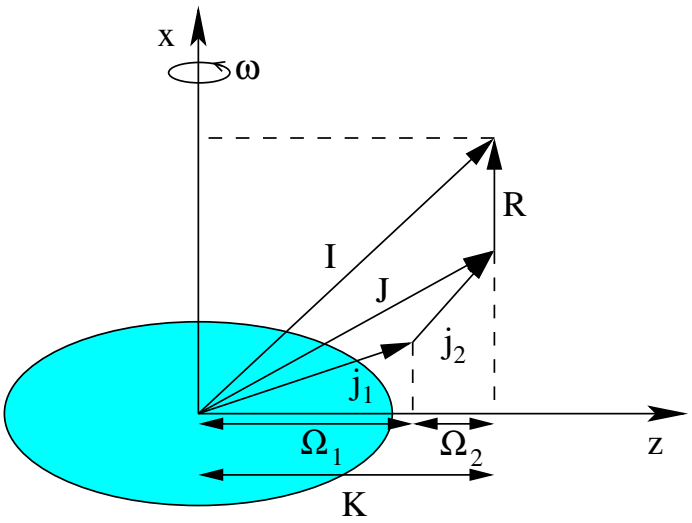

Figure 2.6: Coupling of the collective and single-particle angular momenta. ω is the rotational frequency around the rotation axis x and z is the symmetry axis.

The signature quantum number, r, is defined in the case of nuclear rotation.

Signature relates with the $\mathcal{R}$ invariance of the system which arises from the invariance of the intrinsic Hamiltonian to rotations of 180° about any axis perpendicular to the symmetry axis [Bo75].

Rotational bands can be separated into three categories:

- $K = 0$ bands

  In this case the allowed values of signature are:

  $$r = (-1)^I, \tag{2.8}$$

  which gives the selection rules:

  $$I = 0, 2, 4, ... \text{ for } K = 0 \text{ and } r = +1, \tag{2.9}$$

  $$I = 1, 3, 5, ... \text{ for } K = 0 \text{ and } r = -1. \tag{2.10}$$

  This leads to two rotational bands with opposite values of signature, called signature partner bands. The levels within each band are separated by $2\hbar$ and their energy is given by:

  $$E_{K=0} = \frac{\hbar^2}{2\mathcal{J}^{(0)}} I(I+1), \tag{2.11}$$

  where $\mathcal{J}^{(0)}$ is the rigid body static moment of inertia.

- $K \neq 0$ bands

  In the case of $K \neq 0$ signature is defined as:

  $$r = (-1)^{I+K} \tag{2.12}$$

  and changes sign within a band for alternate spin values.

  For $K \neq 0$ bands particle-rotor coupling occurs which is described by the rotation of the nuclear core (rotor) coupled to the single particles in a way analogous to the classical Coriolis force.

In the case of large deformation or strong coupling, Deformation Aligned (DAL) scheme, K is a good quantum number and there is little signature splitting. In this case the rotational band is defined by:

$$I = K, K+1, K+2, ..., \tag{2.13}$$

with energies:

$$E_{DAL} = \frac{\hbar^2}{2\mathcal{J}^{(0)}} \left[I(I+1) - K^2 \right]. \tag{2.14}$$

When the nucleus is weakly deformed or the particle rotation is fast, the coupling is weak and K is no longer a good quantum number. This case is called Rotation Aligned (RAL) and has the nucleonic angular momentum j as a good quantum number. The band members have spins defined by:

$$I = j, j+2, j+4, ... \tag{2.15}$$

and energies:

$$E_{RAL} = \frac{\hbar^2}{2\mathcal{J}^{(0)}} (I - j_x)(I - j_x + 1). \tag{2.16}$$

- $K = \frac{1}{2}$ bands

  In this case the Coriolis force has only a diagonal contribution to the energy. The energy is defined as:

$$E = \frac{\hbar^2}{2\mathcal{J}^{(0)}} \left[I(I+1) + \alpha(-1)^{I+\frac{1}{2}} \left(I + \frac{1}{2} \right) \right], \tag{2.17}$$

  with α the decoupling parameter. Signature is now:

$$r = (-1)^{I+\frac{1}{2}} \tag{2.18}$$

  and the spins of the band states are:

$$I = \frac{1}{2}, \frac{3}{2}, \frac{5}{2}, ... \ . \tag{2.19}$$

  Because the energy is in this case proportional to $\left(I + \frac{(1+r\alpha)}{2} \right)^2$ the spins of the signature partner bands are displaced in different directions along the momentum axis. Thus if the decoupling parameter is numerically larger than unity this displacement leads to inversion of the normal spin sequence [Bo75, Pa10].

2.3 Magnetic dipole moment and gyromagnetic ratios

Measurements of the magnetic dipole moments and the gyromagnetic ratios (g-factors) of a nucleus and their comparison with theoretical predictions yield useful information on nuclear structure.

The magnetic moment of a single nucleon consists of an orbital and a spin part [Bo69]:

$$\vec{\mu} = g_l \vec{l} + g_s \vec{s}, \tag{2.20}$$

where g_l is the orbital g-factor and g_s the spin g-factor in units of nuclear magnetons ($\mu_N = e\hbar/(2m_p) = 5.0508 \times 10^{-27} JT^{-1}$). The bare orbital g-factors are g_l^p=1 μ_N for protons and g_l^n=0 μ_N for neutrons. For a free nucleon the spin g-factors are g_s^p=5.58 μ_N and g_s^n=-3.82 μ_N for the proton and neutron respectively, whereas s=1/2 for fermions. The spin g-factor for a bound nucleon can vary significantly from the values above, but generally g_s^p is positive and g_s^n negative.

The magnetic dipole moment of a nucleus is defined as [Ej89]:

$$\mu(I) = \left[g_R I + (g_K - g_R) \frac{K^2}{I+1} \right] \mu_N, \tag{2.21}$$

where g_K arises from the single particle contribution in the nuclear magnetic dipole moment due to electric currents generated by the nuclear motion and g_R refers to the collective rotation of the nucleus. g_R is usually approximated by [Ej89]:

$$g_R \simeq k \frac{Z}{A}, \tag{2.22}$$

where the quenching factor k is roughly 1.

In an odd nucleus (e.g. ^{251}Md described earlier) the B(M1)/B(E2) ratios can be used to determine the g_K factor (Equation 1.1). By comparing this factor with theoretical calculations within a certain nuclear model the single-particle configuration can be assigned.

As an example of this process the assignment of the two-quasiparticle configuration of the $K^\pi = 8^-$ isomer in the even-even nucleus ^{250}Fm taken from [Ro09]

is briefly explained. B(M1)/B(E2) ratios are produced for all the observed transitions from the measured intensities. These values are also theoretically calculated from Equations 2.28 and 2.29 by hand or using the program BM1BM2 [Pa09b] that is based on [Dö83, Dö87]. In this approximation an intrinsic representation of the radiative multipole operators based on the rotor-plus-particle coupling concept is used to calculate electromagnetic transition amplitudes with cranking states.

The intrinsic electric quadrupole moment used in the calculations is taken as Q_0=12.6 eb and the quenching factor in Formula 2.22 as k=1 or k=0.8. k=0.8 was used because rotational nuclei with 140≤A≤200 are found to have g_R values consistently lower than $g_R = Z/A$ [Bo69].

The g_K values of the single-particle states involved are calculated with the *swbeta* program [Ćw87]. This program uses a Hamiltonian including an axially deformed Woods-Saxon potential, the spin-orbit interaction and the Coulomb potential for protons to calculate single-particle energies, wave functions, LDM constants, effective barriers for the unbound states, single-particle quadrupole moments and g-factors. The single-particle g_K values computed with the program are combined using the generalised Landé formula (Equation 2.23) to give the g_K value of the two-quasiparticle excitations, labled as g_J:

$$g_J = \frac{1}{2}(g_1 + g_2) + \frac{1}{2}(g_1 - g_2)\left[\frac{j_1(j_1+1) - j_2(j_2+1)}{J(J+1)}\right], \tag{2.23}$$

where g_1 and g_2 are the g_K values of the two quasi-particle states and j_1 and j_2 their spins [Kr88].

For ^{250}Fm the comparison of the experimental with theoretical results is made in Figure 2.7. The intensity ratios could be experimentally determined for the 16^-, 15^- and 14^- states. The figure shows the comparison of theory and experiment for all three of these states. Within uncertainties a two neutron, $\frac{7}{2}^+[624]_\nu \otimes \frac{9}{2}^-[734]_\nu$, and two proton, $\frac{7}{2}^-[514]_\pi \otimes \frac{9}{2}^+[624]_\pi$, configurations can be assigned to this band. The two neutron configuration is favoured by both the quenched and unquenched results, so it can be concluded that the $K^\pi = 8^-$ band is formed by the two neutron configuration.

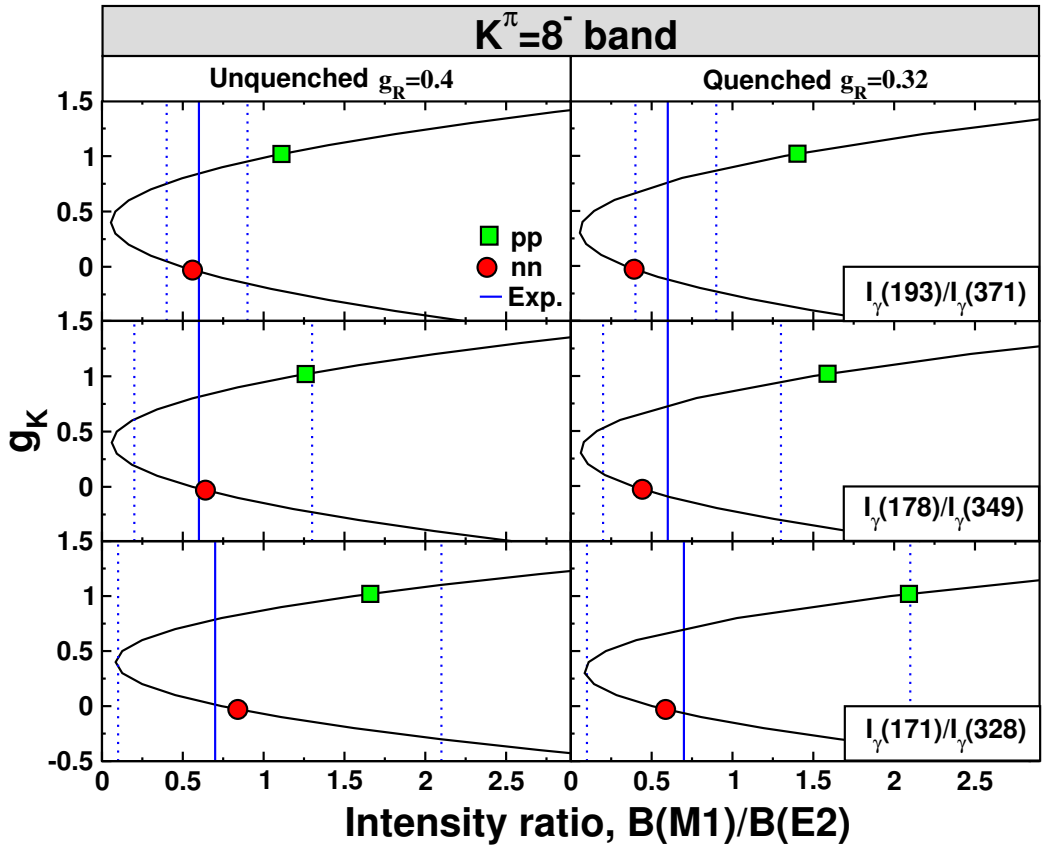

Figure 2.7: Relation between the intensity ratio, B(M1)/B(E2), and the g_K factor for the 16^-, 15^- and 14^- states of the $K^\pi = 8^-$ isomer of ^{250}Fm. The experimental results (blue lines and dotted lines their errors) are compared with the two neutron $\frac{7}{2}^+[624]_\nu \otimes \frac{9}{2}^-[734]_\nu$ configuration (red circles) and the two proton $\frac{7}{2}^-[514]_\pi \otimes \frac{9}{2}^+[624]_\pi$ configuration (green squares). The unquenched and quenched values are as explained in the text. Figure adapted from [Ro09].

2.4 Electromagnetic transitions

SAGE will be used in experiments employing fusion evaporation reactions. In a fusion reaction the projectile and target nuclei interact strongly forming a compound nucleus in an exited state with a lifetime between 10^{-19} and 10^{-16} s. The compound nucleus releases its excess energy and angular momentum by evaporation of particles and emission of γ rays. Depending on its mass the decay can progress through different channels as described in Figure 2.8.

In lighter systems the compound nucleus decays to a particle-stable evaporation residue through light-particle emission, namely neutron, proton and α-particle emission with fission increasingly competing at heavier systems [Fr96].

After the internal energy becomes less than the particle emission threshold the dominant mode of deexcitation is via electromagnetic transitions. The nucleus loses energy rapidly mainly by the emission of E1 γ rays (about 10^{-15} s after particle evaporation). After roughly 10^{-12} s it reaches the yrast line [Gr67] and starts decaying towards the ground state which it reaches after about 10^{-9} s. In some cases the nucleus might populate an isomeric state[1] and thus reach the ground state after a longer time period.

Electromagnetic transitions can proceed via several mechanisms: (1) γ-ray emission, (2) Internal conversion and (3) Internal pair formation (alternatively called electron-positron pair emission and only possible if the excitation energy is above 1.02 MeV). The first two will be described, as they are the processes studied with SAGE. Internal pair formation is not discussed here, but can be found in [Ro49, Wi66].

2.4.1 γ-ray emission

In the process of γ-ray emission a transition of multipolarity L is allowed between two states of angular momenta (I_i, I_f) and parities (π_i, π_f), where $_i$ denotes the initial and $_f$ the final states, if it obeys a set of selection rules [Kr88, Mo66].

[1] Isomeric is an excited state whose half-life is long compared to most other excited states [Wa99].

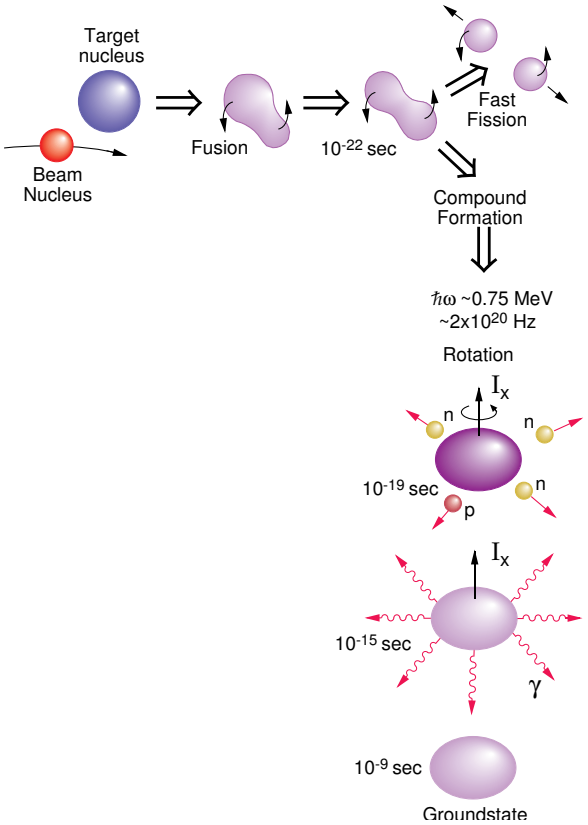

Figure 2.8: Production and decay mechanisms of a compound nucleus [Pa10].

- Conservation of angular momentum:

$$\vec{I_i} = \vec{I_f} + \vec{L} \tag{2.24}$$

- Triangle rule:

$$\mid I_i - I_f \mid \leq L \leq I_i + I_f \tag{2.25}$$

- Parity rule:

$$\begin{aligned} \Delta\pi(EL) &\equiv \pi_i \cdot \pi_f = (-1)^L \\ \Delta\pi(ML) &\equiv \pi_i \cdot \pi_f = (-1)^{L+1} \end{aligned} \tag{2.26}$$

The above apply for all but monopole transitions. M0 transitions do not exist [Ku93] and E0 transitions can only proceed via internal conversion (see Subsection 2.4.2).

Another important observable is the transition probability. This is especially useful when angular correlations or linear polarisation measurements cannot be used for the determination of the type or multipole order of a transition (see for example [Mo76] for a detailed description of these methods). The total transition probability, $T(\sigma L)$, is a function of the reduced transition probability, $B(\sigma L)$, and for the first five values of L they are related as shown in Table 2.1 [Bo69, Mo76].

Table 2.1: Relation between $T(\sigma L)$ and $B(\sigma L)$. E is in MeV, $T(\sigma L)$ in s^{-1}, $B(EL)$ in e^2fm^{2L} and $B(ML)$ is in units of $\mu_N^2 fm^{2L-2}$.

$T(E1)$	1.59×10^{15}	E^3	$B(E1)$
$T(E2)$	1.22×10^{9}	E^5	$B(E2)$
$T(E3)$	5.67×10^{2}	E^7	$B(E3)$
$T(E4)$	1.69×10^{-4}	E^9	$B(E4)$
$T(E5)$	3.43×10^{-9}	E^{11}	$B(E5)$
$T(M1)$	1.76×10^{13}	E^3	$B(M1)$
$T(M2)$	1.35×10^{7}	E^5	$B(M2)$
$T(M3)$	6.28×10^{0}	E^7	$B(M3)$
$T(M4)$	1.87×10^{-6}	E^9	$B(M4)$
$T(M5)$	3.79×10^{-13}	E^{11}	$B(M5)$

The reduced transition probability and decay half-life (τ) are related as [Bo69]:

$$B(\sigma L) \propto (E^{2L+1} \cdot \tau)^{-1}. \tag{2.27}$$

Rough estimates of transition probabilities (called Weisskopf estimates) are derived in [We51]. In [Mo76] these are repeated together with estimates for the reduced transition probabilities and tabulated values for the first five electric and magnetic transitions as shown in Table 2.2.

Table 2.2: The Weisskopf estimates of $T(\sigma L)$ and $B(\sigma L)$. E is in MeV, $T(\sigma L)$ in s^{-1}, $B(EL)$ in e^2fm^{2L} and $B(ML)$ is in units of $\mu_N^2 fm^{2L-2}$.

σL	$B^W(\sigma L)$	$T^W(\sigma L)$
E1	$6.45 \times 10^{-2} A^{2/3}$	$1.02 \times 10^{14} A^{2/3} E^3$
E2	$5.94 \times 10^{-2} A^{4/3}$	$7.23 \times 10^{7} A^{4/3} E^5$
E3	$5.94 \times 10^{-2} A^{2}$	$3.37 \times 10^{1} A^{2} E^7$
E4	$6.29 \times 10^{-2} A^{8/3}$	$1.06 \times 10^{-5} A^{8/3} E^9$
E5	$6.93 \times 10^{-2} A^{10/3}$	$2.38 \times 10^{-10} A^{10/3} E^{11}$
M1	1.79	$3.12 \times 10^{13} E^3$
M2	$1.65 A^{2/3}$	$2.21 \times 10^{7} A^{2/3} E^5$
M3	$1.65 A^{4/3}$	$1.03 \times 10^{1} A^{4/3} E^7$
M4	$1.75 A^{2}$	$3.25 \times 10^{-6} A^{2} E^9$
M5	$1.92 A^{8/3}$	$7.29 \times 10^{-13} A^{8/3} E^{11}$

Equation 1.1 from Chapter 1 comes from the reduced transition probabilities as calculated within the geometric model [Bo75]. These are expressed as:

$$B(M1; KI_i \rightarrow KI_f) = \frac{3}{4\pi} \left(\frac{e\hbar}{2Mc} \right)^2 (g_K - g_R)^2 K^2 \langle I_i K 10 \mid I_f K \rangle^2, \tag{2.28}$$

for M1 transitions and

$$B(E2; KI_i \rightarrow KI_f) = \frac{5}{16\pi} e^2 {Q_0}^2 \langle I_i K 20 \mid I_f K \rangle^2 \tag{2.29}$$

for E2 transitions.

For a rotational band with a quantum number K≠1/2 the spectroscopic electric quadrupole moment can be described as [Ej89]:

$$Q(I) = \frac{3K^2 - I(I+1)}{(I+1)(2I+3)} e Q_o(K) \tag{2.30}$$

For the same band the magnetic dipole moment is defined as in Equation 2.21.

2.4.2 E0 transitions

The E0 transitions are the only allowed transitions between two 0^+ states. They do not change the angular momentum of the nucleus but alter the nuclear surface [Mo76]. E0 components are also observed in transitions between states of the same spin and parity in competition with M1 and E2 components.

E0 transitions mainly proceed through internal conversion. The photon has unit intrinsic spin; so a transition between two states with zero spins and even parities through the emission of a single γ ray is strictly forbidden. Additionally it can proceed through the emission of two γ rays, double internal conversion or simultaneous γ-ray and electron emission. However, all these processes are orders of magnitude less likely to happen than internal conversion. E0 can also take place through internal pair formation if that is energetically allowed [Go66].

The absolute transition probability, W(E0), depends on the electronic factor and the monopole transition strength. The electronic factor, Ω, is not completely independent of nuclear properties as it is described by the electron wave functions within the nucleus. This is the case because the monopole interaction exists only while the electron is within the nuclear charge distribution [Ch56]. The monopole transition strength ρ depends on the nuclear radius ($R \simeq 1.2A^{1/3}$) and the position vector of each proton, $\rho \approx \sum_p \left\langle r_p^2/R \right\rangle$ [Go66].

$$W(E0) = \frac{1}{\tau(E0)} = \rho^2(E0) \times [\Omega_{ic}(E0) + \Omega_{\pi}(E0)], \tag{2.31}$$

where τ(E0) is the partial mean life of the initial state for E0 decay and Ω_{ic}E(0) and Ω_{π}E(0) the electronic factors for internal conversion emission and electron-positron pair emission, respectively [Ki05].

2.4.3 Internal conversion

Internal conversion is the processes in which the electromagnetic multipole field of the nucleus interacts with the atomic electrons, resulting in an electron emission [Kr88]. It was first discovered and named as "conversion of the γ-radiation" by

Meitner and Hahn [Ha24, Me24]. A few years later Hulme gave the first correct theoretical interpretation of the effect [Hu32], and together with Taylor and Mott set the foundation for the development of a relativistic theory on internal conversion [Hu36, Ta32, Ta33].

The emitted electron is one of the atomic electrons and unlike β decay it is not created during the decay process. This implies that internal conversion is a threshold process with the threshold depending on the binding energy, B_i, of the atomic shell involved. The kinetic energy of the conversion electron is the energy of the transition (equal to the energy of the corresponding γ ray if the nuclear recoil is not considered) minus the binding energy of the electron [Kr88, Ej89].

$$T_e = \Delta E - B_i, \tag{2.32}$$

B_i depends on the electronic shell from which the electron comes and so conversion electrons are labelled according to the shell they originate from, K, L, M and so on. This means that a conversion electron spectrum shows discrete peaks belonging to different shells for each transition (unlike the continuum from β decays). With sufficient resolving power, peaks from the different subshells can be discerned. An example of a high resolution spectrum taken from [Gr60] is shown in Figure 2.9.

The vacancy left in the atomic shell after a conversion electron is emitted is filled rapidly by electrons from higher orbitals. This leads to the emission of X-rays (characteristic K X-rays when a K electron is emitted and so on) that can be used to identify internal conversion when studying a γ-ray spectrum.

Internal conversion and γ-ray emission are competing modes of decay. To show which one is preferred in each case, the internal conversion coefficient (ICC) is defined as the ratio of the electron emission rate to the γ-emission rate,

$$\alpha = \frac{\lambda_e}{\lambda_\gamma}. \tag{2.33}$$

α is the total ICC giving the probability of electron emission relative to γ-ray emission. Since different electronic shells correspond to different binding energies a partial ICC

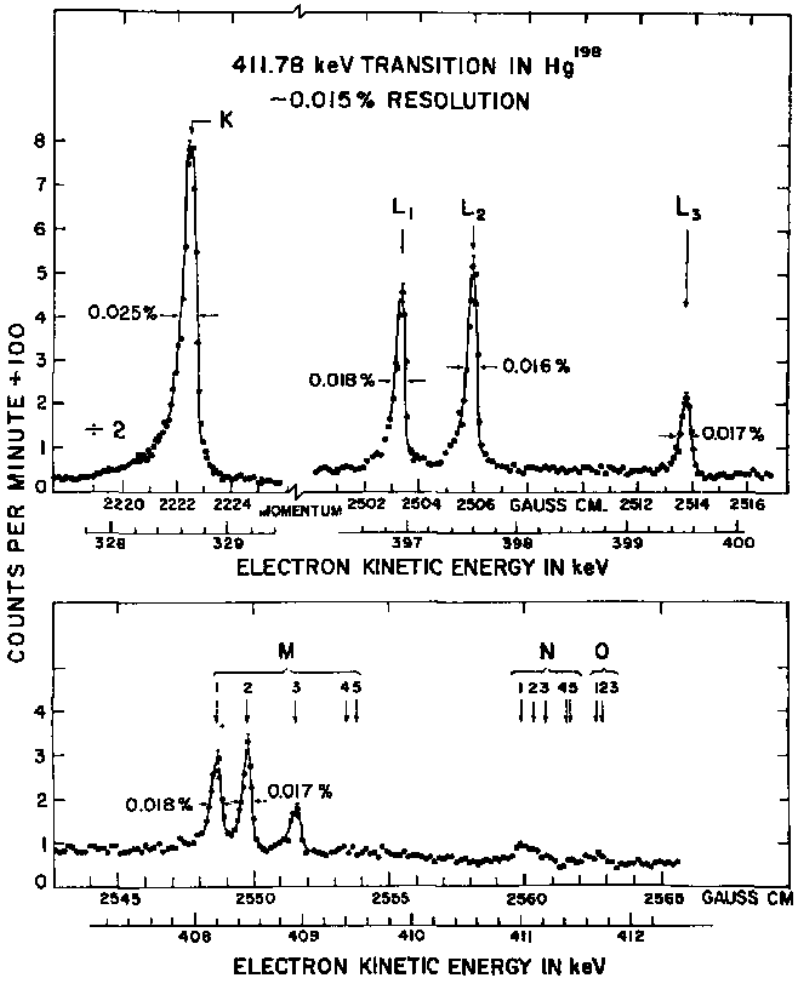

Figure 2.9: A high resolution ICE spectrum showing the conversion lines from the 411.77 keV transition in ^{198}Hg taken from [Gr60]. The spectra were taken using the Chalk River $\pi\sqrt{2}$ spectrometer [Gr60] at a resolution setting of ~0.015%.

can be defined for each shell as:

$$\alpha_i = \frac{\lambda_{e_i}}{\lambda_\gamma}, \tag{2.34}$$

with i representing the shell/subshell. The total electromagnetic decay rate can be written either using the total ICC or partial ICCs as:

$$\lambda_t = \lambda_\gamma(1+\alpha) = \lambda_\gamma(1+\alpha_K+\alpha_{L_I}+\alpha_{L_{II}}+\alpha_{L_{III}}+...). \tag{2.35}$$

The study of ICCs has many useful applications both in nuclear structure and

in other fields. By comparing experimental and calculated values it is possible to determine multipolarities and mixing ratios of transitions, which can lead to spin and parity assignments of excited nuclear states. Knowledge of accurate ICCs is needed in determining total transition rates, and are also used in nuclear reaction calculations, nuclear medicine, environmental control and the nuclear fuel cycle [Ba02, Ki08, Ge08].

A simple nonrelativistic way to define the ICCs in the case of a point nucleus for energies above thresholds gives:

$$\alpha(EL) \cong \frac{Z^3}{n^3}\left(\frac{L}{L+1}\right)\left(\frac{e^2}{4\pi\epsilon_0\hbar c}\right)^4\left(\frac{2m_ec^2}{E}\right)^{L+5/2}, \tag{2.36}$$

for the electric multipoles and

$$\alpha(ML) \cong \frac{Z^3}{n^3}\left(\frac{e^2}{4\pi\epsilon_0\hbar c}\right)^4\left(\frac{2m_ec^2}{E}\right)^{L+3/2}, \tag{2.37}$$

for magnetic multipoles [Kr88].

More realistic definitions of the ICC can be found in Rösel et al. [Ro78] using the relativistic Hartree-Fock-Slater method and in Band et al. [Ba02] using Dirac-Fock calculations.

From Equations 2.36 and 2.37 some general characteristics of the ICCs can be seen [Ro66]:

- They increase rapidly with increasing nuclear charge (atomic number Z).
- They increase with multipole order (L).
- They decrease with increasing transition energy (E).
- They decrease for higher atomic shells (n).

These general features are present in all ICC calculations. ICCs deviate from this pattern at threshold energies where the ejected electron has zero kinetic energy [Ro78].

The dependencies of the internal conversion coefficients on physical parameters are shown in Figure 2.10, where the ICCs for different elements, transition multipolarities and transition energies are compared. Figure 2.11 concentrates on just one superheavy

element, but similar behaviour is present in all the heavy nuclei. The high ICCs for these elements, especially at low transition energies, emphasise the importance of studying internal conversion in this region of the chart of nuclei.

The dependence of the energy of conversion electrons on the binding energy is clearly seen in Figures 2.10 and 2.11. The sudden increase on the ICCs seen in these figures takes place when the transition energy becomes equal to the binding energy of the next available atomic electron shell. These thresholds are obvious for fermium at the lower multipolarity transitions. As the multipolarity increases the ICCs of higher shells dominate over the ones from lower shells and a threshold is not visible in the plot. For example for an 145 keV E1 transition in fermium the α_K is one order of magnitude greater than α_L and α_M, whereas for an E5 transition of the same energy α_K is seven orders of magnitude smaller than both of them.

When the nucleus is considered as having finite size there is a non-zero probability for electrons penetrating into the nucleus. The ICCs calculated using Equations 2.36 and 2.37 and in [Ro78] do not take into account the nucleus-electron interaction while the electron is inside the nucleus. The surface current model [Sl51] used in the calculations in [Ba02] incorporates this interaction approximately.

For highly hindered transitions this effect is significant and corrections are needed in the calculations. For unhindered transitions it is still quite important for M1 transitions and less for M2, M3 and higher multipolarities [Ba02]. To estimate the magnitude of this effect, calculations that use no-penetration models are compared with ones that use surface current models. The effect for an 100 keV M1 transition varies from ∼0.01% for light elements to ∼16% for superheavy elements [Ba02, Ki08].

The most widely used ICC tables are those of Hager and Seltzer [Ha68], Rösel et al. [Ro78] and Band and Trzhaskovskaya [Ba78]. All these calculations use the relativistic Hartree-Fock-Slater method. More recently Band et al. [Ba02] published tables that show great improvements in accuracy using the Dirac-Fock method. The most precise calculations so far are made with the BrIcc conversion coefficient calculator [Ki08] using Dirac-Fock. This is shown in [Ge08] where a comparison of the above-mentioned

calculations with measured values is made.

Here a hypothetical example of multipole order and multipole mixing ratio assignment is shown. Let us consider that in an internal conversion experiment studying fermium a 200 keV transition was measured. From the absolute values of ICCs and their ratios α_i/α_j (see Figure 2.12 top diagram) for this transition one can assign its multipolarity [Ej89]. This can also be made using the normalised values of ICCs (normalised so that for every transition $\sum \alpha_i = 1$), shown in the bottom diagram of Figure 2.12, and comparing the theoretical and experimental patterns for the L_I, L_{II} and L_{III} shells. For mixed multipole transitions the multipole mixing ratio, δ^2, can also be assigned. This is possible because the conversion coefficients are sensitive to the multipolarities but are independent of the transition matrix elements.

It can be proved that the $M1$, $E2$ multiple mixing ratio can be calculated from the $\alpha_{L_I} \ : \ \alpha_{L_{II}}$ ratios using the relation:

$$\delta^2 = \frac{\alpha^c_{L_I}(M1) - \alpha^c_{L_{II}}(M1) \cdot \alpha^m_{L_{II}}/\alpha^m_{L_I}}{\alpha^c_{L_{II}}(E2) \cdot \alpha^m_{L_{II}}/\alpha^m_{L_I} - \alpha^c_{L_I}(E2)}, \tag{2.38}$$

where the ICCs marked with superscript m refer to measured values and those marked with superscript c refer to calculated values.

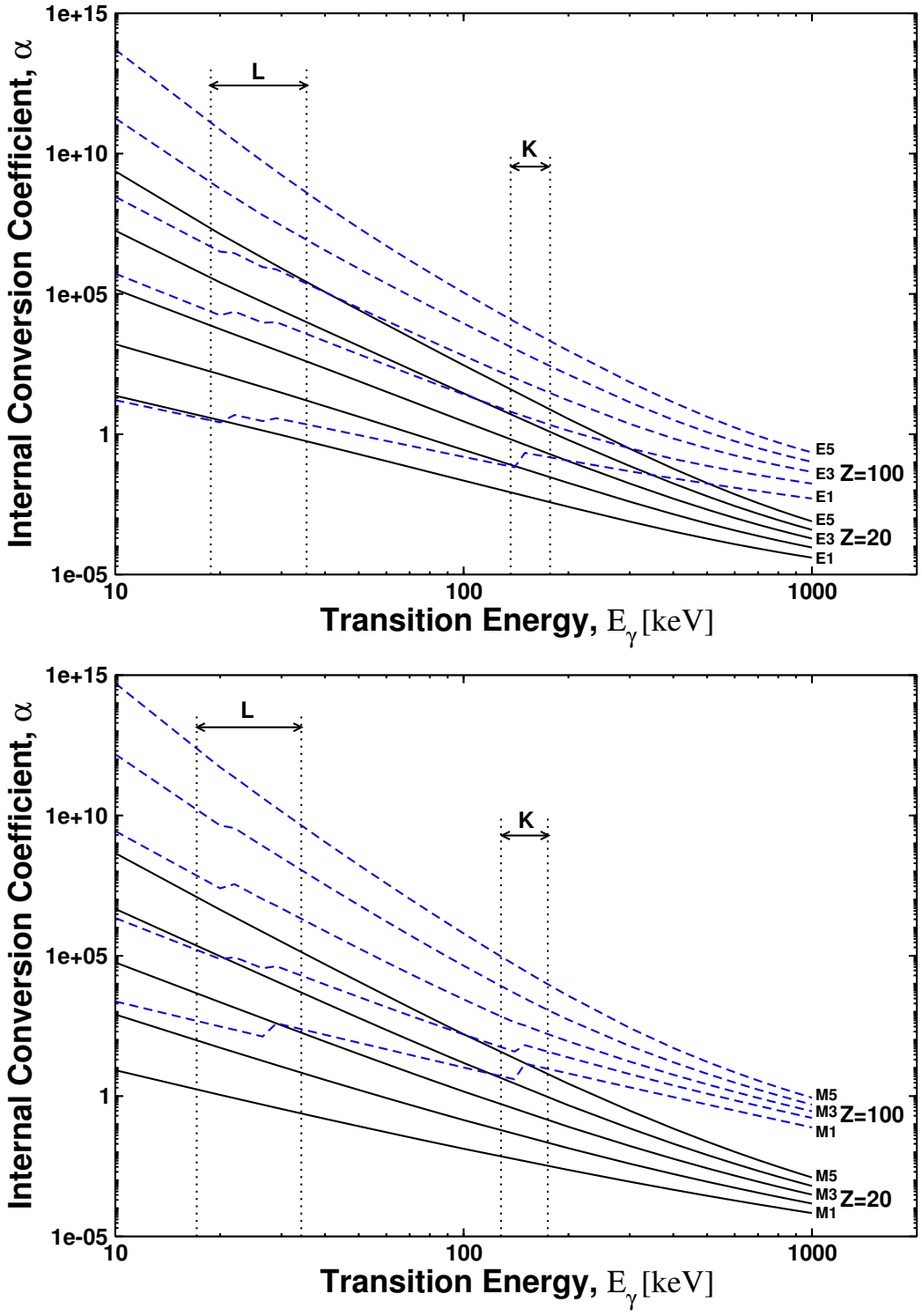

Figure 2.10: Internal conversion coefficients for electric (top) and magnetic (bottom) transitions with multipolarity L⩽5 as a function of transition energy for elements with Z=20 and Z=100 [Ki08]. The positions of the bound electron shells are indicated.

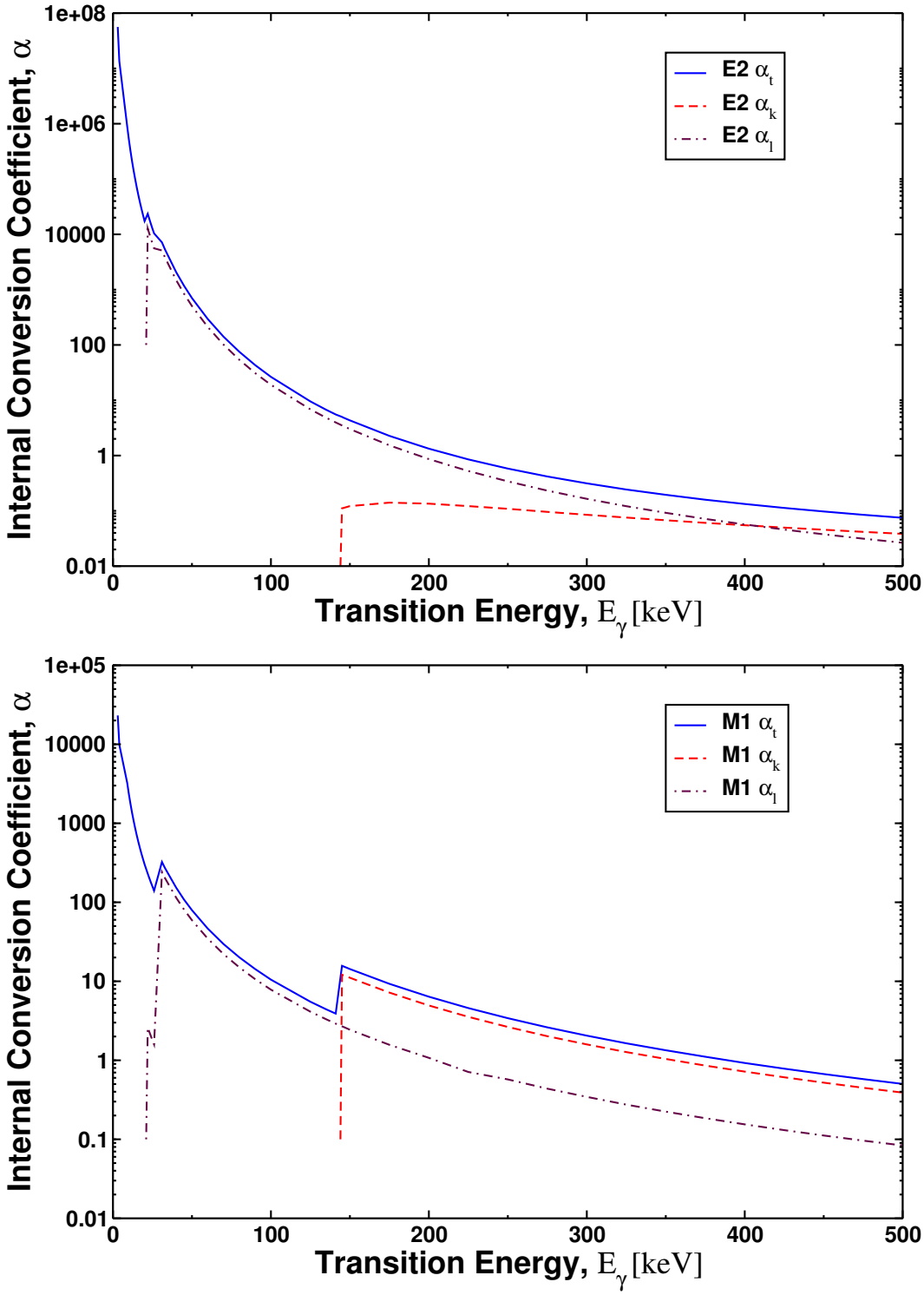

Figure 2.11: Internal conversion coefficients for E2 transitions (top) and M1 transitions (bottom) in fermium (Z=100) with respect to transition energy.

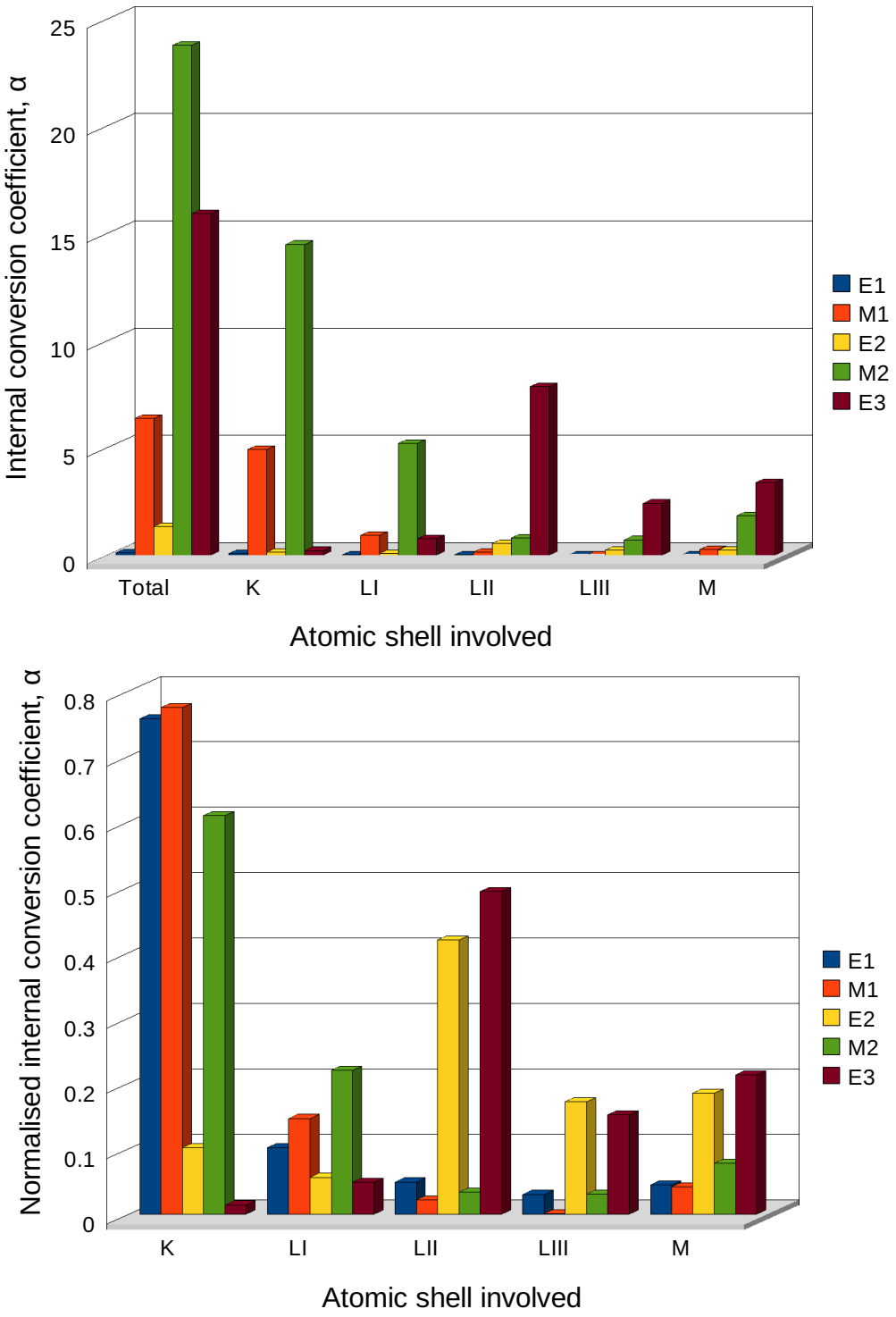

Figure 2.12: Absolute (top) and normalised, so that for every transition $\sum \alpha_i = 1$, (bottom) internal conversion coefficients for different multiples for a 200 keV transition in fermium.

Chapter 3

Concept of an ICE and γ-ray spectrometer

3.1 Historical review of γ-ray and electron spectrometers

The first great leap in the detection efficiency and resolution of charge particle and γ-ray detectors was made with the introduction of solid state detectors. For γ rays, organic (plastic) and inorganic scintillators (NaI(Tl), BaF_2, BGO etc.) and semiconductor detectors (Ge(Li) and HPGe) were used [Ne66, Kn00]. For charged particles, semiconductors like silicon were found to be ideal in most cases [Gi66, Kn00].

A major advancement in the detection of γ rays was the construction of large γ-ray detector arrays surrounding the target region [No94]. The first generation of such arrays consisted of crystal scintillators coupled to photomultiplier tubes (PMTs), for example NaI arrays such as the crystal balls at Argonne [Ja83] and Heidelberg [Si80] and BaF_2 arrays such as the Chateau de Cristal in Strasbourg [Be84].

The use of HPGe detectors with anti-Compton suppression shields (initially with NaI and later on using BGO crystals [No94]) led to the second generation arrays such as TESSA [Tw84] and Hera [Di84] followed by the third generation arrays like

GAMMASPHERE [Le90] and EUROBALL [Eb92]. Fourth generation arrays that use γ-ray tracking (AGATA [Si05] and GRETA [Le03]) are under development.

The story in electron spectroscopy has been somewhat different. The necessity of discriminating electrons from other charged particles and reducing the low energy electron background has led to the use of magnetic and electric fields in combination with a detector arrangement.

The first semicircular spectrometers [Da12, Da13] were built almost a century ago, but they lacked space-focusing. Later on, long and short lens spectrometers helped to solve this problem [Ml79]. Better focusing and dispersion was achieved with the double focusing $\pi\sqrt{2}$ spectrometer [Si46] and the orange spectrometer [Vl56, Ko65].

Electron spectrometers can be separated into mainly two categories: devices that use longitudinal magnetic fields to transport the electrons to the detector and devices that use fields transverse to the electron trajectories [Si66].

Examples of spectrometers from both categories can be found in [Ej89] and [Ml79]. A good example of the first type is SACRED [Bu96, Ka04] operated in Jyväskylä. Orange spectrometers and the more compact mini-oranges [Kl72] are the best examples of the second type. Successful use of mini-orange arrays has also been reported [Ga01]. Spectrometers based on different magnet arrangements than in the orange spectrometer also fall in this category [Ki97].

The mini-orange spectrometer uses permanent magnets to guide electrons to a silicon detector positioned behind a central absorber. The magnets act as a filter to separate electrons from positrons and the absorber reduces the amount of γ-rays and other background radiation from reaching the detector. This spectrometer however only transmits electrons in a narrow energy window and in a small solid angle. This problem can be overcome by the use of smaller magnets relative to the detector size. A simple representation of a mini-orange filter is shown in Figure 3.1.

Combined γ-ray and electron spectrometers are very powerful tools in spectroscopy. Magnetic spectrometers have been combined with a small number of γ-ray detectors in the past giving many interesting results. Drastically improved results can be achieved

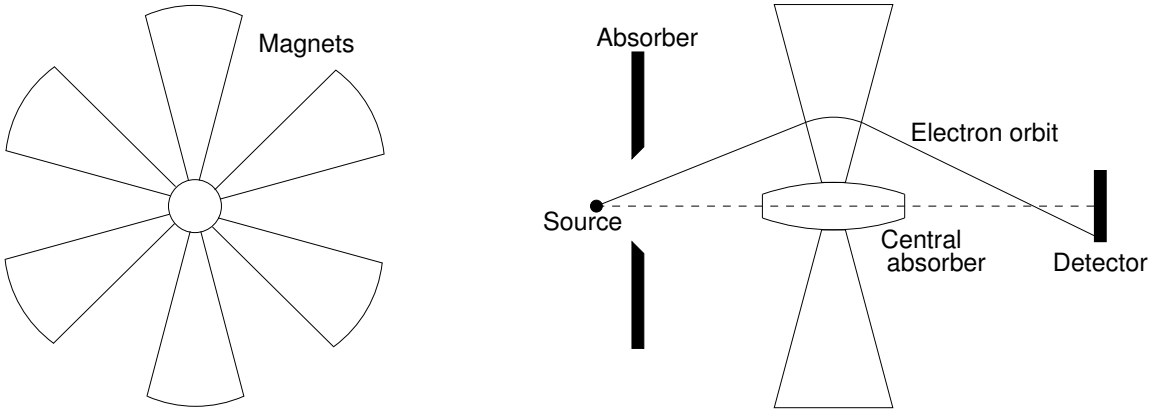

Figure 3.1: A simple diagram of a mini-orange spectrometer. On the left a view of the spectrometer from the target position and on the right a view showing the source and detector and a random electron orbit.

by combining electron spectrometers with γ-ray detector arrays.

An example of this is ICEBall [Me93], a mini-orange array that can be used in conjunction with large γ-ray detector arrays like the Spin Spectrometer and GAMMASPHERE. It consists of six mini-orange spectrometers and the same number of Si(Li) detectors. Its compact geometry allows it to be positioned inside the target chamber of the γ-ray detector arrays.

Magnetic lenses with silicon detectors were combined in many cases with germanium detectors and scintillators in different geometries as described in [Di95, Di99].

A different approach was taken by a Polish collaboration [An08] combining quasi-mini-oranges (similar to mini-oranges only without the central absorber and using less magnets) with a solenoid field transporting the electrons to five detectors (2 Si(Li) and 3 PIPS-passivated implanted planar silicon detectors). This spectrometer can be coupled to the OSIRIS-II HPGe detector array.

SAGE falls in the category of magnetic lenses combined with germanium detectors. It is built on experience from previous devices trying to optimise its resolving power and efficiency both for electrons and γ rays. Along with a relatively high electron transmission efficiency it is a prominent representative in the field of combined

electron and γ-ray spectroscopy.

3.2 SAGE design requirements

SAGE is a spectrometer that combines γ-ray and internal conversion electron spectroscopy. This is not an easy task as many different parameters and issues need to be optimised in order for such a spectrometer to be successful.

- γ-ray detection:
  To efficiently detect γ rays with energies less than 1 MeV it is essential to have as little absorbing material as possible in the path of the γ rays to the detector.

- Electron detection:
  A silicon detector is used for the detection of ICEs but due to its high sensitivity to all types of radiation it needs to be positioned far from the target.

- Electron transport:
  To transport the ICEs to the detector a magnetic field is required and so solenoid coils need to be implemented in the design.

- Reduction of electron background:
  Low energy delta electrons are produced when the beam particles interact with the target and the surrounding materials. Reaction kinematics cause most delta electrons to move at forward angles [Sc92, Ke92]. Placing the detector at a backward angle and using a high-voltage barrier between the target and the detector reduces the amount of delta electrons reaching the silicon detector.

- Reduction of Doppler broadening:
  Doppler broadening has a large effect in ICE spectroscopy. Using an almost collinear geometry between the magnetic field axis and the beam axis reduces this.

- Analysis techniques:

  To use the powerful analysis technique of recoil-decay tagging, SAGE needs to be combined with a recoil separator and a focal-plane spectrometer.

- High beam intensities:

  For the study of exotic nuclei with very low production cross-sections higher beam intensities are required. Digital electronics allow the data acquisition system to cope with the higher count rates. Rotating targets are also essential in this case.

Many compromises were made during the design as a result of the above restrictions not being independent of each other. For example an optimal magnetic field that would achieve maximum ICE transmission efficiency would require the target to lie within the solenoid coils. This would result in all the γ rays being absorbed by the coil material, rendering the γ-ray detectors useless.

Each one of the above topics is approached and discussed in detail in the following sections.

3.3 Geometry of the setup

To make the description of the setup easier a rendered mechanical drawing of SAGE is shown in Figure 3.2, with its main parts being the germanium and silicon detectors. In the figure SAGE is combined with RITU and GREAT.

- Germanium-detector array

  The JUROGAM II germanium-detector array surrounds the target region and detects the prompt γ rays. JUROGAM II consists of 15 Phase I Compton-suppressed germanium detectors [Be92, No94] and 24 fourfold segmented Clover detectors [Sh99]. To allow the use of magnetic coils close to the target one ring of five Phase I detectors is removed, leaving a total of 10 detectors in place (see Fig-

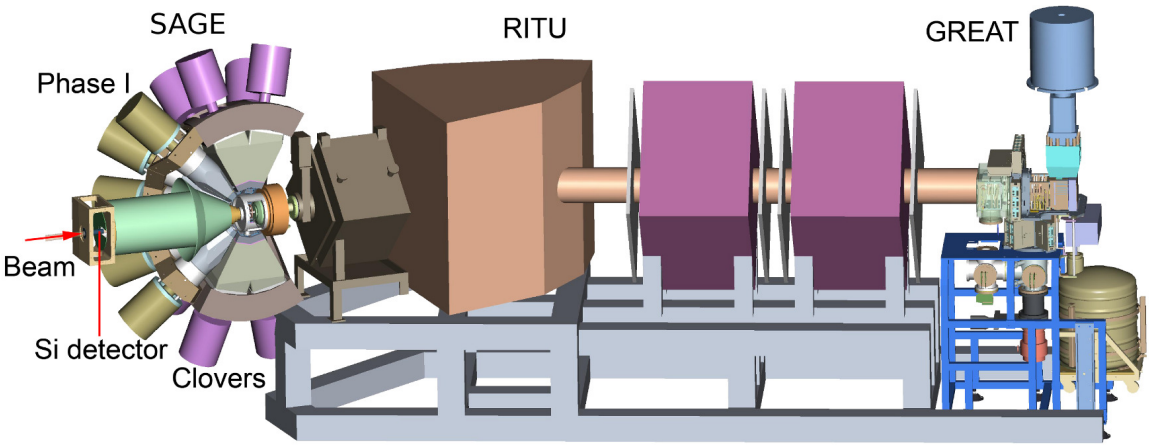

Figure 3.2: Schematic representation of the SAGE spectrometer, in conjunction with RITU and GREAT.

ure 3.3). The γ-ray detection efficiency of the array with 10 Phase I and 24 Clover detectors is 5.5% at 1332 keV.

- Silicon detector

  The internal conversion electrons are transmitted to the segmented silicon detector employing the magnetic field induced by solenoid coils. A near collinear geometry is used between the beam and solenoid axes to reduce Doppler broadening. The silicon detector is circular with 50 mm diameter and segmented into 90 individual segments. It is described in more detail in Section 4.1.

- Recoil separator and focal plane spectrometer

  SAGE is combined with the RITU gas-filled recoil separator [Le95] and the GREAT focal-plane spectrometer [Pa03b]. RITU transports the fusion evaporation reaction products towards GREAT where they are implanted in DSSDs. Their subsequent decays are detected by the different detectors of GREAT. Using SAGE in conjunction with RITU and GREAT allows the use of the recoil-decay tagging technique [Si86, Pa95].

  – RITU (Recoil Ion Transport Unit) is a QDQQ type separator using helium

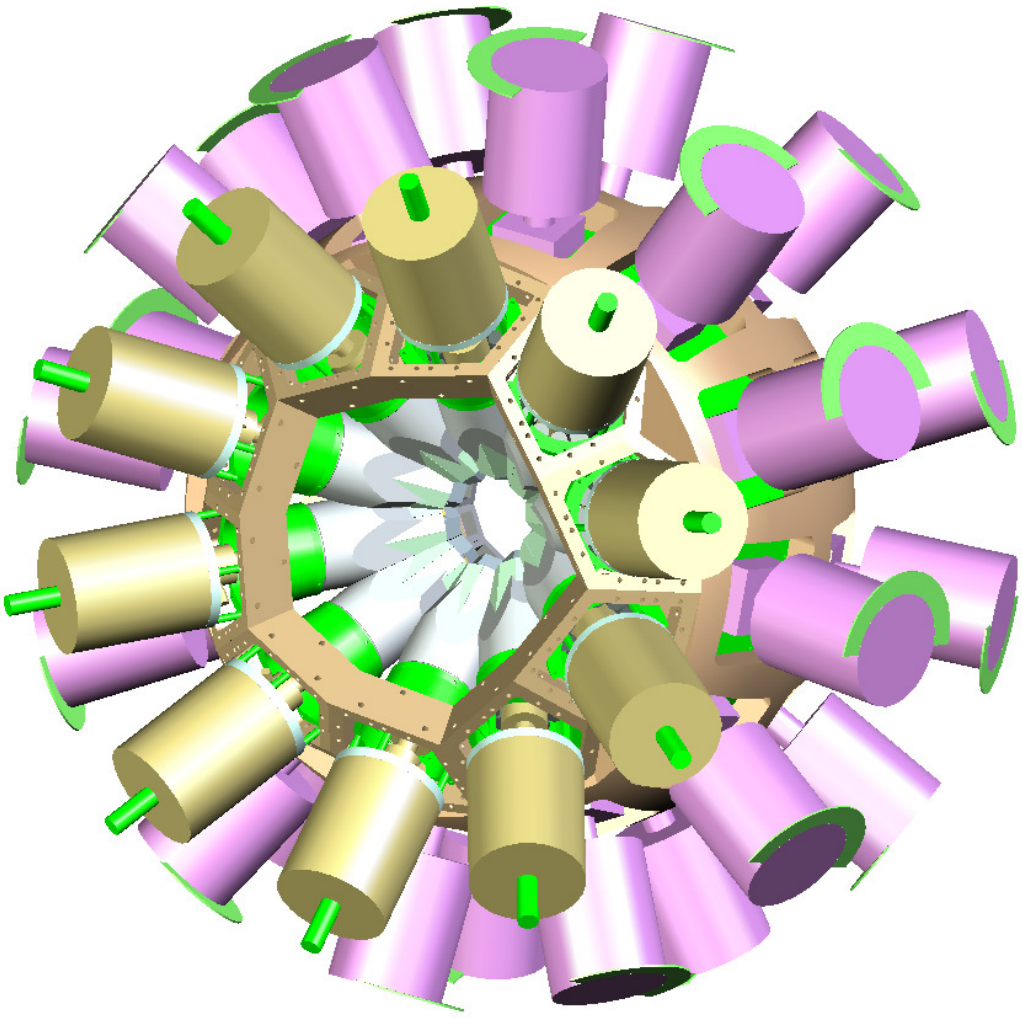

Figure 3.3: The JUROGAM II germanium-detector array. The purple dewars indicate the Clover detectors and the beige the Phase I detectors. The pentagon-shaped area in the front of the array is where the removed five Phase I detectors were positioned.

at 1 mbar pressure as a filling gas. It was mainly built and designed for the study of heavy elements. It has maximum magnetic rigidity of 2.2 Tm, angular acceptance of 10 msr and dispersion 10 mm/% [Le95].

– The GREAT (Gamma Recoil Electron Alpha Tagging) focal-plane spectrometer is an arrangement of silicon, germanium and gas detectors. At the entrance of GREAT lies a multiwire proportional counter (MWPC) which is

responsible, along with the DSSDs, for distinguishing fusion reaction products from their subsequent decays and from scattered beam particles. The recoils are implanted in the two DSSDs of GREAT. Different gain settings can be applied at the DSSDs to measure the electrons, protons or alpha particles the implanted ions emit. An array of PIN diodes (p-type - intrinsic - n-type semiconductor) surrounds the DSSDs with approximately 30% geometrical efficiency and detects ICE that are emitted from the decaying recoils. Low energy γ rays and X rays are measured by a planar double-sided germanium strip-detector situated directly behind the DSSDs. The GREAT Clover detector is positioned above the DSSDs and can detect higher energy γ rays with greater efficiency than the planar detector. For the same purpose additional detectors (usually VEGA or Clover detectors) may be placed at either side of the spectrometer and behind the DSSDs [Pa03b].

3.3.1 Mechanical design of SAGE

A series of solenoid magnetic coils are used to transport the conversion electrons to the silicon detector positioned upstream of the beam. This is necessary because the silicon detector is sensitive to all types of radiation, therefore it cannot be placed near the target region otherwise the useful conversion electron signals would be submerged in the background. A compromise between maximising the transmission efficiency, reducing background noise and keeping within the available space had to be made. Other aspects such as support, cooling and powering of the coils were taken into account when finalising the design.

The design process was an iterative procedure starting with a general design of the setup, simulating the magnetic and electric fields and using these to simulate the transmission efficiency. If the outcome was not satisfactory the design was modified by altering the dimensions and position of the solenoid coils, the high-voltage barrier, the carbon foil unit and the beam line. Figure 3.4 shows a cross-section of the setup

where the different parts can be seen.

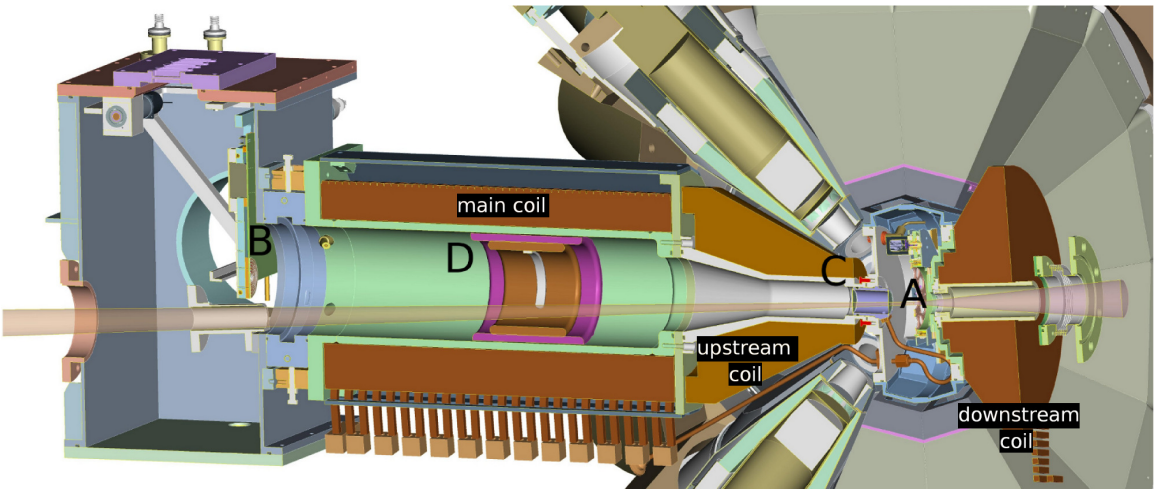

Figure 3.4: A cross-section of SAGE as seen from above. The different parts of the setup are as follows: "A" the target position, "B" the silicon detector, "C" the carbon foil unit and "D" the high-voltage barrier. Surrounding the target region are the JUROGAM II germanium detectors and around the beam pipe are the solenoid coils. The beam (represented by a cone) passes next to the detector moving towards the target.

The space envelope available for the coils is defined by JUROGAM II, RITU and the beam-line diagnostics box which contains vacuum pumps and a Faraday cup. The JUROGAM II array is positioned at the target region, so the volume defined by the collimators of the Compton-suppression shields of the germanium detectors provides the space limits for the target chamber. The shaping of both the downstream and upstream coil (shown in Figure 3.4) depends on the space envelope outlined by the two outer rings of JUROGAM II detectors. As the target position is fixed the position of the gate valve connecting SAGE to RITU (see Figure 3.5) gives the maximum allowed length of the downstream coil. Similarly, the position of the beam-line diagnostics box restricts the length of the main and upstream coils.

The arrangement is schematically shown in Figure 3.5. Between the downstream coil and the RITU gate valve a bellows is needed to allow alignment adjustments, hence

the empty space in this region. Part of the large space between the main coil and the diagnostics table is taken by the detector chamber, but most of it is left empty. This is necessary in order for the setup to be positioned in and out of JUROGAM II.

In an ideal situation with no space restrictions, the magnetic field produced by the coils would be constant on the solenoid axis; in reality it is not so uniform and it shows valleys and peaks. In Figure 3.6 a comparison of the two is made. In both cases the detector is positioned in a region of lower magnetic flux density.

Ideally, the way to increase the transmission efficiency would be by applying a higher magnetic field between the target and RITU. This would act as a magnetic mirror reflecting some of the electrons moving towards RITU back to the detector. One such example is shown in Figure 3.6, where the single-coil geometry was modified to allow more current through some of the loops closest to RITU, thus boosting the field.

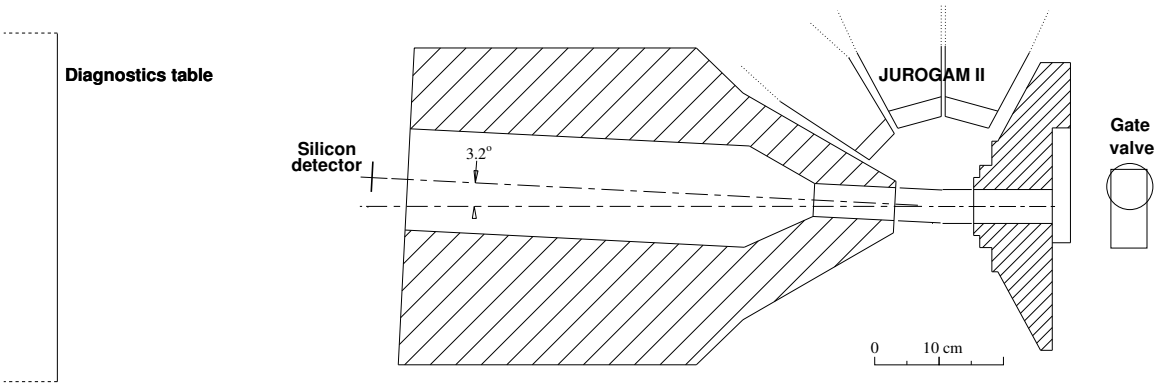

Figure 3.5: A schematic representation of the volume available for the solenoid coils. The gate valve connecting to RITU is on the right hand side and the beam diagnostics box on the left.

From the different types of magnetic coils commercially available, water-cooled copper coils were chosen for SAGE. In the first implementation of the SACRED spectrometer [Bu96] superconducting coils were employed, but were found to be difficult to work with and also require a lot more space than what was actually available. Permanent magnets were not an option either as they cannot provide the necessary

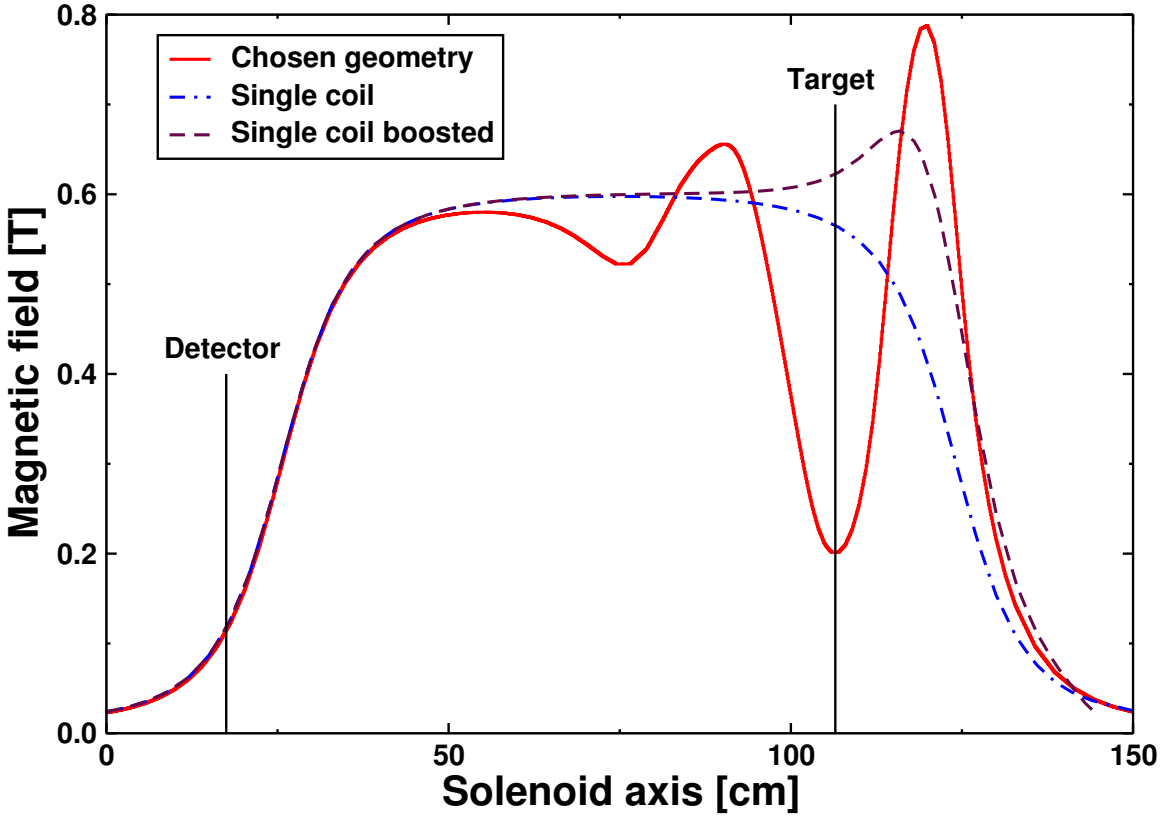

Figure 3.6: A comparison of the magnetic fields on the solenoid axis produced by a single coil, when no space restrictions apply, and by the more realistic space-restricted case. The field produced by a modified version of the single coil that boosts the field between the target and RITU is shown for comparison.

field profile. A picture of the actual magnetic coils along with the target chamber, taken during the construction of SAGE is shown in Figure 3.7 . Further information on the coils and how their cooling is made can be seen in Appendix C.

A relatively strong (0.5 T or more) and uniform magnetic field on the solenoid axis is essential for obtaining a high electron transmission efficiency. Additionally if the magnetic field is not adequately strong the electrons will move in larger radii (see Equation A.20 in Appendix A) making the use of a bigger, and hence more expensive, silicon detector necessary. On the other hand if the field is too strong then the majority of the electrons will be concentrated in the central segments of

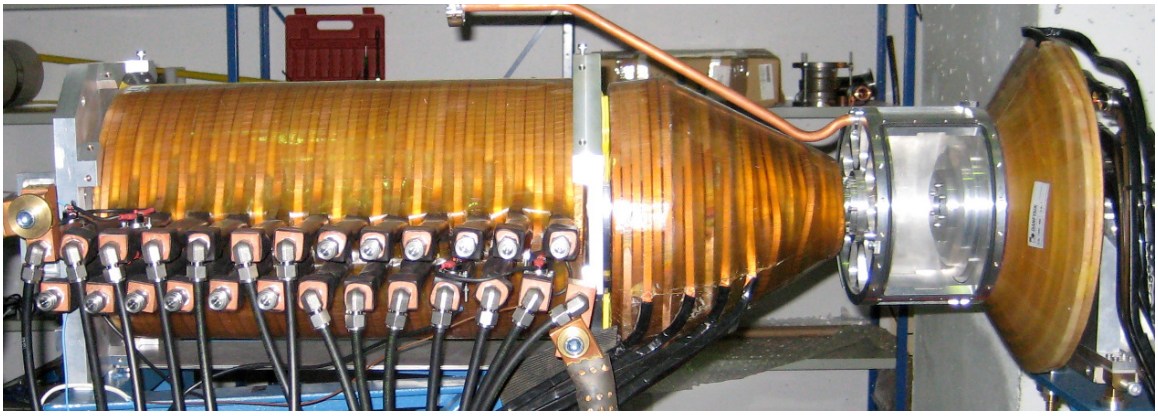

Figure 3.7: A picture of the magnetic coils and target chamber during construction.

the detector. To ensure that the electron flux is more equally distributed across the detector, this is positioned outside the bore of the magnet in a region of lower magnetic flux density. This is important in increasing the maximum allowed count rate for the detector and also to reduce the pileup.

In a lower magnetic field the spiral motion of the electrons on the solenoid axis is elongated, i.e. the electrons form fewer circles in the perpendicular plane per unit of length. This means that the incident angle between the normal to the detector surface and the electron path reduces, decreasing the probability for backscattering [Wa68, Ml79]. Backscattering is angle dependent but appears to be energy independent in the energy region between 40 keV and 1200 keV [Ka57, Wa68, Ca86, Me93].

Simulated and measured fields of the magnetic coils are discussed in detail in Section 3.4. The effect of the magnetic field on the PMTs of the BGO Compton-suppression shields of JUROGAM II is described in the same section. This effect is reduced by using steel shielding around the coils.

Previous experience with the SACRED spectrometer showed that collinear geometry between the solenoid axis and the beam axis provides the best spectral response [Bu96] (see [Bu87, Di91] for more details). A perfect collinear geometry would require the beam to pass through a hole at the centre of the detector, remarkably reducing the detection efficiency. In SAGE a 3.2° angle is adopted between the two axes. This

geometry will also decrease the high flux of background delta electrons, originating mainly from atomic collisions between beam and target particles [Ka04].

To further reduce the low energy background, a high-voltage barrier is positioned between the target and detector positions. This is discussed in more detail in Section 3.5.

The safe operation of a high-voltage barrier dictates its placement in a region of high vacuum, of the order of $10^{-6} - 10^{-7}$ mbar. A carbon foil unit is used to separate the high-voltage barrier region from the 1 mbar helium gas used in RITU (see Section 3.8).

Another effect of the collinear geometry is the Doppler shift of the electrons emitted from moving recoils. The unshifted electron energy, E, in the recoil rest frame can be derived using the Lorentz transformation for four-momentum and the invariance principle [Ka01]. These give,

$$E = \frac{E' + m_e - \beta \cos\theta' \sqrt{E'^2 + 2m_e E'}}{\sqrt{1-\beta^2}} - m_e, \tag{3.1}$$

where E' and θ' are the measured values in the laboratory frame and m_e is the rest mass of the electron. If different emission angles cannot be measured (as is the case here) then an average angle θ' may be used.

The method used for defining the average angle is the same as described in [Ka01]. By solving Equation 3.1 for θ', this angle can be calculated with respect to the shifted and unshifted transition energies. Unshifted are the Doppler corrected energies measured from the γ rays and shifted the ones measured from the conversion electrons. The Lorentz factor β is calculated from the reaction kinematics. For each transition observed in both the electron and γ-ray spectra and therefore for each energy, a different average emission angle is calculated. A straight line is fitted through these calculated angles to obtain an average Doppler correction angle for all the energies.

A quick calculation of the average angle can be made using the Monte Carlo code SOLENOID, presented in [Bu96] and Section 3.6. This code is executed for the desired reaction and amongst other values it gives the average emission angle per energy of the electrons that are subsequently detected.

Despite the energy dependence of the Doppler correction angle and the backscattering due to the mirroring effects described in Section 3.4, the above method yielded correct electron energies within 0.1 keV or less of the calculated ones, when used for SACRED. In SACRED average angles between 150-160° were used. Simulations performed for SAGE indicate similar values in the energy region between 40 and 400 keV.

3.3.2 Support and position adjustment mechanism

A support structure was designed and built (Figure 3.8) that allows individual fine position adjustment of every major part of SAGE as well as precise placement of the whole unit inside the JUROGAM II array.

The schematic diagram in Figure 3.9 shows the different parts of the support structure and the allowed movement for each one. All the parts of the setup form a rigid unit positioned on the main support frame (indicated with the number 1 in the schematic). This is supported on caster wheels used for rolling it into position and for crude positioning adjustment. When in the final position, brass pushers are used to lift the whole structure up to adjust it to the required height. A lifting cradle can also be attached to the main support frame for craning SAGE into the experimental hall if needed.

A secondary support frame (2 in the figure) resides on the main one, with the main and upstream coil supports fixed to it. This can move parallel to the main frame, but no height adjustment is possible at this level. The downstream support structure (number three in the diagram) slides into its final position on rails attached to the secondary frame. This is necessary because of the shape of the target chamber's back plate (drawn with dashed line in the schematic).

The main and upstream coils and detector chamber are fixed into position on the secondary frame and are used as the fixed points for adjusting the rest of the setup. The downstream coil can be adjusted precisely using a separate support plate (number 4) that allows movement on all three axes (Figure 3.10).

Alignment between the individual parts is ensured through spirit levels fixed on

the movable parts. A telescope is used to align the electron part of the setup with the beam line.

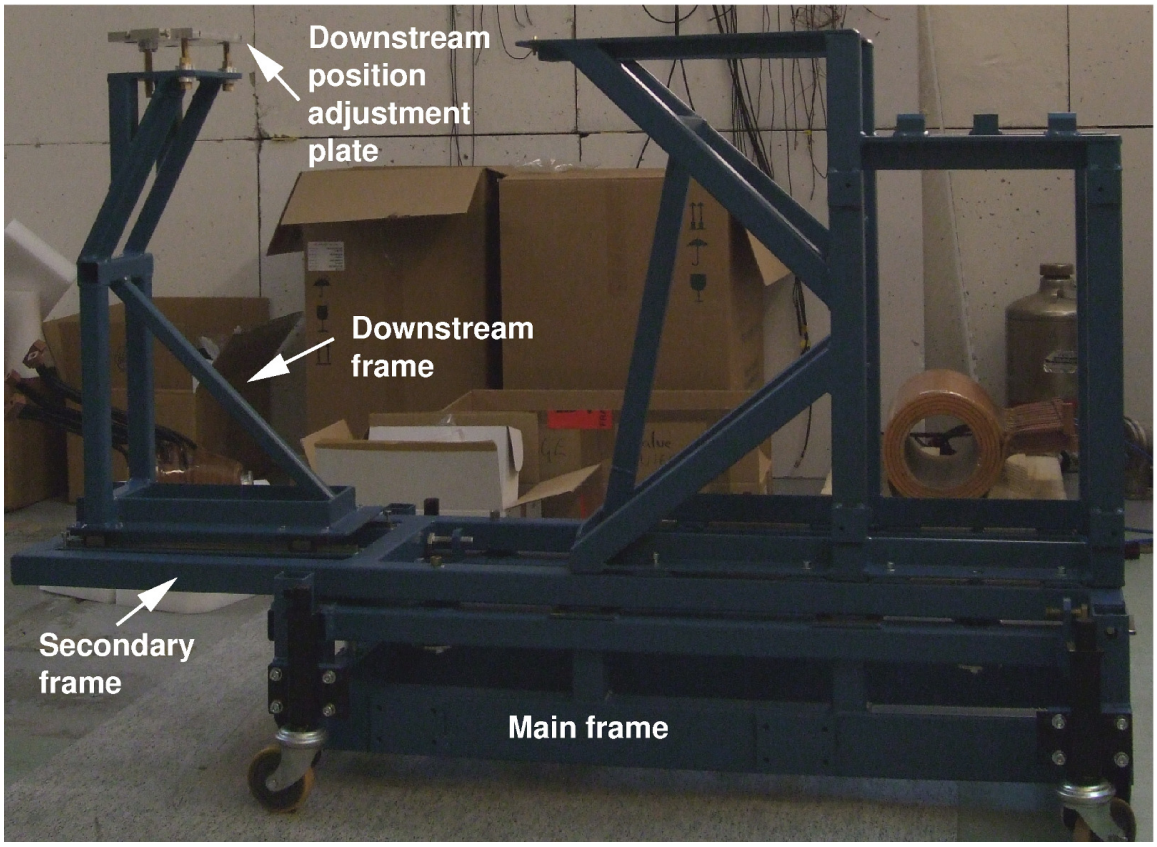

Figure 3.8: The support structure for the electron detector part of SAGE. The different adjustment planes are indicated on the figure, see Figure 3.9 for comparison.

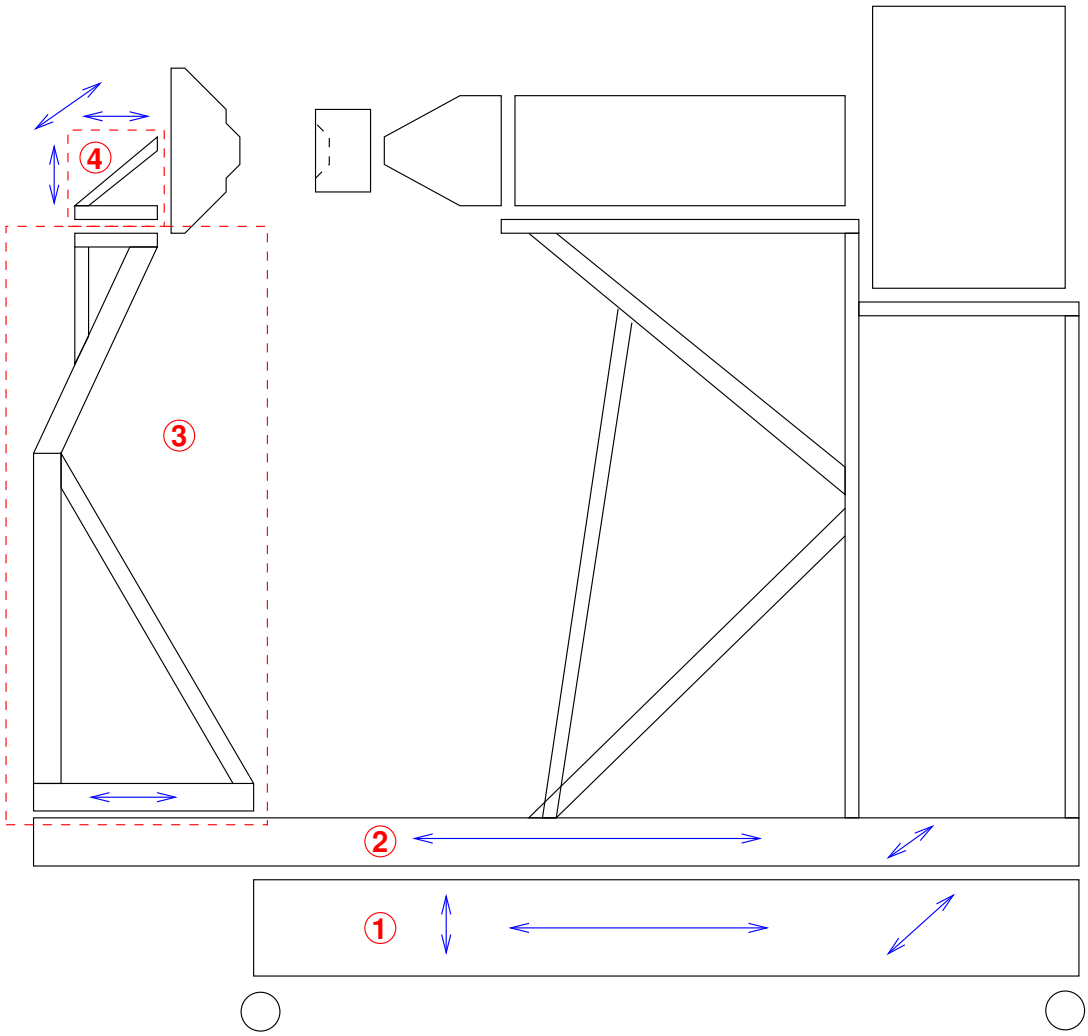

Figure 3.9: A schematic diagram of the support structure used to allow precise position alignment of SAGE. Different parts of the support structure are numbered as follows: (1) the main support frame, (2) the secondary frame, (3) the movable support for the downstream coil and (4) the position adjustment plate for the same coil. The arrows show the allowed directions of movement. The slanted arrows indicate movement perpendicularly to the drawing.

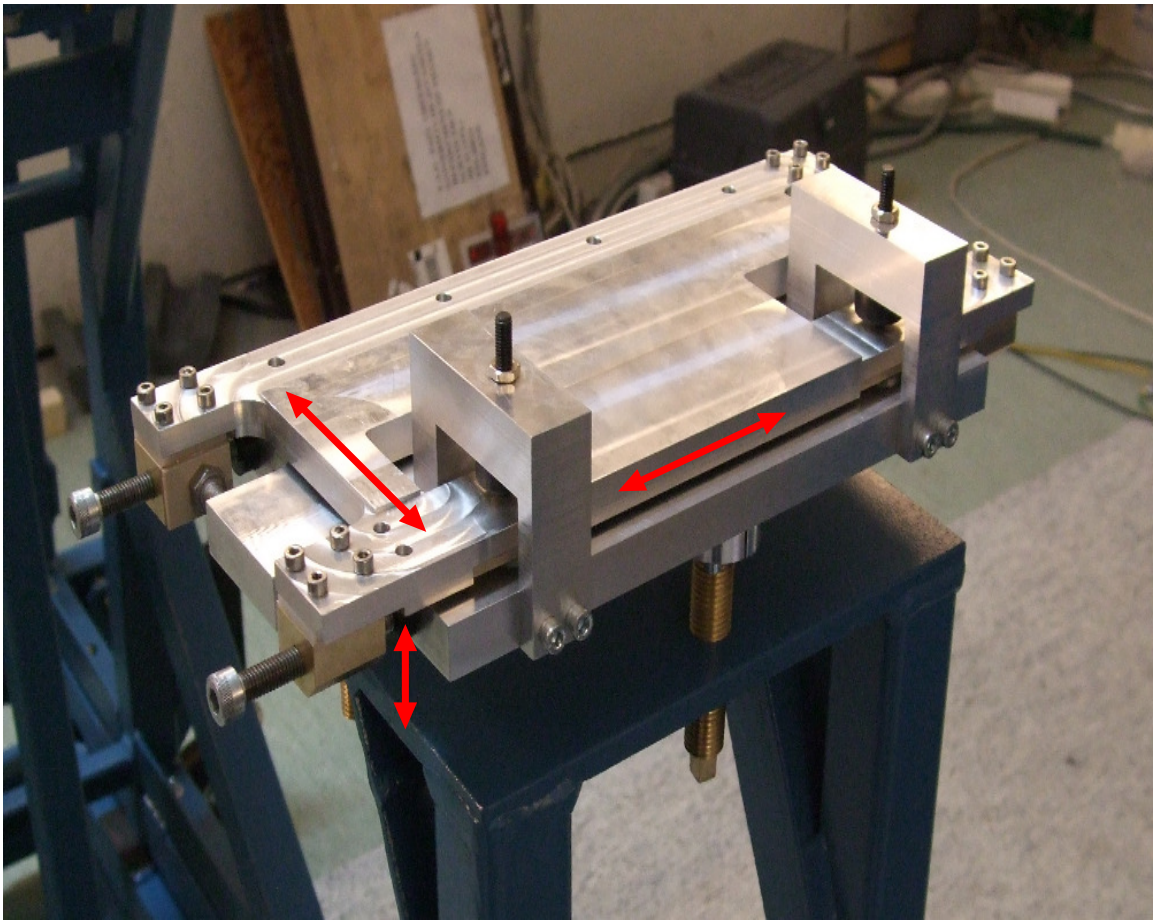

Figure 3.10: The downstream coil adjustment plate. The upper plate can move on ball bearings relative to the lower one allowing adjustment on the horizontal plane. Vertical adjustment is achieved by jacking screws.

3.4 Magnetic field study

3.4.1 Magnetic field simulations

A three-dimensional model of the solenoid coils and of the components made from magnetic material in their vicinity was built. The coil design was optimised through simulations and measurements using a prototype. Only results from simulations using the finalised solenoid coil geometry (Figure 3.11) will be presented here.

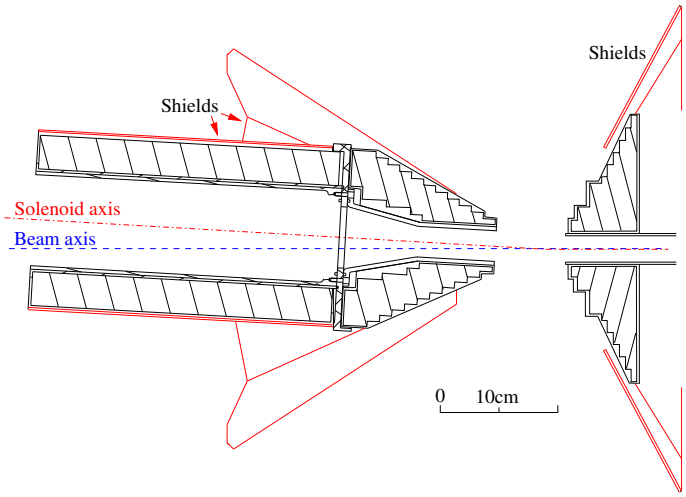

Figure 3.11: The finalised solenoid coil geometry. The magnetic shielding is also shown.

The maximum current that will be used in the coils of SAGE is 1000 A but for most experiments 700 A is adequate to allow high transmission efficiency. The magnetic field on the solenoid axis for 700 A and 1000 A current through the coils is presented in Figure 3.12. The magnetic field strength is reduced when lower current is used, but the peak to valley ratios (mirror ratios) do not change. Using the notation of Figure 3.12 the mirror ratios are presented in Table 3.1 along with the same ratios when magnetic shielding is used; as discussed further in the text.

Knowledge of the peak to valley ratios is important as the possibility an electron will be mirrored when approaching a stronger field (e.g. magnetic mirror effect when

Table 3.1: Comparison of the peak to valley ratios for the magnetic field on the solenoid axis with and without magnetic shielding.

Ratio	Without shielding	With shielding
a/b	1.11	1.11
c/b	1.26	1.23
c/d	3.26	3.92
e/d	3.91	4.52

moving from the target towards the detector) or even trapped between two stronger field regions (e.g. magnetic bottle effect between peaks c and e) depends greatly on these mirror ratios. It can be easily proved that for a certain mirror ratio particles need to have a large component of velocity parallel to the field axis to not be mirrored. Consequently particles with insufficient energy are mirrored/trapped.

$$\left|\frac{u_{\parallel 0}}{u_{\perp 0}}\right| < \left(\frac{B_m}{B} - 1\right)^{1/2}, \tag{3.2}$$

where $u_{\parallel 0}$ and $u_{\perp 0}$ are the components of velocity parallel and perpenticular to the field axis at the origin and B_m and B the maximum and minimum magnetic fields involved in the mirror ratio [Ja99].

The magnetic field flux lines when applying 1000 A current through the solenoid coils and without using magnetic shielding are shown in Figure 3.13. For higher flux densities the line spacing decreases, indicating that the field is mainly concentrated in the inner bore of the solenoids, weakening further away. The direction of the magnetic field is always tangential to the field lines. For reasons explained in Appendix B all the figures presenting magnetic lines use a totally collinear geometry between the beam and solenoid axes.

The magnetic field density equipotential lines as obtained from a simulation for 1000 A current are presented in Figure 3.14. Plots like Figure 3.12 are projections of

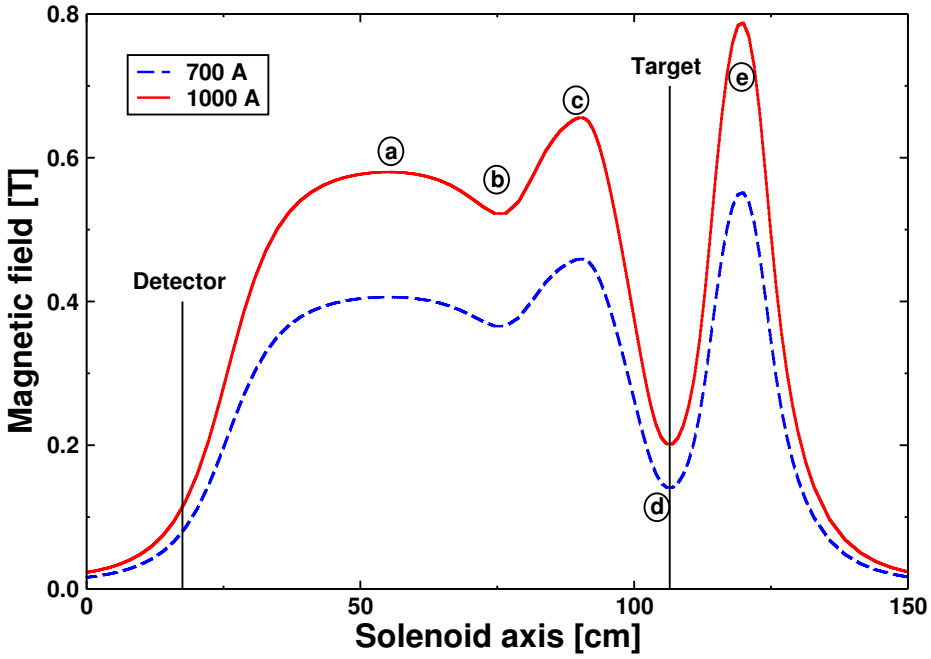

Figure 3.12: A comparison of the magnetic field strength on the solenoid axis for 700 and 1000 A current through the coils.

this plot on a certain axis. The lines are colour coded according to the strength of the field. The maximum field presented in this figure is restricted to 1 T, but a stronger field is present in the shields.

As was mentioned in Section 3.3, the strength of the magnetic field and the field direction close to the photomultiplier tubes highly affect the propagation of electrons between the dynodes of each PMT. Some of the PMTs of the BGO shields of JUROGAM II are individually shielded by thin mu-metal[1] cylinders. In order to weaken and redirect the magnetic field in the region of the PMTs 6 mm thick steel shielding plates are mounted as shown in Figure 3.11.

The direction of the magnetic field affects the force applied on the electrons inside the PMTs (Figure 3.15), as can be deduced from Equation A.10. The simulated effect of shielding on the direction of the magnetic field flux lines at 1000 A current

[1]Mu-metal is a nickel-iron alloy with very high magnetic permeability.

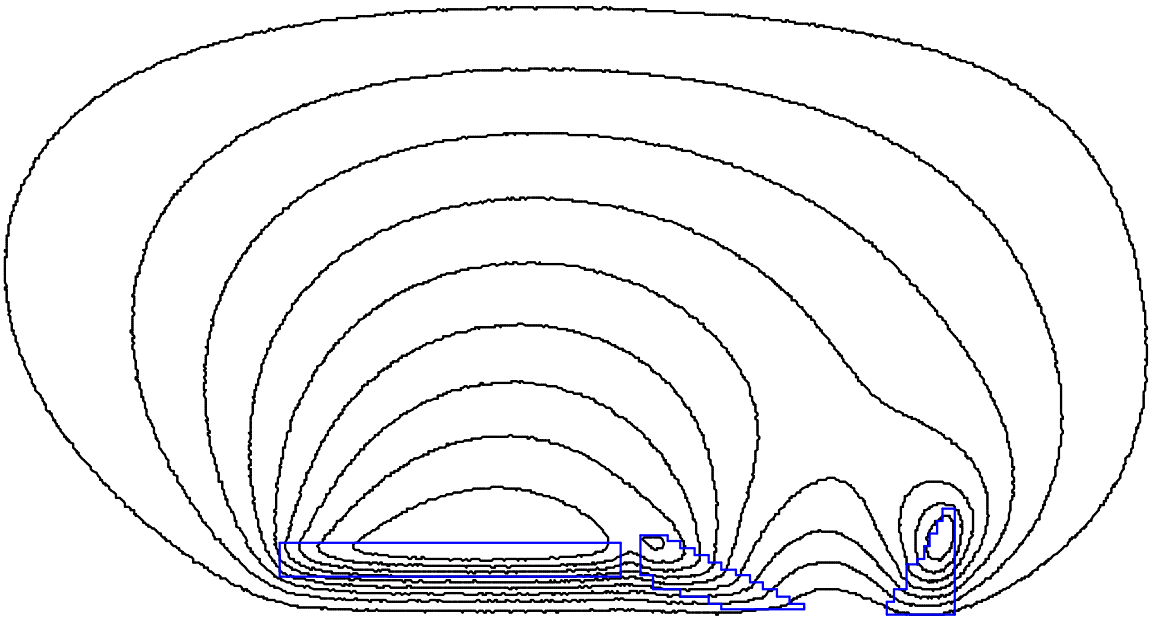

Figure 3.13: Magnetic field flux lines without magnetic shielding. The density of the lines is greater where the magnetic field is stronger. The current through the coils is 1000 A.

is presented in Figure 3.16.

The maximum field at the region of the PMTs that are situated closest to the coils is reduced by an order of magnitude due to the shields. As an example the field strength at point A of Figure 3.14 is reduced from 35.08 mT to 2.94 mT when shielding is used. From tests performed using a prototype and later with the SAGE coils it was found that thicker shielding is necessary close to these PMTs. This extra shielding was designed and mounted on the JUROGAM II array.

Another purpose of magnetic shielding is to increase the field strength on the solenoid axis as shown in Figure 3.17 for 1000 A current. The field upstream of the detector chamber where the shields lie closer to the solenoid axis is enhanced. The effect of the shields is smaller on the downstream side where the shielding plates are situated further from the axis. The peak to valley ratios are different to when no shielding is used as shown in Table 3.1. The increase of the e/d mirror ratio

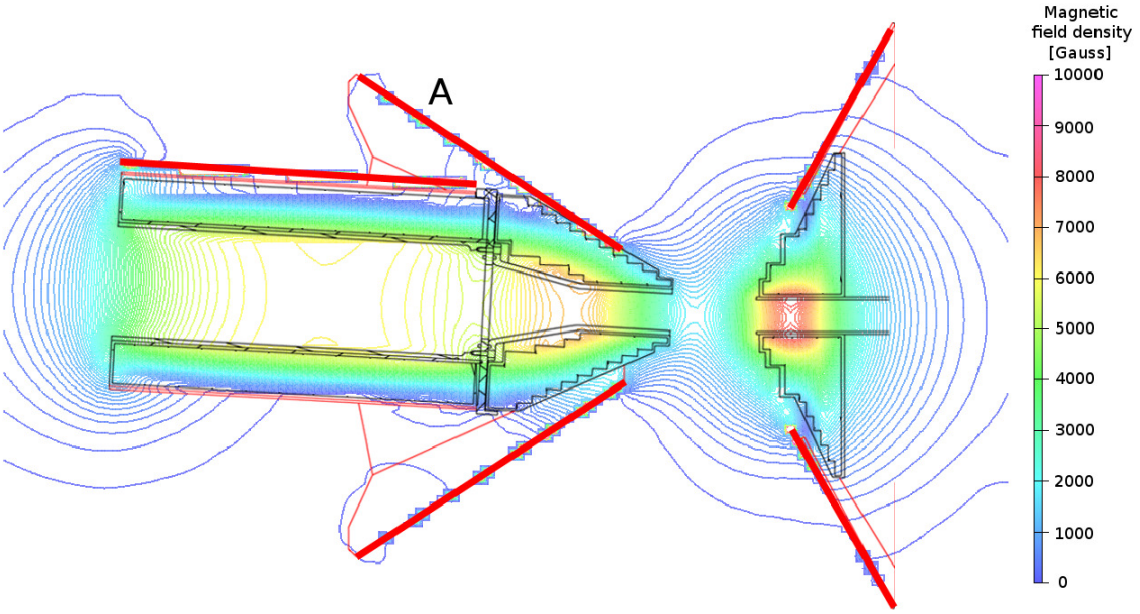

Figure 3.14: Equipotential lines of the magnetic field density for 1000 A current through the coils. The projection is made looking the setup from above so the bottom part of the main coil on the drawing is where the cooling outlets are positioned where no shielding is used. Point A indicates the position of the PMT closest to the solenoid coils.

leads to more electrons moving from the target towards RITU to be reflected towards the detector; even though the c/d ratio increases as well, the magnetic bottle effect reduces and both these factors increase the transmission efficiency.

The magnetic field on the solenoid axis was measured using a Hall-effect[2] gaussmeter and compared to the simulated one. All the magnetic coils were used in the measurement but only the main coil shielding was present. A tool to position the Hall probe precisely on the solenoid axis was designed and the Hall probe was corrected for the magnetic field of the earth.

The very good agreement between simulated and measured magnetic fields at

[2]The production of a transverse potential gradient in a material by a steady electric current which has a component normal to the magnetic field is called the Hall effect [Sm72]

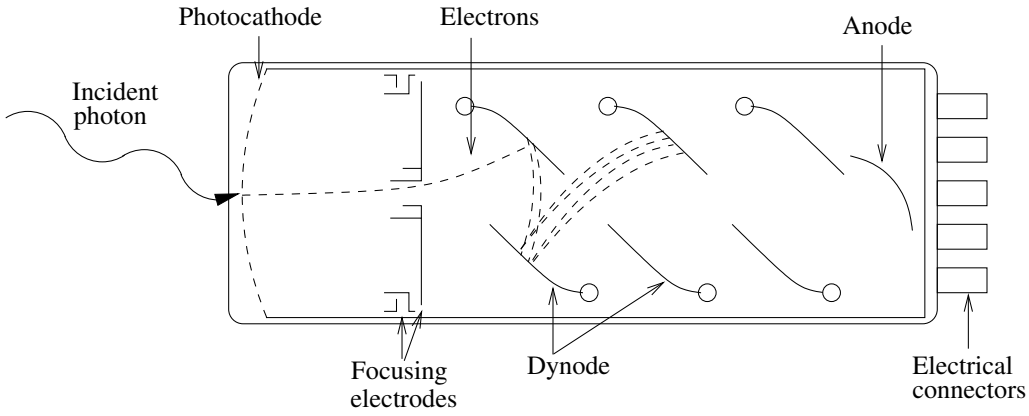

Figure 3.15: Schematic diagram of a photomultiplier tube showing the propagation of electrons between the dynodes.

700 A current is shown in Figure 3.18. The discrepancies are mainly due to uncertainties in the positioning of the Hall probe. The error of the Hall probe is of the order of 1%. All errors are smaller than the size of the data points.

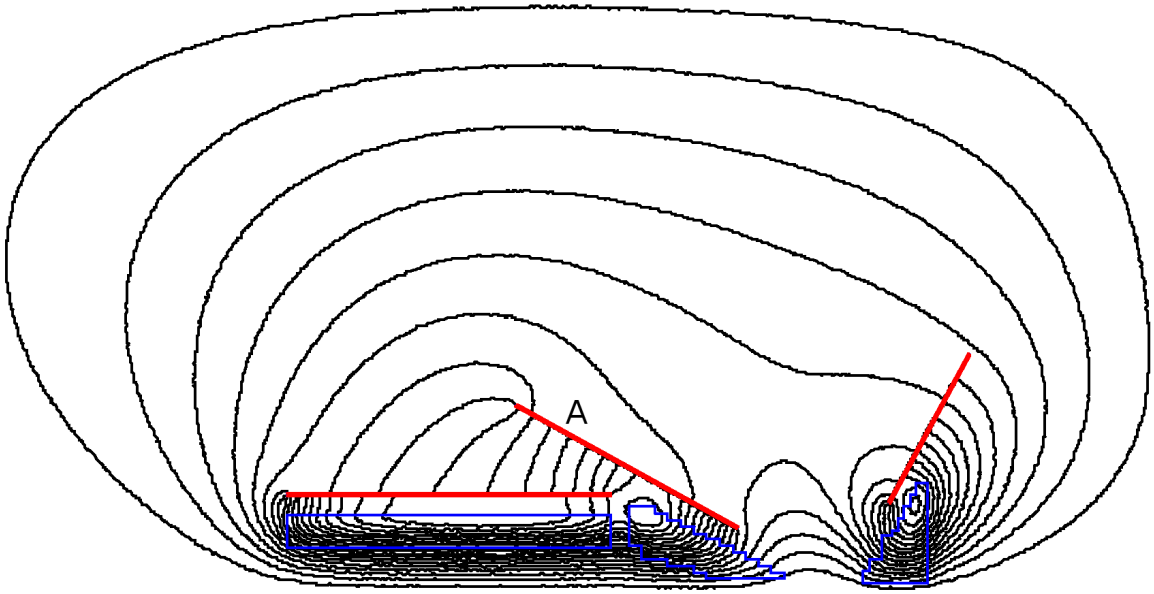

Figure 3.16: The magnetic field flux lines induced by the SAGE coils and employing the magnetic shielding plates. The current through the coils is 1000 A. Because the density of the lines is greater where the magnetic field is stronger, most of the magnetic field flux lines are directed through the shields. To show their direction outside the shield region a greater number of magnetic lines is used in this figure compared to Figure 3.13.

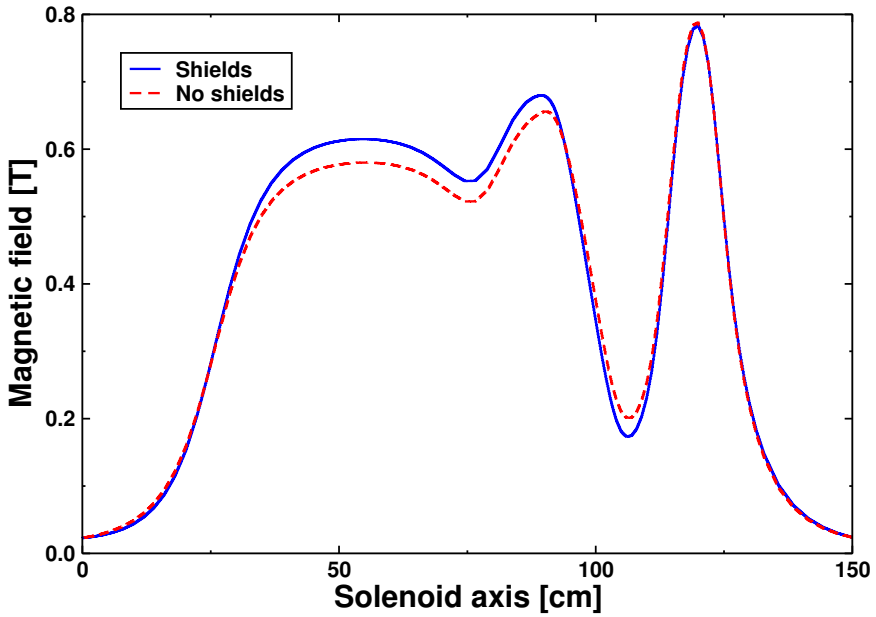

Figure 3.17: A comparison of the simulated magnetic field strength on the solenoid axis with and without shielding.

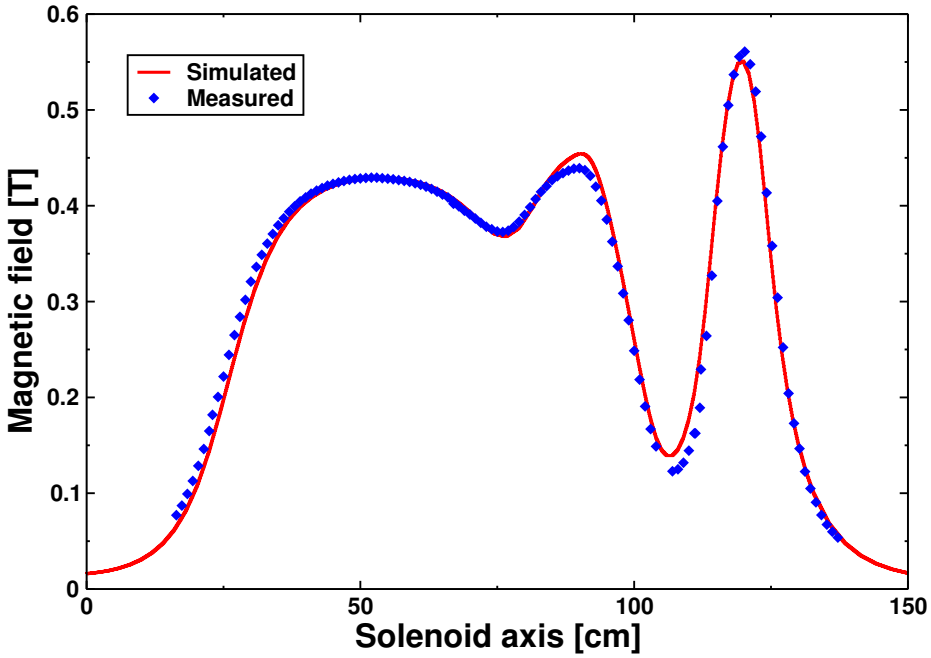

Figure 3.18: Measured and simulated magnetic fields on the solenoid axis.

3.4.2 Measurements using a prototype

Prototypes of SAGE were built to investigate the electron transmission efficiency and the magnetic shielding. These studies were made employing the SACRED solenoid coils.

The electron transmission efficiency measurements of the prototype are not directly comparable with SAGE as their geometries are not identical. In general, the SAGE coils are bigger and more uniform. One of the prototype setups is shown in Figure 3.19. In this setup an iron block was positioned inside the last coil (further right in Figure 3.19) to strengthen the magnetic field in the source region.

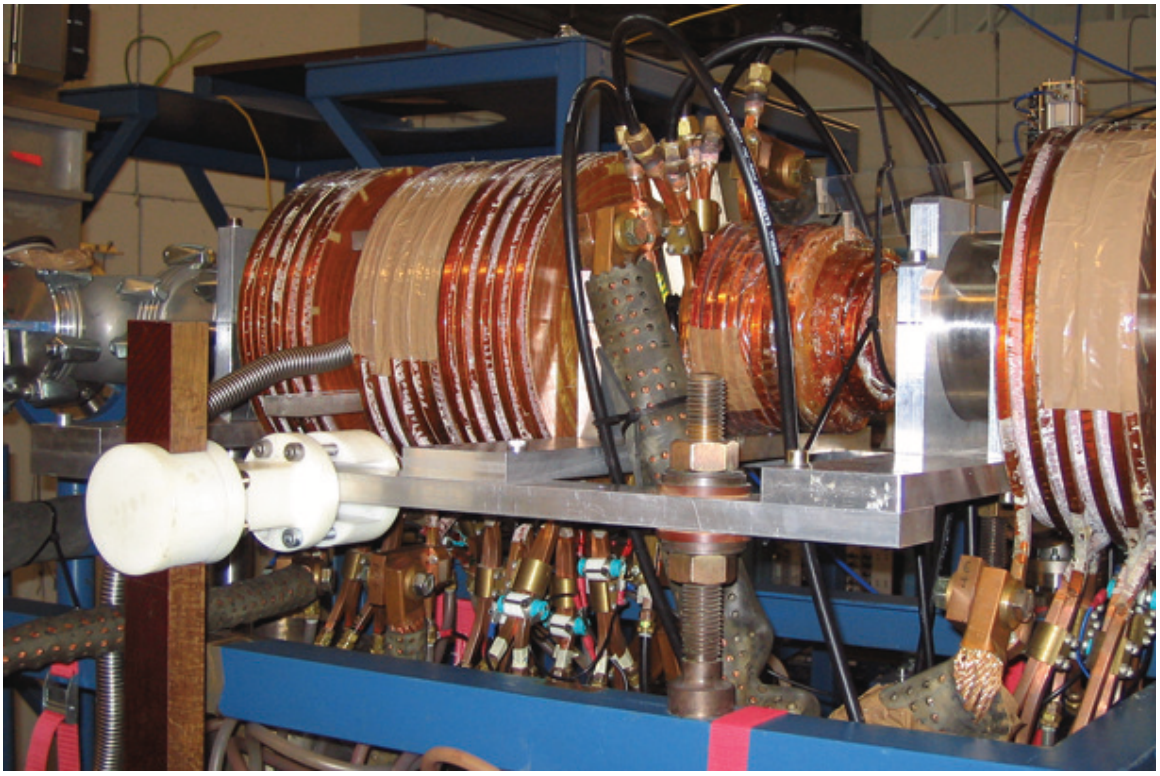

Figure 3.19: Photograph of one of the prototype coil setups.

The tests were made with a cooled to approximately -30° C, 25.4 mm^2 silicon PIN diode coupled to a PSC 761 preamplifier and a linear amplifier. A ^{133}Ba source was used and the current in the coils was between 560 A and 800 A. The main ICE

energies of ^{133}Ba are 45.0 keV, 75.3 keV, 124.6 keV, 240.4 keV, 266.9 keV, 320.0 keV and 350.5 keV. The magnetic field and transmission efficiency were simulated and then measured. The predicted and measured values follow the same trend, as shown in Figures 3.20 and 3.21. The discrepancies are due to system losses that were not taken into account in the simulations, like poor vacuum conditions, misalignment of the source and detector etc. A transmission efficiency between 10% and 5% in the 45-350 keV energy range was achieved.

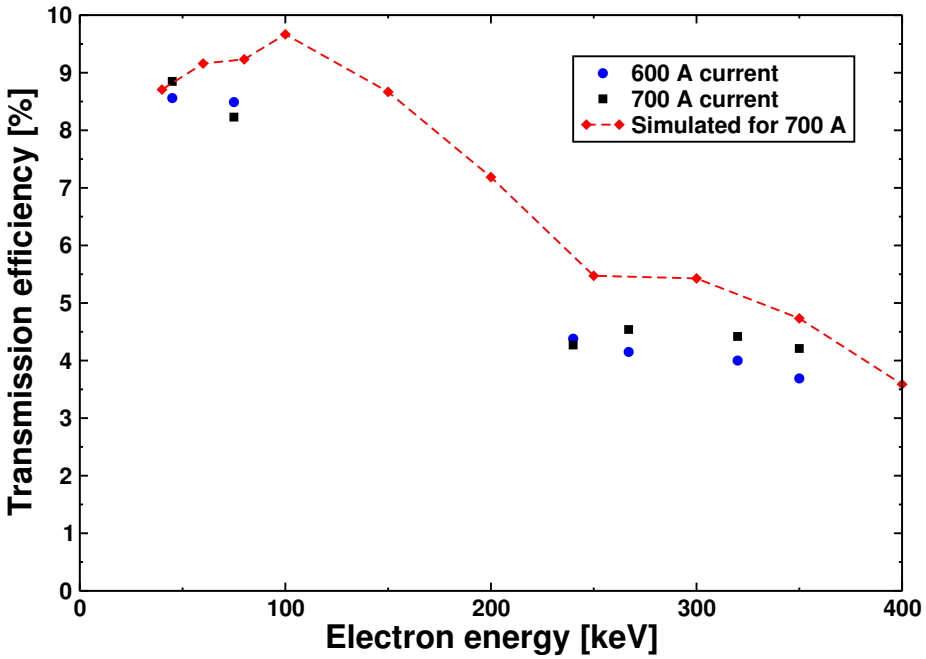

Figure 3.20: Measured and simulated electron transmission efficiency for the prototype presented in Figure 3.19.

The effect of the stray magnetic field induced by the prototype coils in the PMTs of the BGO shields of JUROGAM II and the amount of shielding needed to minimise it was studied. A BGO shield populated with PMTs in various positions was placed close to the coils at discrete angles allowing different distances between the PMTs and the coils.

In the worst case scenario, one of the PMTs was parallel to the coils and lying adjacent to them. In other cases the BGO shield was either at 45° or 90° with respect

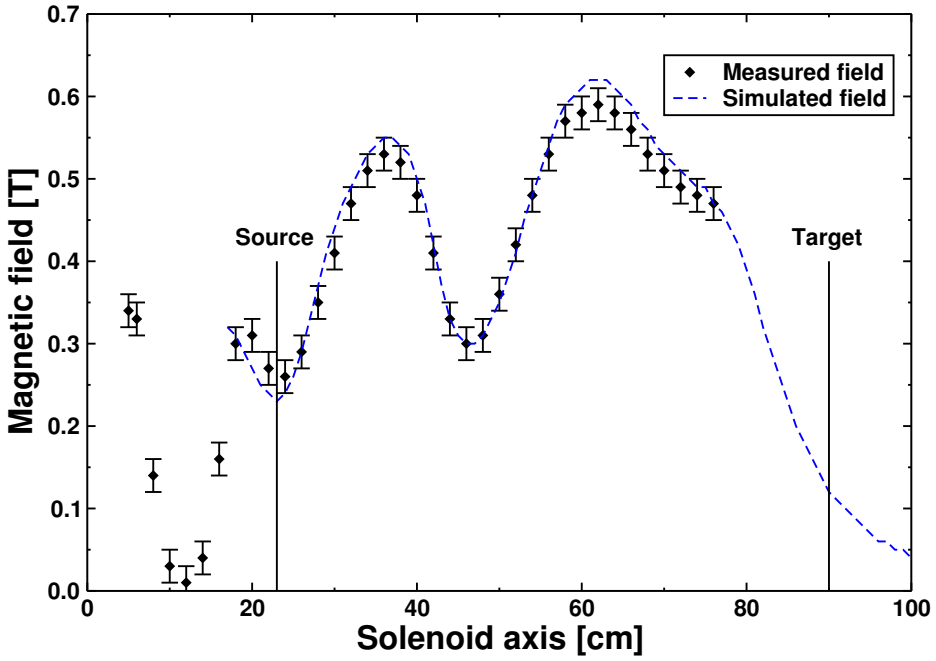

Figure 3.21: Measured and simulated magnetic field on the solenoid axis for the prototype presented in Figure 3.19.

to the solenoid axis. It was found that a 1 mm thick iron shield bent around the PMT significantly increased the overall performance. Additional shielding around the coils was used. A 2 cm thick iron shield was found adequate in most cases.

3.5 Electric field simulations

A large flux of low energy delta electrons is produced during the interaction of the beam and target particles. Like conversion electrons, these can be transported to the silicon detector generating a huge background in the low energy region. To reduce this flux an electric field gradient induced by a high-voltage barrier is employed between the target and the detector.

The energy of delta electrons depends on the energy of the projectile, E_a, the K-electron binding energy of the atoms of the target, E_k, and the electron and projectile masses m_e and m_a respectively. The maximum energy they can get for a certain target and projectile is given by [Kl69]:

$$E(\delta) = 4\left[\sqrt{\frac{m_e}{m_a}E_k E_a} + \frac{m_e}{m_a}E_a\right]. \tag{3.3}$$

A typical reaction for the study of nobelium is ^{48}Ca beam on lead target at 219 MeV. For this reaction Equation 3.3 gives maximum delta electron energy of approximately 69 keV.

The maximum voltage that can be applied to the SAGE high-voltage barrier is -50 kV, which is adequate to stop most of the low energy electrons. The high-voltage barrier geometry is presented in Figure 3.22 with the real barrier shown in Figure 3.23.

The high-voltage power supply is connected through a shielded, PVC-insulated cable to a resistor chain consisting of five 1 GΩ resistors. This in turn is connected to a ceramic high-voltage vacuum feedthrough to the beam pipe. The voltage is applied to the electrode using the horseshoe shaped connector shown in Figure 3.24. An unshielded PVC-insulated cable connects the feedthrough with the horseshoe which is placed inside the electrode.

Both the electrode and the horseshoe are made of stainless steel and the electrode has rounded edges. This is a precaution as field density increases at sharp edges and consequently increases the possibility of producing discharges. For the same reason the inner bore and edges of the electrode are highly polished.

A Noryl insulation sleeve surrounds the electrode and is longer than it, with

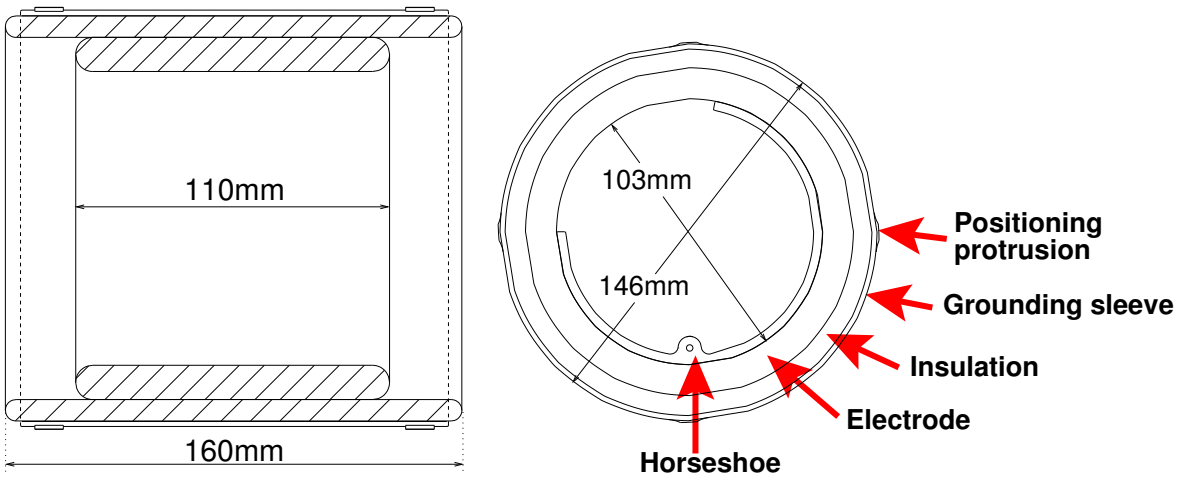

Figure 3.22: Cross-sections of the high-voltage barrier, parallel to the beam (left) and perpendicular to it (right).

both edges extending further to ensure that no flashovers can occur between the high-voltage barrier and any grounded surfaces, such as the inside of the beam pipe. Such discharges could destroy the silicon detector or some of the preamplifiers. The Noryl insulator has dielectric constant of 2.7, breakdown voltage of 16-20 kV/mm [Ol97, Go98] and is 7.5 mm thick, more than enough to safely prevent a breakdown at maximum voltage. A thin aluminium grounding sleeve is wrapped on the outside of the insulation providing a more uniform grounding plane around the electrode.

The Noryl insulator has 0 V potential on one side and -50 kV on the other which causes a high stress potential gradient across it. Should a flashover occur either in the insulator or due to impurities in the vacuum, then the voltage will drop in the resistor chain that is attached to the high-voltage cable on the outside of the chamber thus quenching the discharge to prevent damage.

The high-voltage barrier can be considered as a cylindrical capacitor with capacitance given by:

$$C = \frac{2\pi\epsilon_0\epsilon_k L}{ln\frac{r_{out}}{r_{in}}} = 73.47\,pF, \tag{3.4}$$

where ϵ_0 and ϵ_k are the dielectric constants of vacuum and Noryl respectively, L is

Figure 3.23: A picture of the finalised high-voltage barrier.

the length of the barrier and r_{out}, r_{in} its outer and inner radii.

The barrier along with the resistor chain form a low-pass filter with characteristic time RC=367 ms (Figure 3.25). This means that should a discharge occur it will take 367 ms for the barrier to charge up to 63 % of the input voltage or about 1.8 s to fully charge up.

All the individual parts of the high-voltage barrier form a rigid unit carefully machined to avoid the presence of any trapped air volumes between the individual parts. To further reduce this possibility, the unit is positioned inside the beam pipe using small protrusions on the outside of the grounding sleeve.

The high-voltage barrier is a crucial component of SAGE, since a sudden discharge of such a high voltage could destroy sensitive electronic equipment or even cause a fatality. To ensure a safe working environment everything is well shielded and insulated, and during the design process a number of simulations were conducted to recognise any faults and indicate where additional insulation would be required.

Three-dimensional simulations were made with OPERA 3D [VF07] where the high-

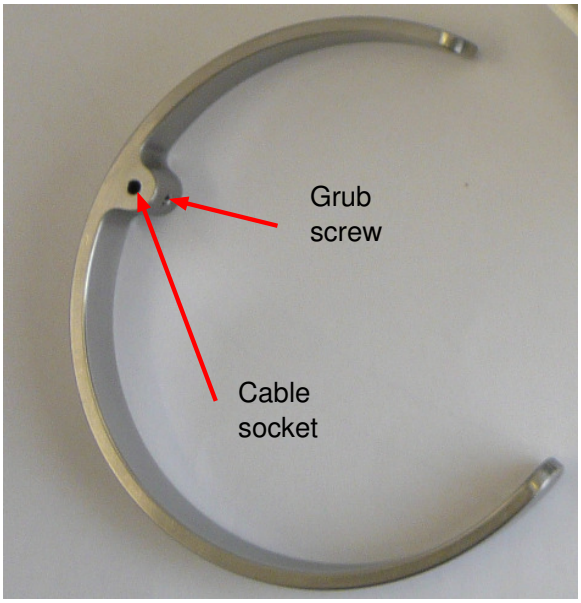

Figure 3.24: The horseshoe connector used to charge the high-voltage barrier. The cable plugs into the socket and is held in position by a grub screw.

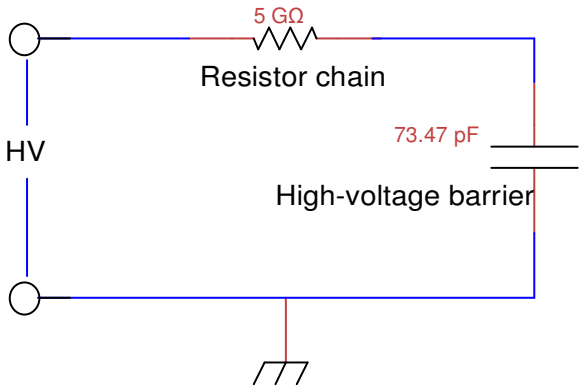

Figure 3.25: The circuit formed by the resistor chain and the high-voltage barrier.

voltage barrier and the power cable were simulated along with the coil support, illustrated in Figure 3.26. With these simulations a design was chosen where high field concentrations are minimised. The resulting electric field and high voltage profile are presented in Figure 3.27, which was produced using FEMM [Me06].

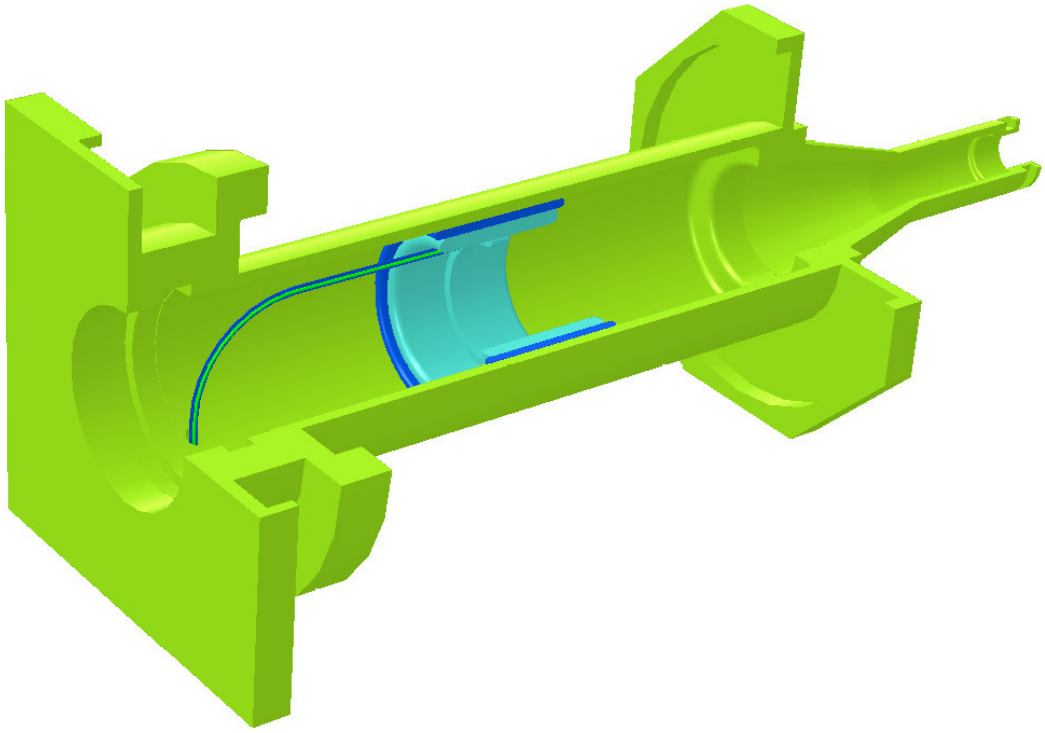

Figure 3.26: A perspective view of the setup used for the OPERA 3D simulations. The high-voltage barrier, the cable and the beam pipe are shown.

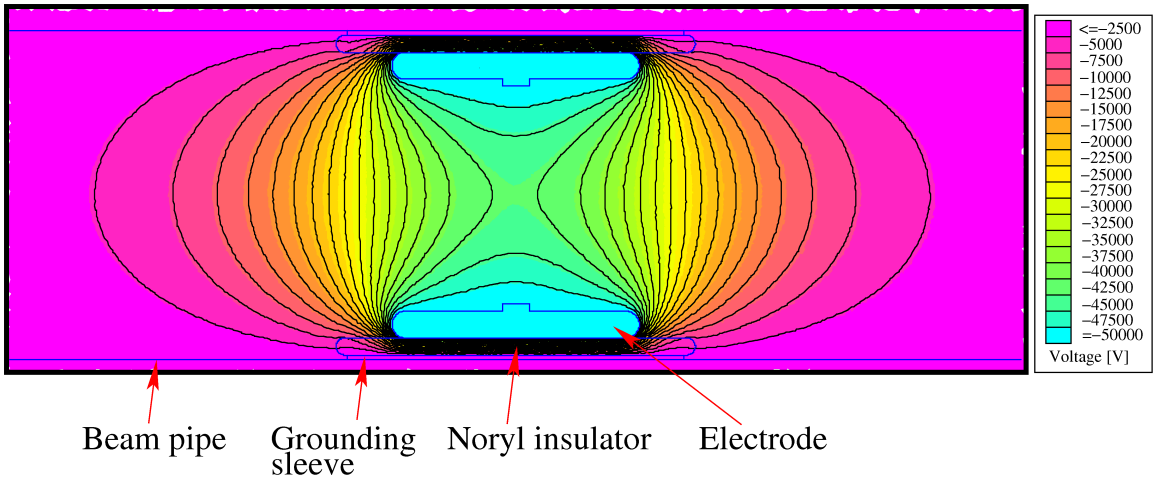

Figure 3.27: The electric field potential of the high-voltage barrier. In this simulation the high-voltage supply cable is not taken into account.

3.6 Electron transmission efficiency simulations

A very important factor for the good performance of SAGE is optimisation of the electron transmission efficiency. To simulate the transmission efficiency, the Monte Carlo computer code SOLENOID [Bu96] was used. The geometry of the setup (detector, beam line, carbon foil unit, silicon detector) was integrated in the code. A cascade of electrons of various energies was produced and uniformly emitted at the target position. The amount of electrons that either reached the detector or were lost in the way (both through interactions with the electromagnetic fields or the surrounding material) was calculated.

As in the case of the magnetic field simulations, where different solenoid coil geometries were studied, different geometries were considered in the transmission efficiency's case. Because the transmission efficiency depends on the magnetic and electric fields it was considered before performing any major changes on the solenoid coils and the high-voltage barrier.

The results presented here are for the finalised setup geometry. The solenoid coils are as described in Section 3.4 and the high-voltage barrier and carbon foil unit as in Sections 3.5 and 3.8 respectively. The silicon detector is described in Section 4.1 and is 1 mm thick. The simulated electron transmission efficiency is presented in Figure 3.28. The magnetic field was calculated for 1000 A current and the electric for -30 kV on the high-voltage barrier.

The transmission efficiency increases rapidly with increasing energy until about 160 keV, then until 360 keV it is roughly constant around 7.5 %. It then gradually decreases with increasing energy. This behaviour can be explained as at lower energies more electrons are absorbed inside the target and carbon foils or are reflected by the electromagnetic fields. The magnetic field is not strong enough to constrain higher energy electrons thus the number reaching the detector decreases above 360 keV. Additionally the 1 mm thick silicon detector used in these simulations is efficient for electron detection up to roughly 500 keV, this also affects the amount of detected electrons are higher energies.

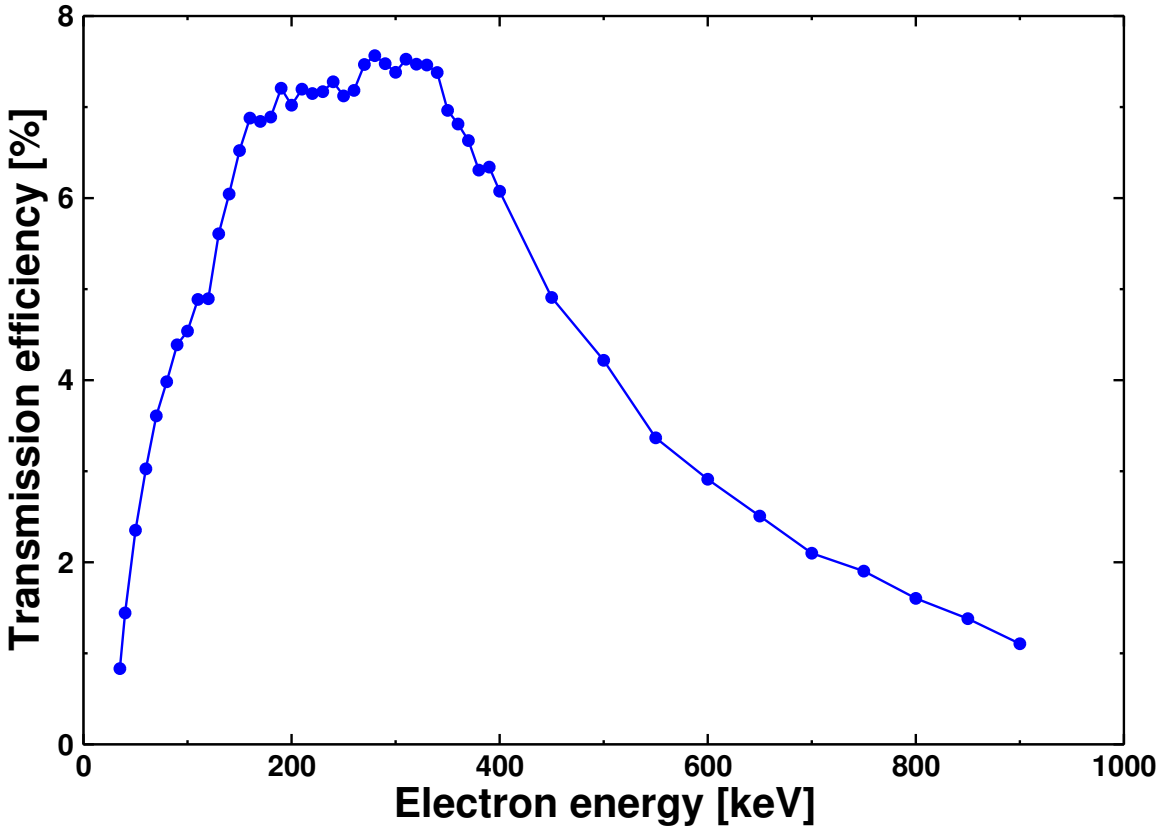

Figure 3.28: Simulated electron transmission and detection efficiency when using a 1 mm thick detector. Magnetic field calculated for 1000 A current through the coils and electric field for -30 kV on the high-voltage barrier.

The energy dependence of the major loss mechanisms is plotted in Figure 3.29. At higher energies the bottleneck is the radius of the carbon foil unit (aperture in Figure 3.29). At lower energies different mechanisms compete with the reflection of electrons from the electromagnetic fields being the most prominent. In the simulation output the same electron may be included in more than one category. For example the same electron can be reflected by the electromagnetic fields and consequently absorbed in the carbon foils. This can lead to the total losses to be presented as greater than 100 %.

The electron distribution on the detector surface is also something that was con-

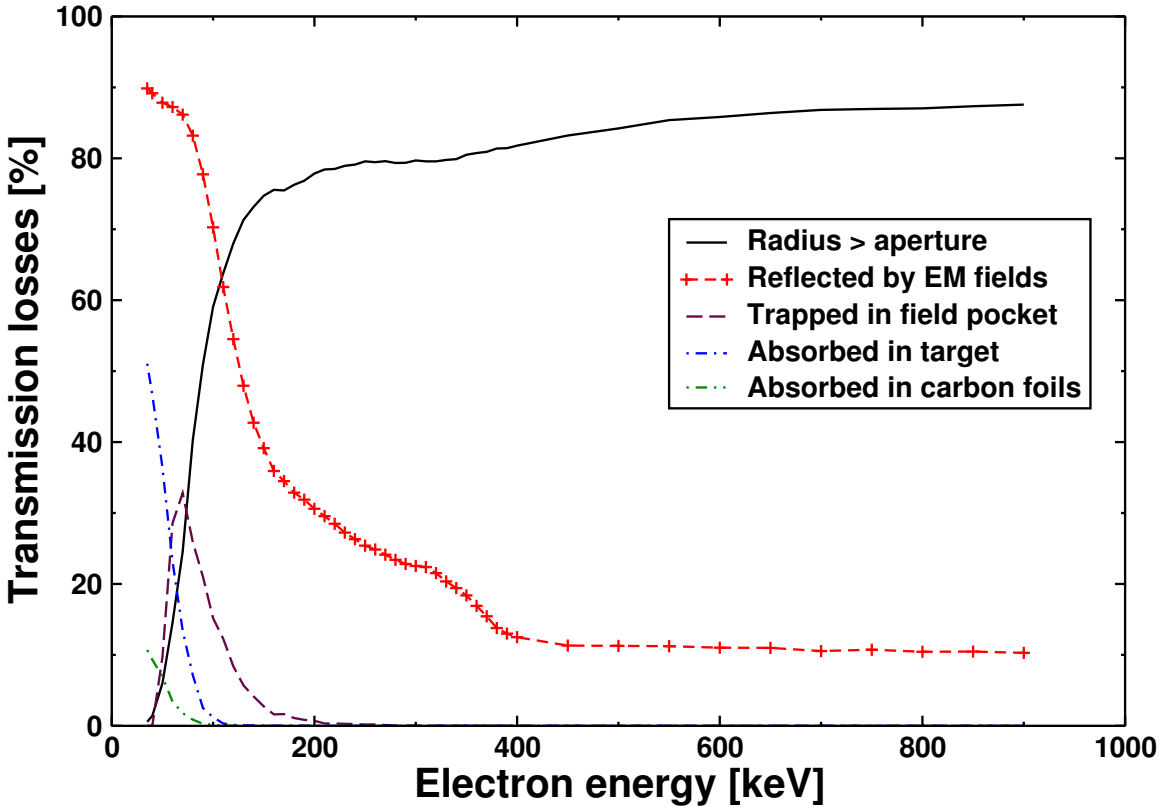

Figure 3.29: Percentage losses of electrons per energy as calculated from the simulations. Aperture is the carbon foil unit and EM fields the electromagnetic fields of the setup. The total losses are shown greater than 100 % in some energies for the reasons explained in the text. 1000 A current through the coils and -30 kV on the high-voltage barrier were used in the simulations.

sidered in design. In Section 3.3 the positioning of the detector in an optimum magnetic field strength was discussed. From the SOLENOID simulation, the percentage of conversion electrons measured by each area of the detector, were calculated (Figure 3.30). The main areas are namely the central pixel, inner rings and outer rings and are presented in more detail in Section 4.1.

As expected at lower energies most of the electrons are measured by the inner detector rings. This is because the focusing power of the solenoid coils is proportional to the transverse momentum of the electrons ($r \propto \frac{p_\perp}{B}$, see Appendix A). At higher

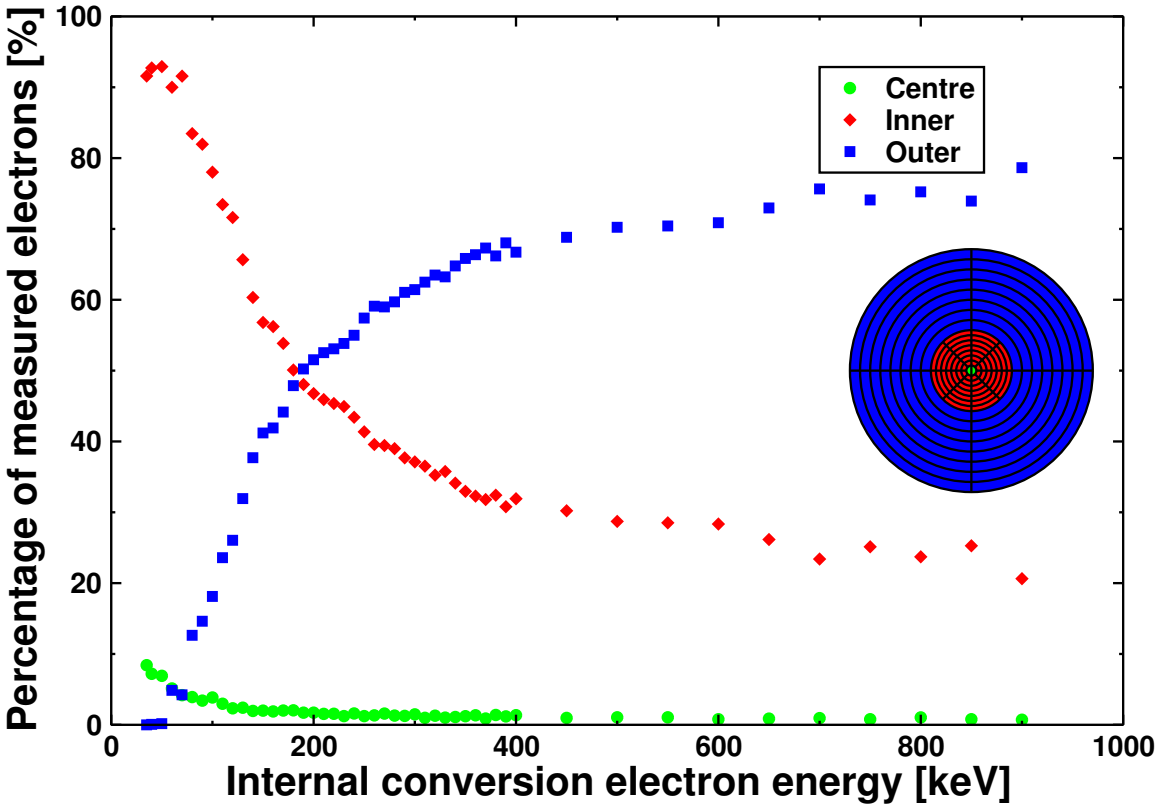

Figure 3.30: Percentage of measured electrons per detector section per energy. Centre refers to central pixel and inner and outer to the corresponding rings of the detector. The data series are colour-coded according to the detector layout shown in the graph. 1000 A current through the coils and -30 kV on the high-voltage barrier were used in the simulations.

energies the outer segments give higher count rates for the same reason. The central pixel acts similarly to the inner rings.

Due to the high delta-electron background higher segmentation is chosen for the central pixels. This allows more evenly distributed count rate over the detector. Rate distribution estimates are further discussed in Section 3.7.

It should be stressed that the transmission efficiency should be calculated separately for each SAGE experiment, because the calculated values depend on target thickness, recoil energy, angular distribution of the emitted electrons and different

electric and magnetic field strengths. The Monte Carlo code allows the user to do this very quickly and since the electric and magnetic fields only require scaling when different voltage and current is used the whole process is fairly straight forward.

3.7 Silicon detector rate distribution estimates

The SAGE silicon detector had to be designed in a way that allows the use of high intensity beams and offers an evenly distributed count rate throughout its surface. It was not possible to build prototype detectors because of the high manufacturing cost and long delivery times, so a set of calculations were made trying to find the best design.

As a starting point the SACRED silicon detector [Ka04] and the count rate distribution measurement from a ^{254}No experiment [Bu02] using this detector was taken. It was found that for the SACRED detector the rate density as a function of segment radius follows the equation:

$$f(r) = \frac{a}{1 + (\frac{r}{b})^3}, \tag{3.5}$$

where a and b are constants. This function has no physical weight and was an educated guess. The agreement between data and function are shown better by integrating the function over the geometry of the detector. By applying each detector ring's inner and outer radii as limits to the integration and then dividing the resulting value by the number of segments per ring the count rate per segment was calculated. All the above values are presented in Figure 3.31.

Other detector geometries were studied by integrating the function given in Equation 3.5 with different limits and the following constraints were applied to ensure realistic results. The angle of the beam and the solenoid axes was kept at 2.5° and the magnetic field properties were the same as in SACRED. The spacing between the detector segments was kept at 0.1 μm, the detector diameter at 60 mm and its distance from the target at 90 cm.

The final geometry selected gives the most evenly distributed count rate from all

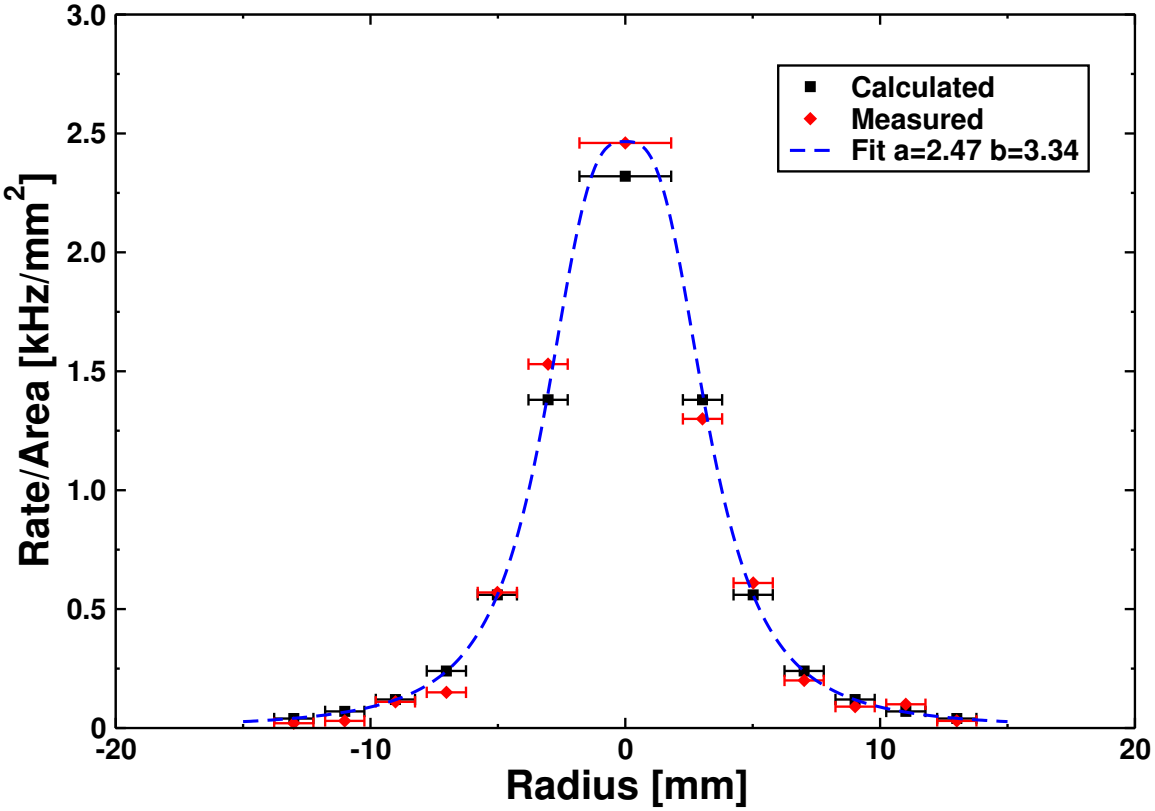

Figure 3.31: Comparison between the measured and calculated count rate distributions of the SACRED detector. A fit using Equation 3.5 with a=2.47 and b=3.34 is also shown.

the studied geometries. By further dividing the inner rings and central pixel, higher count rates are achieved because the distribution does not peak in the centre, as shown in Figure 3.32.

A second set of calculations was made to study the effect of detector displacement on count rate distribution. The same method as above was used but this time a two dimensional grid was defined with each point of the grid having a relative value given by the count rate distribution function. The detector was displaced and the area covered by each segment integrated to give the new count rate. The displacement was made along the 22.5° diagonal. This represents a worst case scenario as the count rate peaks mainly in one segment.

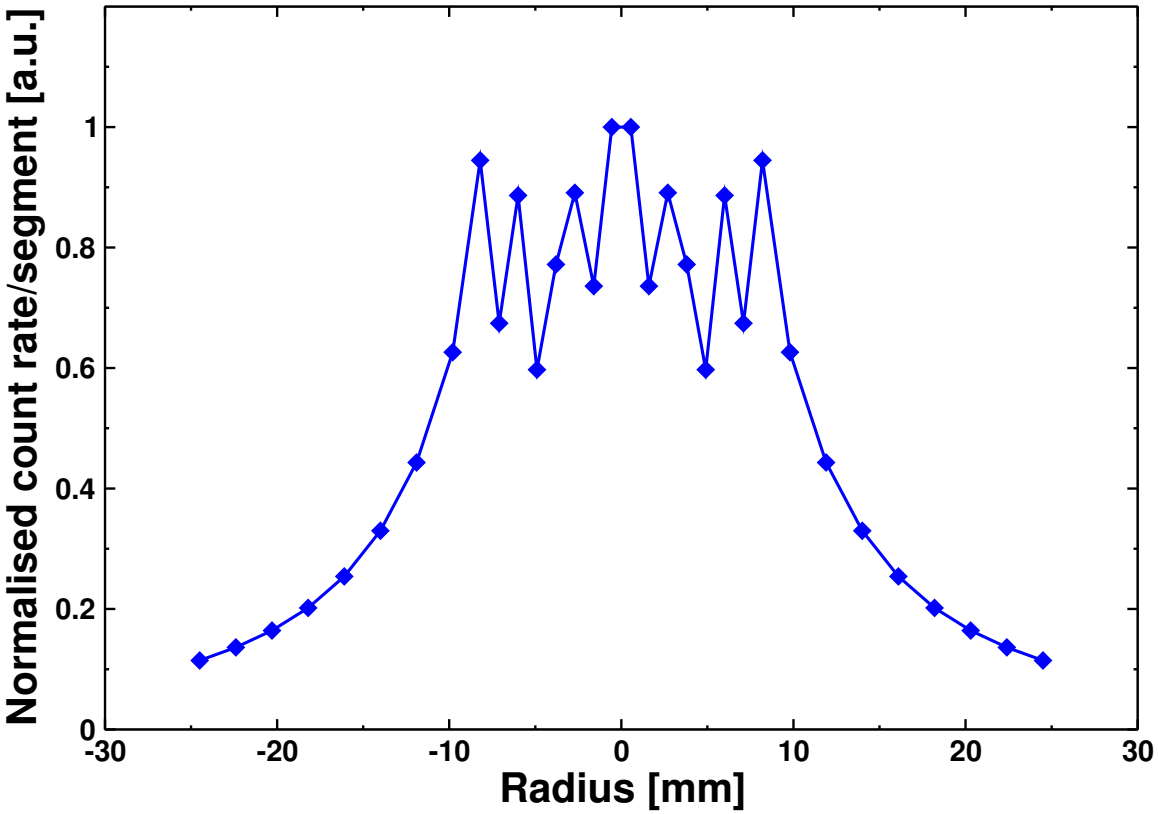

Figure 3.32: Normalised count rate distribution per detector segment for SAGE. The distribution does not peak in the centre as it did in SACRED but is more evenly spread.

This exercise showed that the detector must be precisely positioned otherwise the count rate at various segments would increase drastically, as demonstrated in Figure 3.33. The results are normalised so that for a centred detector the count rate in the highest counting pixel equals one.

A fine position adjustment mechanism is integrated in the detector support to correct for any misalignment (see Figure 3.34). The support structure is mounted on rails connected to the detector chamber door and moves on the vertical and horizontal axes using stepper motors. The system allows for ± 6 mm movement on both axes, restricted by limit switches.

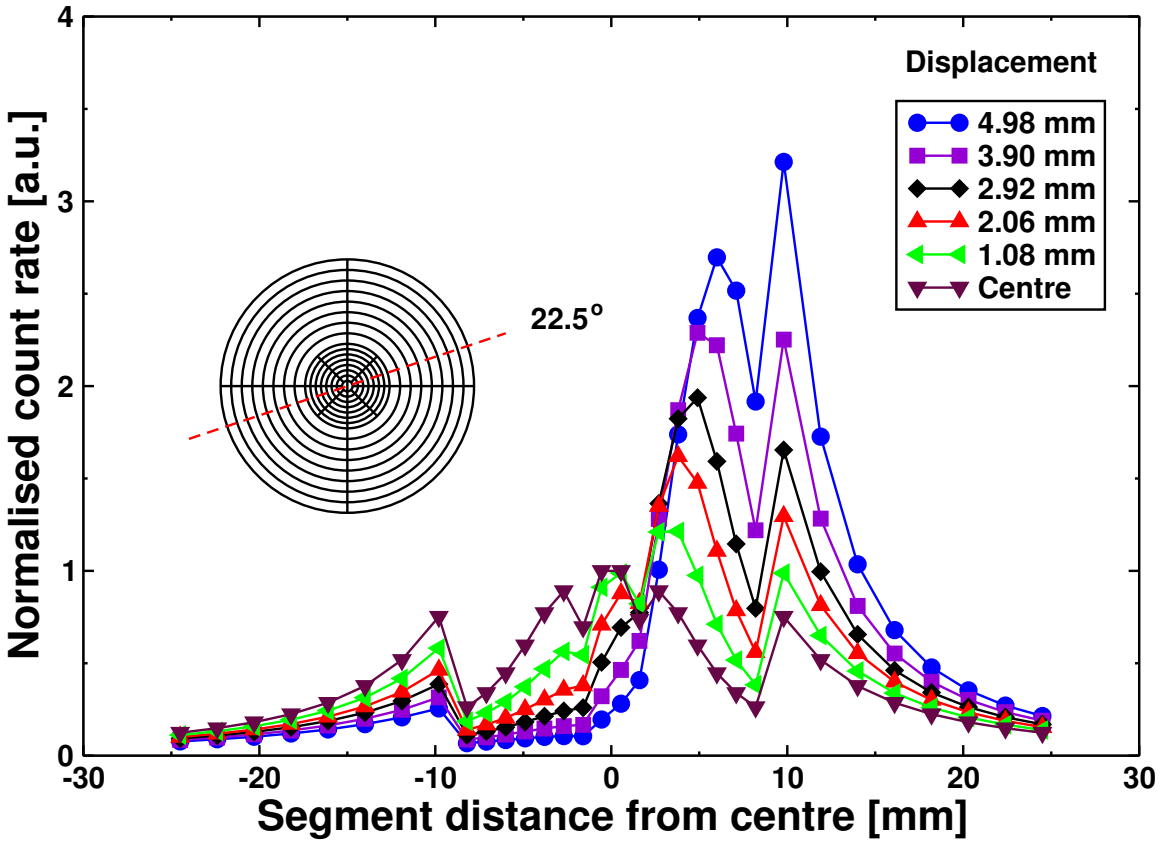

Figure 3.33: Normalised count rate of the fastest counting segment per ring as a function of detector displacement. The displacement is made along the 22.5° diagonal. The normalisation is done so that the maximum count rate when the detector is centred equals one.

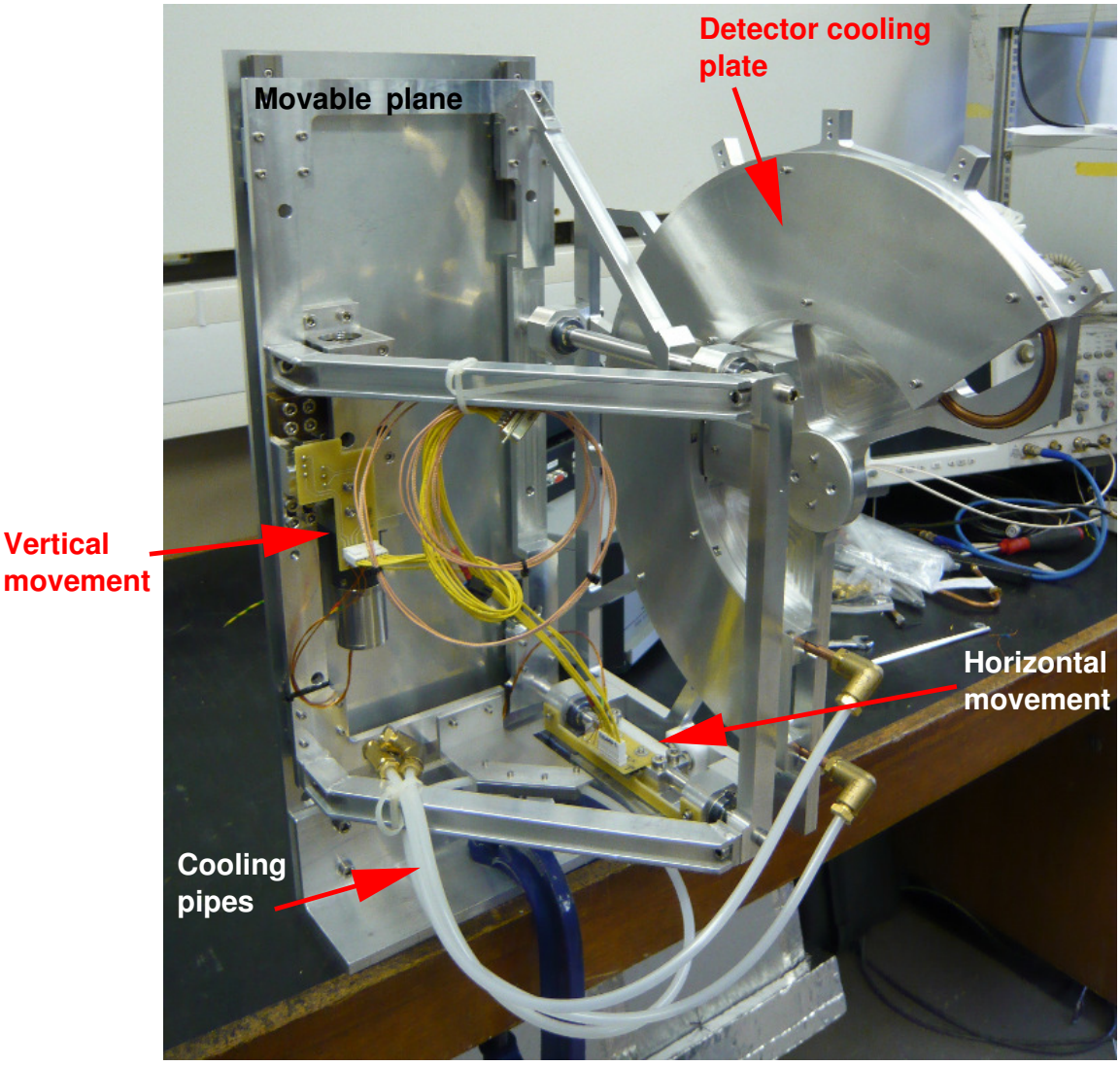

Figure 3.34: A picture of the silicon detector support frame where the fine position adjustment of the detector takes place. The frame is mounted on a dummy plate used during manufacture and testing.

3.8 The vacuum and pumping arrangement

Appropriate vacuum conditions are vital for the correct operation of SAGE. The bulk of the spectrometer can be separated into two main pumping volumes. RITU, that operates using 1 mbar helium gas and the high-voltage barrier region that requires a high vacuum for proper operation. These two volumes need to be well separated, while ensuring good electron transmission.

Good vacuum is necessary in the region of the high-voltage barrier as any impurities, mainly helium particles and water vapour, can cause discharges of the barrier. The beam can interact with residual gas molecules (contaminants) ionising them producing a flux of electrons which aided by the electric and magnetic fields are accelerated and transmitted to the detector, resulting in a large background.

In [Ka04] a study was made to find the best way to minimise the amount of helium in the region of the high-voltage barrier. It was shown that separating the two regions with a single $40\,\mu g/cm^2$ carbon foil gives at best 10^{-5} mbar pressure, which is inadequate. The carbon foil would collapse at higher pressure differences and helium gas leaked through it preventing better vacuum conditions.

This is overcome by employing a unit using two $50\,\mu g/cm^2$ carbon foils with intermediate pumping (Figure 3.35). Adequate pressure (10^{-6} - 10^{-7} mbar) is achieved this way. To prevent leaks around the carbon foil unit a piston seal is used. Helium particles diffuse through the carbon foils at a slow rate but have no major effect on the pressure in the high-voltage barrier region.

Transmission efficiency simulations showed that the best position for the carbon foil unit is upstream of the target. If it is positioned downstream of the target it significantly reduces the recoil transmission into RITU and prevents gas cooling of the target.

To further improve the vacuum a cold trap (see Figure 3.36) is positioned below the detector chamber and cooled with liquid nitrogen through a cold finger to approximately -50° C. The cold trap removes water vapour and gases from the pumping stream by sublimating the gas molecules on the trap surface. This means that the

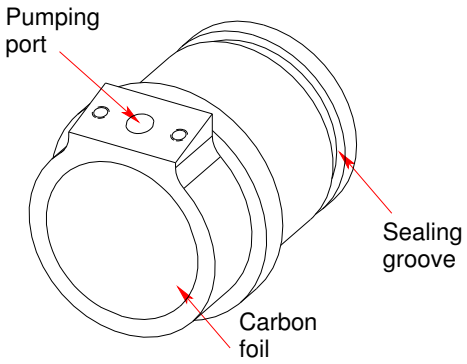

Figure 3.35: A schematic diagram of the carbon foil unit, showing the pumping port and the sealing groove.

gas molecules transform from the gas phase to a solid crystalline phase, bypassing the liquid phase.

If the cold trap was not present, any impurities would be attracted towards the cold surface of the detector. Impurities implanted on the detector surface could locally alter its electric field configuration, form conductive bridges between neighbouring pixels decreasing the inter-strip resistance [Ha09] or interact with the incident electrons, affecting the resolution of the detector.

The pumping scheme is shown in Figure 3.37. The spectrometer is separated from the beam line and RITU with gate valves. Pumping to 10^{-2}-10^{-3} mbar can be done separately for each volume using the rotary vane pump and lower pressures are reached using a 1200 l/s turbo pump.

In normal operation all volumes are pumped simultaneously first with the rotary vane pump through the needle valve and then with the turbo pump until equilibrium is reached throughout the spectrometer volume. Then the gate valve to RITU (that is in vacuum mode) is opened and while pumping the carbon foil unit with the rotary vane pump, helium is slowly introduced in the system.

Continuous monitoring of the pressure in each volume is made with manometers, from atmospheric pressure to a few millibar, and with Pirani/cold cathode full range gauges for pressures down to 10^{-7} mbar.

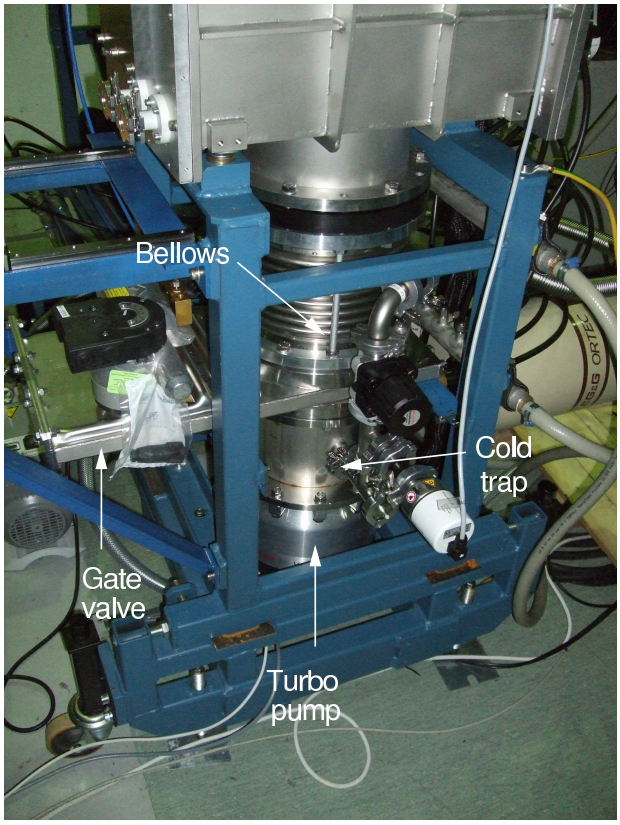

Figure 3.36: A photograph of the pumping station positioned under the detector chamber. The turbo pump and cold trap can be seen.

By closing gate valves G1, G2 and the beam line gate valve one gains access to the detector without venting the whole system. In this case valve v2 allows continuous pumping of the high voltage region through the turbo pump. To gain access to the target region while keeping the detector chamber under vacuum gate valve G2 and the RITU gate valve are closed.

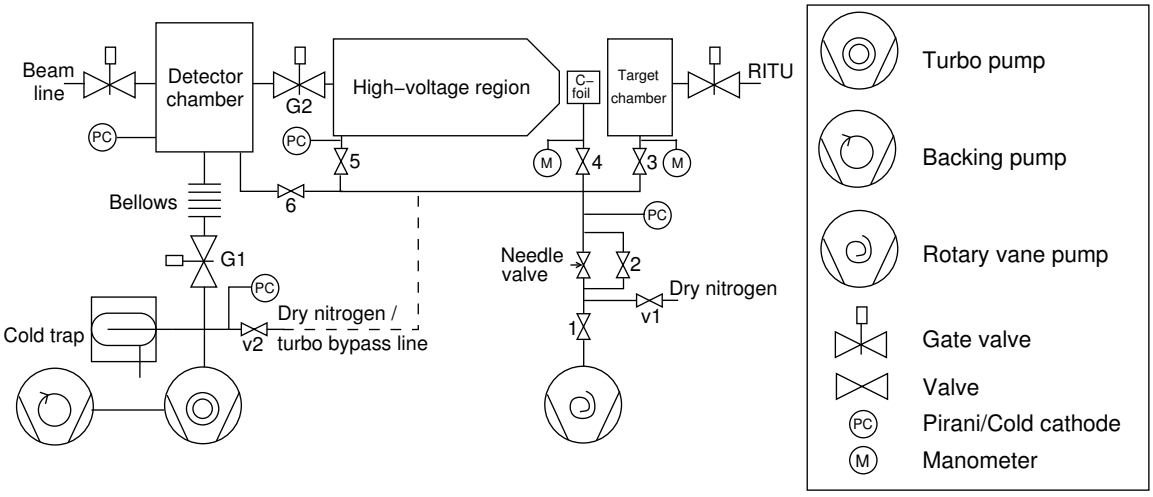

Figure 3.37: The vacuum control system for the SAGE spectrometer.

Chapter 4

Detector and Electronics

4.1 The SAGE silicon detector

4.1.1 The silicon detector properties

The silicon detector used in the SAGE spectrometer (Figure 4.1) is 1 mm thick and has a concentric ring structure. It is divided into 90 individual segments with the geometry shown in Figure 4.2. The numbering scheme of the detector pixels is presented in the same figure. The central pixel of the detector is divided into two semicircles with 1 mm radius (pixels 1 and 2). Following these are the 7 inner rings which are 1 mm wide and each one is split into 8 segments (pixels 3 to 58). The 8 outer rings are 2 mm wide and are divided into 4 segments each (pixels 59-90), making the overall diameter of the active part of the detector 48 mm. The capacitance of the larger detector segments is roughly 10 pF reducing to about 0.2 pF for the central pixel.

By taking a closer look at the detector one can see that the inter-strip gaps separating the segments are 70 μm wide. The way the separation is made is shown in Figure 4.3. The strip pitch is 1 mm measured from the end of one strip to the end of the next. For example lets consider the centre of the detector to be at the origin. The end of the central segment is at 1 mm, following this is a 70 μm wide inter-strip gap. The second strip is between 1.07 mm and 2 mm. Then an inter-strip gap and so on.

Taking into account the inactive areas that separate strips into individual segments gives a total inactive area for the detector of approximately 4%.

Surrounding the active segments of the detector are a series of guard rings [Ka67]. These shape the electric field, reducing edge effects and providing a homogeneous potential to all the strips, increase the breakdown voltage of the detector and reduce the leakage current by collecting its surface component [Br83, Mi05, Ha09]. These factors improve the overall performance of the silicon detector. The various technical design characteristics of the detector are presented in Table 4.1. This detector design was chosen for the reasons explained in Section 3.7.

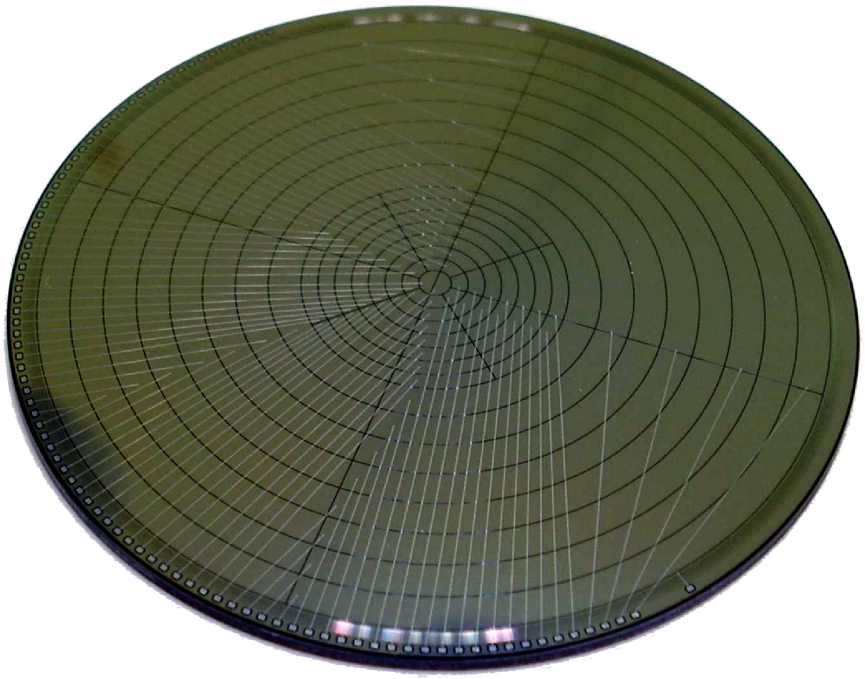

Figure 4.1: Photograph of the SAGE silicon detector. The detector segmentation and signal wires are clearly visible.

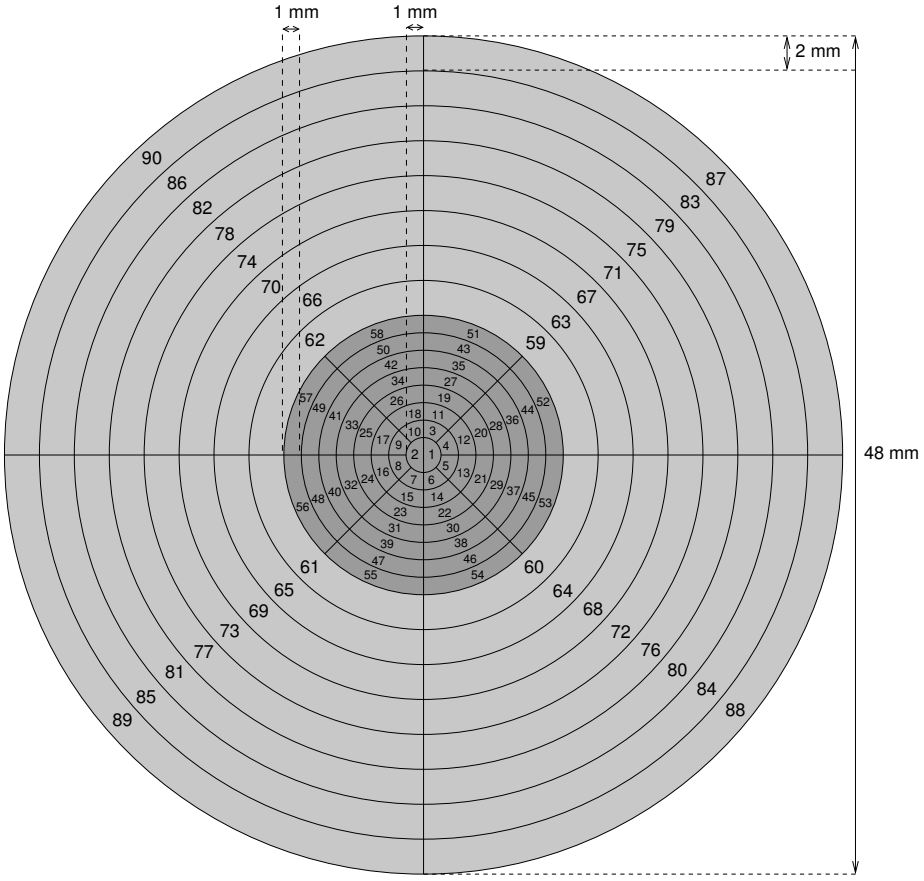

Figure 4.2: The geometry of the SAGE silicon detector. The numbers and dimensions of the individual pixels are shown.

4.1.2 The detector Printed Circuit Board layout

A PCB was designed to accommodate the silicon detector and the 90 preamplifiers. The preamplifiers used are the CAEN A1422 that are described in Subsection 4.2.3. The layout is such that all the channels are equivalent with the preamplifiers positioned equidistantly from the detector and having individual power supply filtering. The circuit diagram of a single detector channel is shown in Figure 4.4 and the layout of the PCB in Figure 4.5. The outputs are divided into groups of ten channels and are taken through 9 25-way D-type connectors on the feedthrough plate of the vacuum chamber. These are connected to the PCB through flexible ribbon cables that are also

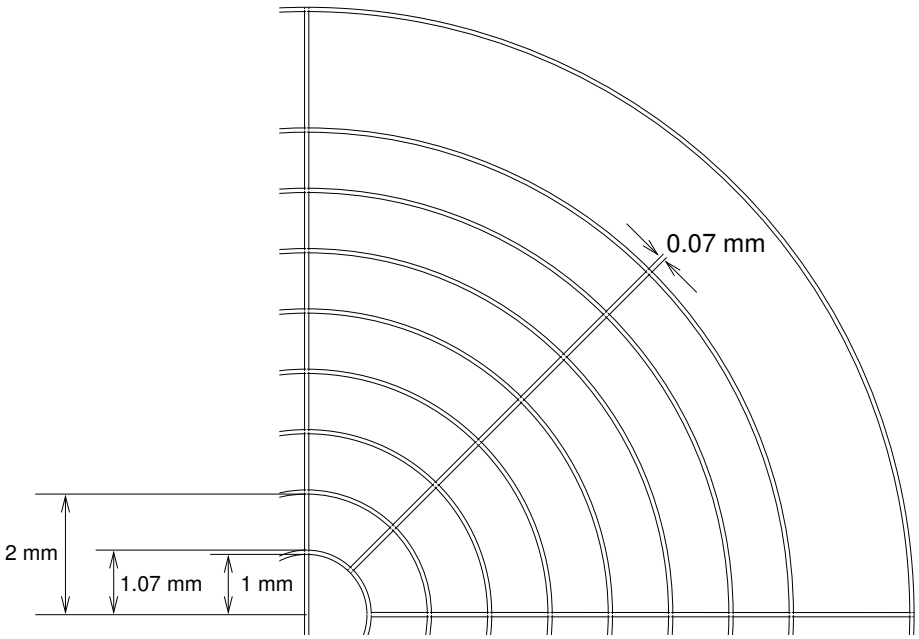

Figure 4.3: Detail of the central part of the SAGE silicon detector. The 70 μm wide inactive strips between the active segments are shown.

used for powering the preamplifiers. Micro coaxial cables are under consideration for replacing the ribbon cables as they are better shielded and will reduce noise pickup. The ribbon cables plug into 26-way side-latch headers on the PCB. On the outside of the chamber, small adaptor boxes connect into each of the D-type connectors to convert the D-type to SMA (sub-miniature version A) connectors.

The bias voltage is applied either directly through a bias resistor to the back side of the detector or through the preamplifiers. Both these methods are integrated in the PCB design so that if one method introduces noise in the system the other will be used. The two methods are interchangeable by means of a jumper but the default bias method is through the bias resistor.

The PCB is placed in high vacuum of the order of 10^{-7} mbar. The detector and preamplifiers are cooled through contact and radiative cooling using a refrigerated circulator with ethanol as the refrigerant. The ethanol circulates through the cooling plate as shown in Figure 4.6.

Table 4.1: Design technical specifications of the SAGE silicon detector as defined by the manufacturer.

Characteristic	Value
Outer diameter	50 mm
Detector thickness	1000 μm
Full depletion (FD)	150 V typical
	200 V maximum
Total leakage current	1 μA typical
(FD+30 V at 20°C)	3 μA maximum
Estimated capacitance	11 pF/cm^2 for Si
	1 pF/cm^2 for tracks
Electron cut-off energy	4 keV

4.1.3 Offline detector testing

The detector was tested by the manufacturer by connecting all the segments together and measuring the overall capacitance and current at different bias voltages. The measurements were made in a light-sealed chamber, at 20-21° C temperature and humidity of 35-60 %. From these, one can determine the full depletion bias voltage region and also how resistive the detector is. The results from these measurements are presented in Figure 4.7.

The detector becomes fully depleted around 128 V, as seen in Figure 4.7(a). This is explained if we consider that the depletion region of the detector simulates a charged capacitor. By increasing the reverse bias voltage the depletion region increases and the capacitance decreases [Kn00]. When the detector becomes fully depleted the capacitance is almost constant.

In Figure 4.7(b) the voltage-current characteristics of the detector are shown. Its operational region is between V_{min} and V_{max} which ideally should be flat. This would

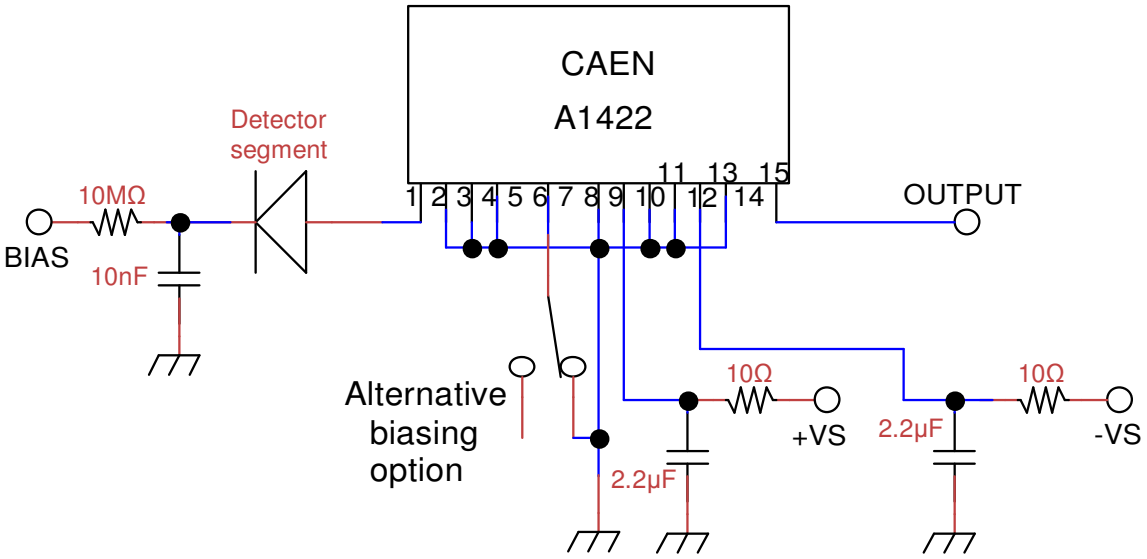

Figure 4.4: Circuit diagram for one channel of the detector PCB, employing a CAEN A1422 preamplifier. The bias and preamplifier power supply filtering circuits can be seen.

allow the detector to be operated at higher bias voltages and hence have lower capacitance. This can be achieved by cooling the detector to reduce the leakage current and consequently the electronic noise and so improving the resolution. Beyond V_{max} the current increases rapidly. This is due to ionisation of atoms in the detector material that produce free charge carriers. This decreases the resistance of the detector material causing an increasing current flow [Sm78].

The detector was bonded to the assembled PCB for further testing. After mounting the PCB to the detector cooling plate the preamplifiers were connected as shown in Figure 4.6. To ensure a quiet testing environment that additionally resembles the experimental conditions, the PCB was placed inside a screened box and the D-type to SMA converter boxes were used in the output.

Most of the channels were tested with cosmic radiation and all of them with the 59.54-keV γ-ray of an ^{241}Am source. Oscilloscope screen-shots from the tests are presented in Figures 4.8 and 4.9. The tests were made in air and no detector cooling

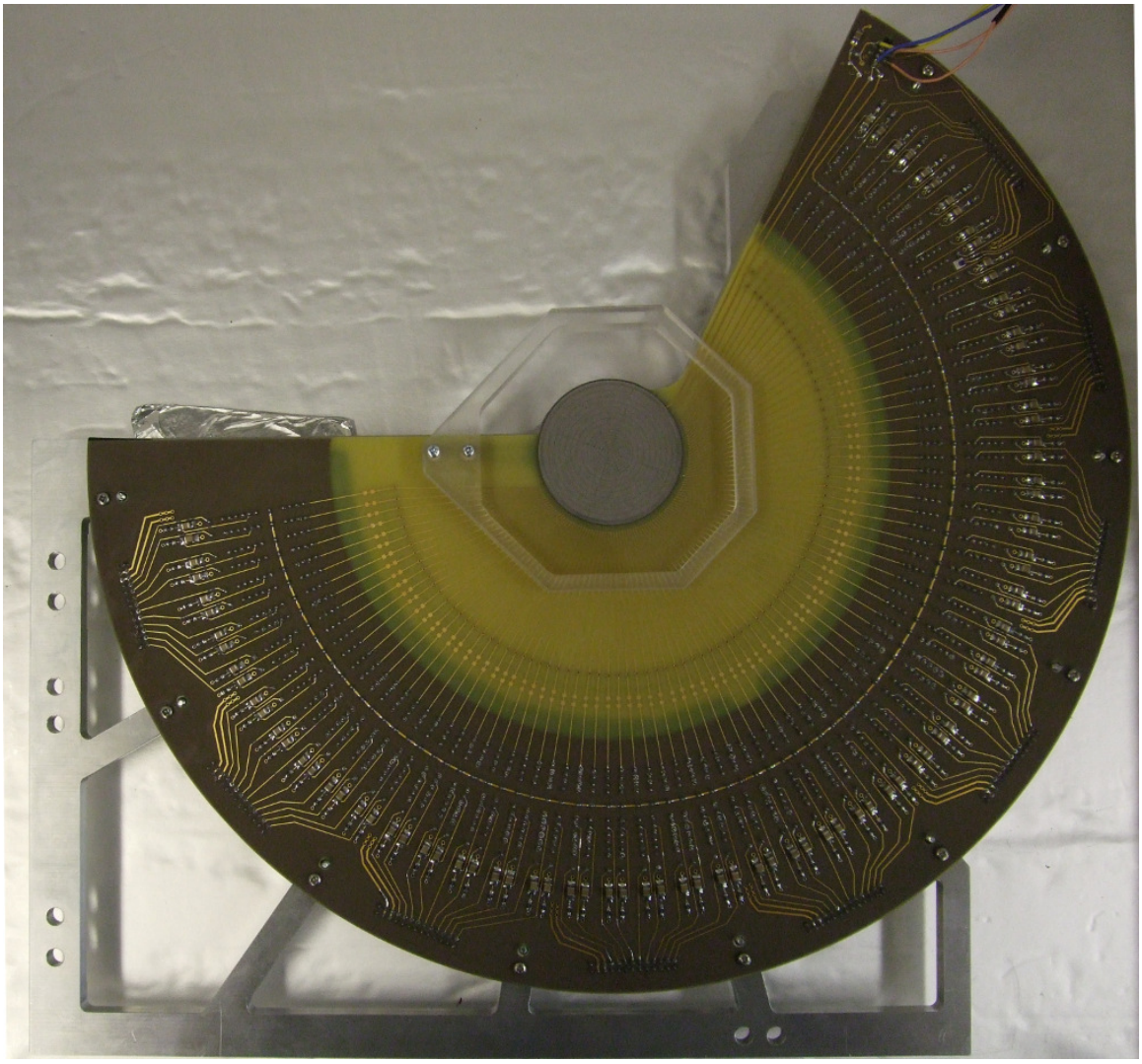

Figure 4.5: Photograph of the detector PCB mounted on the detector cooling plate as seen from the front. The detector is situated behind a protective Perspex cover.

was used. The power dissipation from the preamplifiers (276 mW per preamplifier) caused a temperature increase on the PCB which in the final implementation will be avoided by cooling.

The overall results of these tests are highly satisfactory. The completed, fully populated PCB with mounted detector and preamplifiers, has a low noise level (approximately 4 mV baseline noise) and no cross talk between the channels is observed.

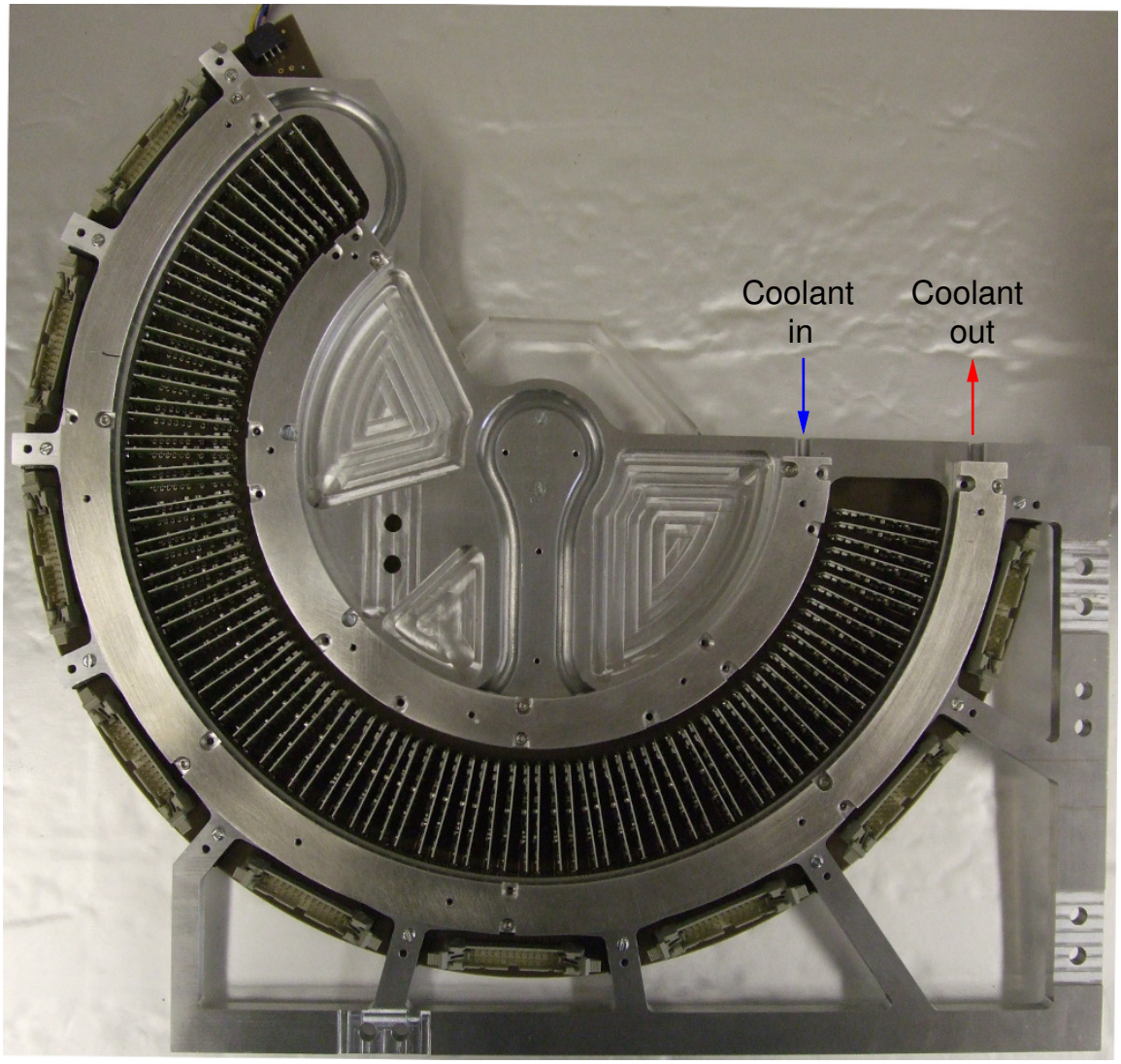

Figure 4.6: Photograph of the detector PCB from the back side, with the preamplifier covers removed. The inlet and outlet of the coolant are indicated by arrows.

The random high frequency noise seen in the oscilloscope screen-shots will be filtered and averaged by the digital data acquisition system. The different amount of noise seen in the two figures is due to the different scales on the oscilloscope.

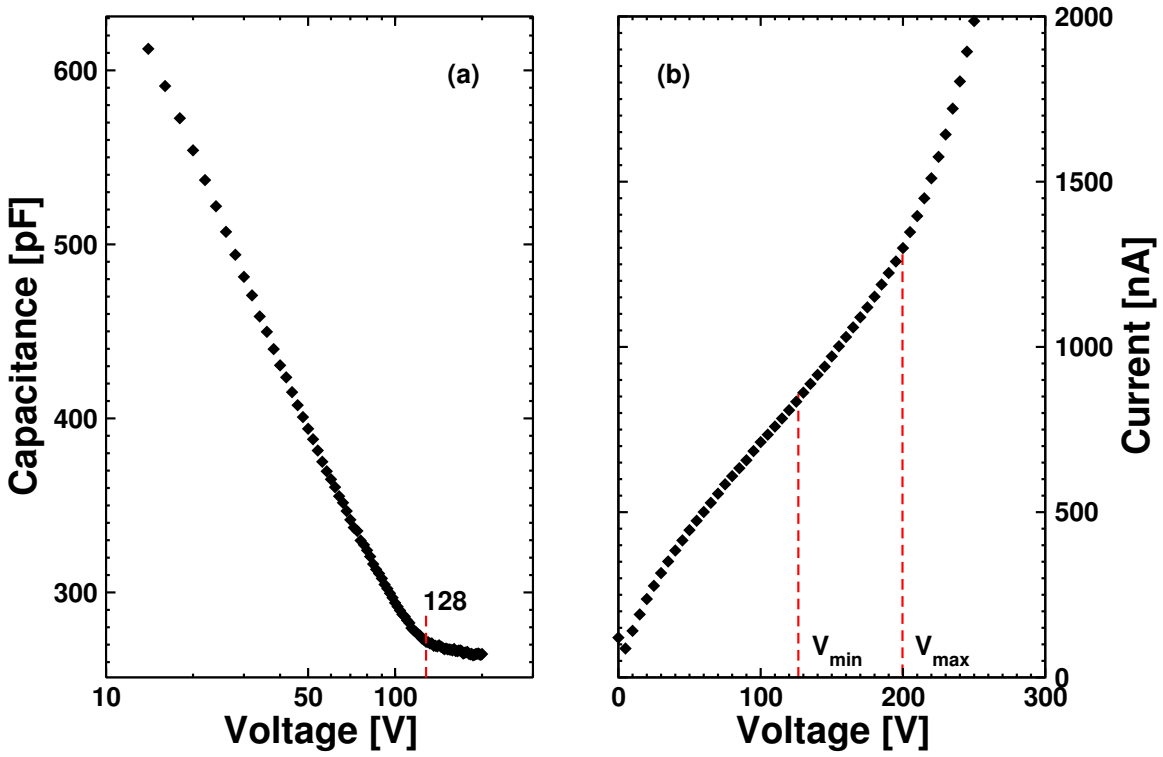

Figure 4.7: (a) Capacitance as a function of bias voltage. The detector is fully depleted when 128 V is applied. (b) Current as a function of voltage. The operational region of the detector lies between the two dotted lines. V_{max} shows the point where the detector becomes resistive.

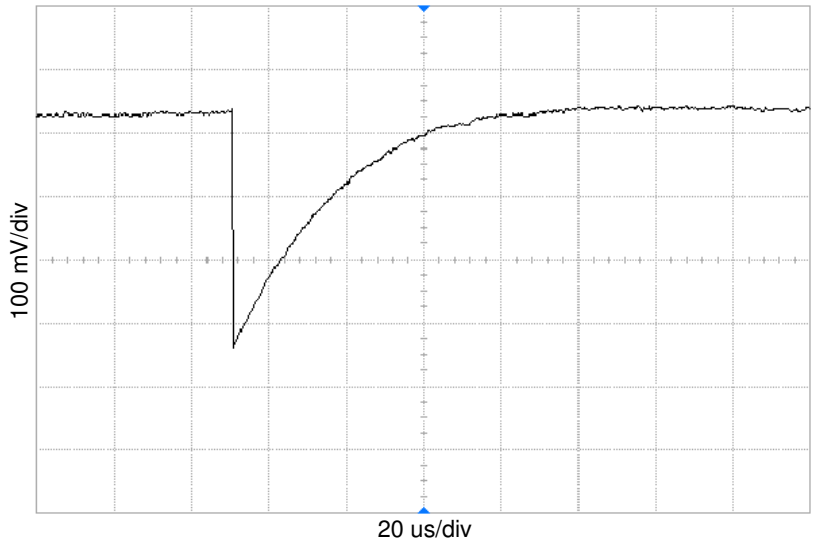

Figure 4.8: Oscilloscope screen-shot from the detector tests with cosmic radiation. A random detector channel was selected (Channel 2) where approximately 1 MeV was deposited.

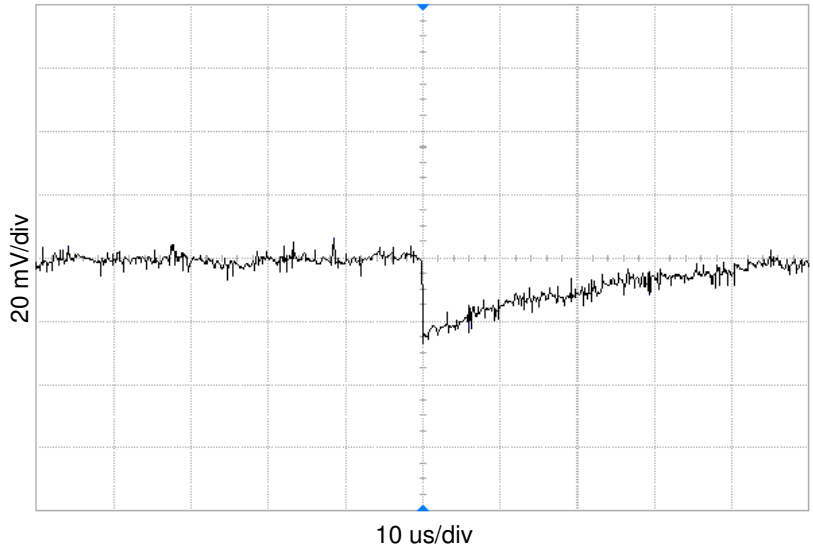

Figure 4.9: Oscilloscope screen-shot from the detector tests with an ^{241}Am source where the 59.54-keV γ-ray was detected. A random detector channel was selected (Channel 2).

4.2 Preamplifiers tested for the silicon detector

In a silicon detector the charge produced by the incident radiation is too small to be used without further amplification [Kn00]. The first amplification stage in the signal chain is made using an FET followed by a preamplifier.

The output of each of the segments of the SAGE silicon detector is connected to a separate preamplifier. Because of the considerable number of channels (90 in total) it is essential the preamplifiers are compact so they can be placed in close proximity to the detector, on the same PCB if practicable. This will reduce the capacitive load on the detector compared to using long cables between the detector and preamplifiers and minimise the effect on signal to noise ratio. SAGE will be mainly employed in the study of low energy electrons, thus high gain preamplifiers need to be used. Additionally the preamplifiers are required to be able to operate in high vacuum.

The preamplifiers that fulfilled the above criteria were the Amptek A250F/NF, the Cremat CR-110 and the CAEN A1422 hybrid preamplifiers, as well as modified versions of the latter two with increased gain. Hybrid preamplifiers, in this case, means preamplifiers made by using printed and discrete electronic components on a ceramic interconnection substrate [Se95]. Technical specifications of these preamplifiers are described in Table 4.2. The physical dimensions of the preamplifiers are shown in Figure 4.10 and photographs of the chips in Figure 4.11.

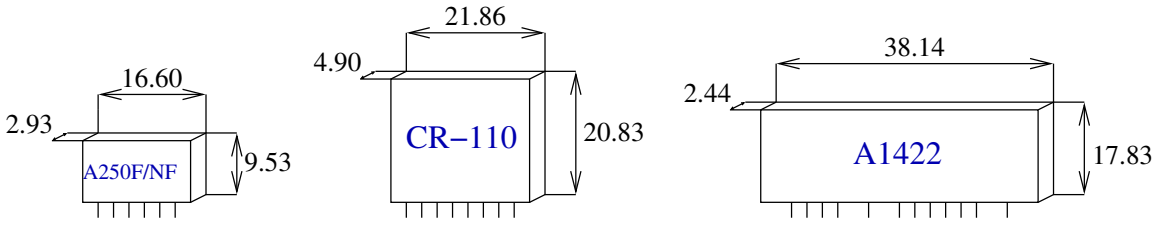

Figure 4.10: Schematic drawing of the tested preamplifiers with their dimensions.

Table 4.2: Specifications table of the tested preamplifiers showing their gain, output and operational characteristics.

	A250F/NF	CR-110(61)	CR-110(200)	A1422(90)	A1422(200)	A1422(400)	A422
Gain [mV/MeV]	175	61	200	90	200	400	90
Noise in Si [keV]	<2	<2	<2	<2	<2	<2	<10
T_{rise} [ns]	3.80	6.55	6.55	12.00	12.00	12.00	<20.00
Decay time constant [μs]	250	140	140	1180	50	50	220
Output impedance [Ω]	100	50	50	50	50	50	50
Operating voltage [V]	±6 - ±8	±6 - ±13	±6 - ±13	±12	±12	±12	±24
Operating current [mA]	±4	+7.5, -3.5	+7.5, -3.5	+15, -8	+15, -8	+15, -8	+20, +30
Power dissipation [mW]	20	70	70	276	276	276	576

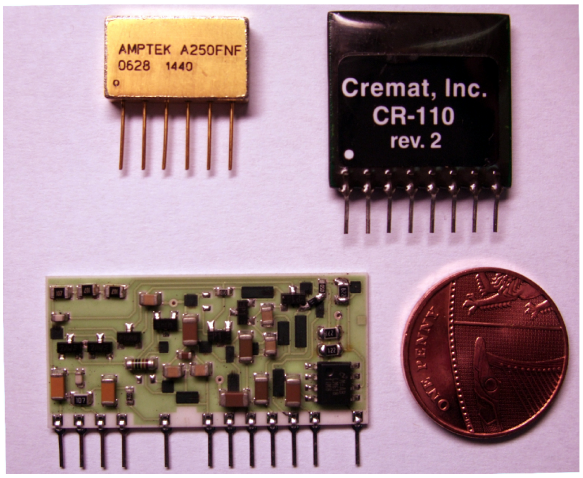

Figure 4.11: Photograph of tested preamplifiers. Clockwise from the top left corner: A250F/NF, CR-110, A1422.

The preamplifiers were tested using both a test pulse from a pulse generator and a detector signal. The main tests were made with a window-less silicon PIN photodiode (HAMAMATSU S3590-06), with active area of 9x9 mm and 25 pF capacitance. The preamplifiers were mounted on test PCBs placed inside a metal box, for shielding from electronic noise and light. A ^{133}Ba source was used for testing the setup with electrons and some additional tests were made with alpha particles using an ^{241}Am source and cosmic rays.

For the tests with the detector the setup was placed inside a vacuum chamber with an ultimate pressure of the order of 10^{-2} mbar and was cooled down to -30° C (temperature at circulator) with a refrigerated circulator using ethanol as the refrigerant (photodiode temperature varied depending on cooling time). The preamplifiers were powered directly from a standard NIM crate with no additional filtering and the PIN diode was biased at +75 V.

The preamplifier output was connected to a spectroscopy amplifier and then to the analog or digital pulse processing electronics. The digital electronics used for the tests were the Lyrtech 16-channel VHS-ADC with Virtex-2 field-programmable gate array (FPGA) (a version of these cards with Virtex-4 FPGA is used with SAGE), the

4-channel Tracking Numerical Treatment (TNT2) card [Ar06] and the Gamma-Ray Tracking 4 channel (GRT4) VME card [La04]. The firmware for the Lyrtech digital electronics was still under development during the test period so the main bulk of the tests were made using a multichannel analyser with the MAESTRO-32 MCA emulation software.

The different preamplifiers tested for SAGE are presented in the following subsections together with the results from the performed tests.

4.2.1 The AMPTEK A250F/NF

The A250F/NF was thoroughly tested as its high gain, small size and low power consumption made it a strong candidate for the preamplifier choice. For the first series of tests the AMPTEK PC250F test board (Figure 4.12) was used. Modifications were made to the detector bias supply and the preamp bias supplies. Low-pass bias filters and power supply decoupling capacitors (reservoir capacitors to provide low impedance for the preamplifier circuit and to filter the power supply) were added to the test board. These can be seen in more detail in the circuit diagram in Figure 4.13.

An in-house version of the AMPTEK test board that can accommodate 4 preamplifiers and uses a surface mount FET (MMBF4416) was used to further test the A250F/NF. The tests showed that the preamplifier is unable to drive a $50\,\Omega$ load over long distances as distortions to the signal occur. This was later verified by the manufacturer by confirming it has an output impedance of $100\,\Omega$.

To overcome this problem buffer amplifiers were used for impedance matching. The quad channel Cadeka CLC4600 and the single channel Texas Instruments OPA820 and OPA842 amplifiers were tested. The buffers proved to have an effect on signal quality. In some cases overshooting or undershooting was observed, in others the exponential character of the signal was lost. Various methods were used to filter the output signal and compensate for the changes produced from the buffer amplifiers.

To take advantage of the full dynamic range of the digital electronics, additional gain and offset adjustment is required, as explained in Section 4.3. A version of the

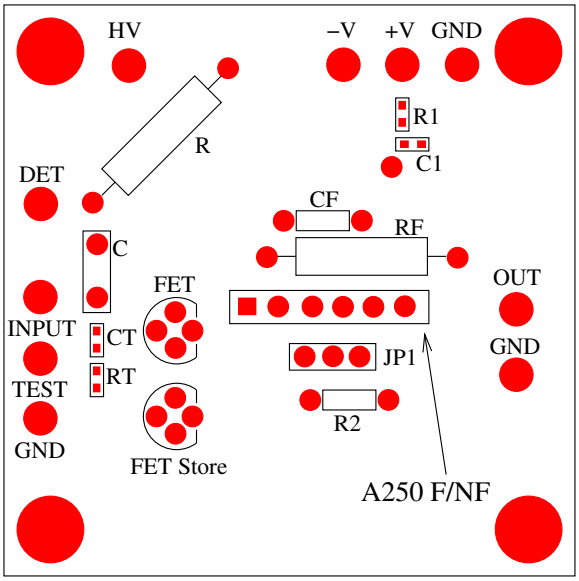

Figure 4.12: The AMPTEK PC250F test board used for testing the A250F/NF preamplifier.

test board that takes these requirements into account and also filters the output was built (see schematic representation in Figure 4.14). This test board has two different gain stages. In the first one a CMOS operational amplifier allows high gain without greatly affecting the signal shape; a buffer amplifier is used in the second stage as a line driver. The offset adjustment is made by changing resistor values, so if this design was to be used in the final SAGE PCB an offset should have been decided beforehand. This test setup produced the best results observed using the A250F/NF. A typical output pulse from this is shown in the oscilloscope screen-shot in Figure 4.15.

The overall performance of the A250F/NF was acceptable but some of the better test results were not reproducible. If this preamplifier was to be used in SAGE, an additional buffering circuit needed to be accommodated on the detector PCB to drive the 50 Ω load on the output of the preamplifiers. This preamplifier uses an external FET (unlike the ones presented next that have integrated FETs) that should also have been integrated in the detector PCB circuit. These would have made the PCB more difficult to manufacture and more prone to reliability issues.

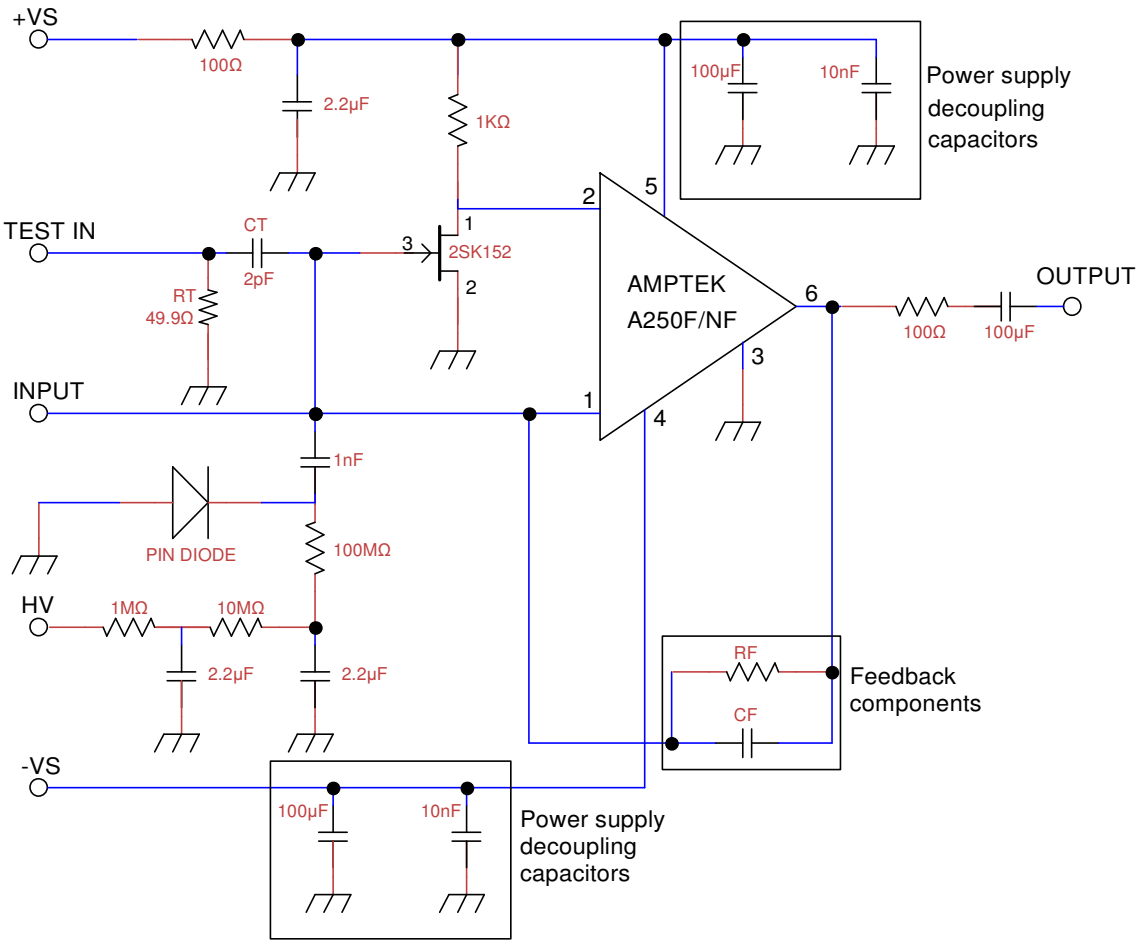

Figure 4.13: Circuit diagram of the modified PC250F test board.

4.2.2 The Cremat CR-110

Cremat provides the CR-150 evaluation board (shown in Figure 4.16) for testing this preamplifier. The tests with the Cremat preamplifier proved to be more straightforward than those described earlier for the A250F/NF. The CR-110 has a 50 Ω output impedance and so it can drive a 50 Ω load over long distances. No modifications were made to the CR-150 test board, as from the circuit diagram one can see that both the bias and the preamplifier power supplies are very well filtered.

The CR-110 performed consistently better than the A250F/NF. Non-exponential behaviour (similar to the one observed for the A250F/NF) was present in some cases

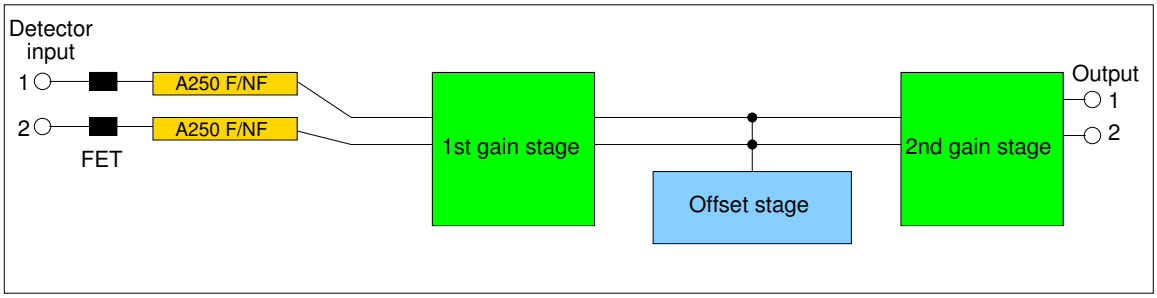

Figure 4.14: Schematic representation of the test PCB for the A250F/NF preamplifier where the different gain and offset stages can be seen.

in the output pulses of a CR-110 preamplifier. The oscilloscope screen-shot from Figure 4.17 is an example of such a pulse. These pulses are not desirable but were often seen with the CR-110 and A250F/NF.

4.2.3 The CAEN A422 and A1422

The first preamplifier received from CAEN was the A422 hybrid charge-sensitive preamplifier with a fast timing output. This preamplifier has adjustable gain of 1 mV/MeV, 45 mV/MeV and 90 mV/MeV and requires ±12 V and ±24 V to operate. The performance of the preamplifier was very poor and it was also found to overheat. This was attributed to two Zener diodes that were used as voltage regulators to provide the ±12 V from the ±24 V inputs (see Figure 4.18). The Zener diodes were removed and the ±12 V were externally supplied to the preamplifier, ultimately reducing the produced heat. The performance of this preamplifier was found to be insufficient showing two components in the rise time and very poor resolution.

To solve the problems of the A422, CAEN provided the A1422 hybrid charge-sensitive preamplifier. This preamplifier was smaller in size than the A422 and had a fixed gain of 90 mV/MeV. Its decay time constant was more than five times that of the A422 (1180 μs compared to 220 μs). The PCB shown in Figure 4.19 was specifically built to test this preamplifier which performed very well. Simple filtering was applied at the preamplifier power supplies, and no filtering used for the detector

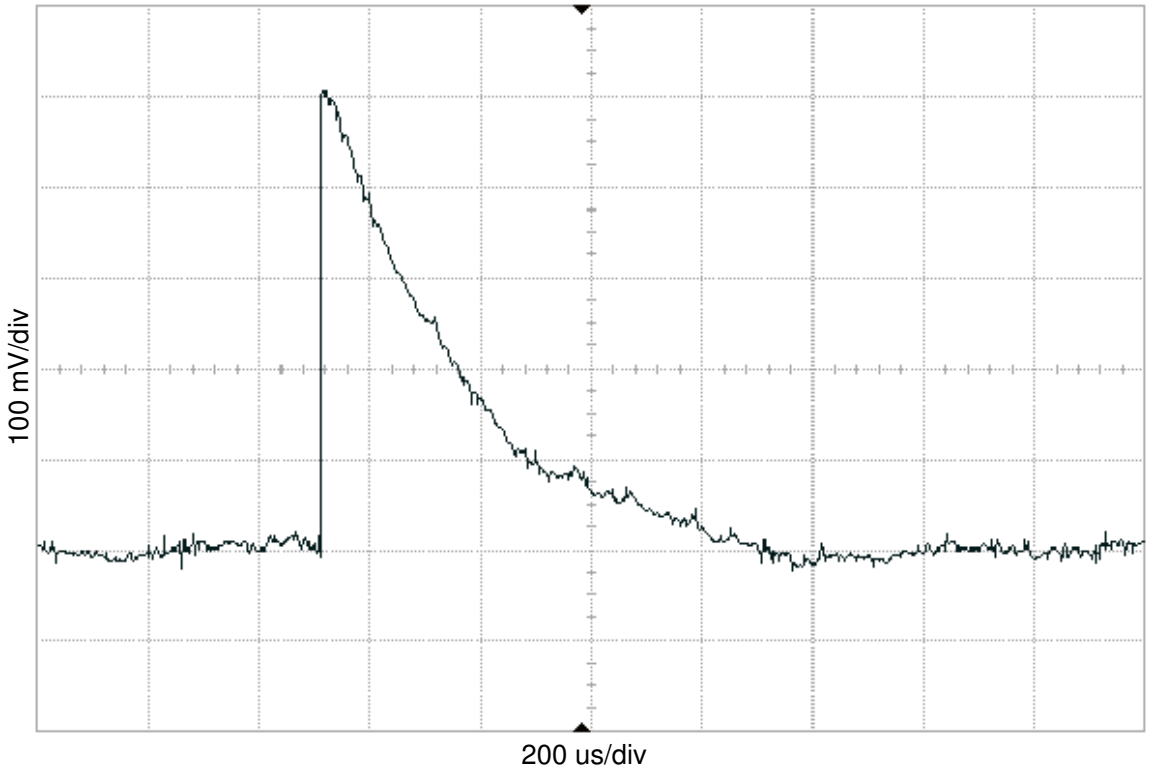

Figure 4.15: Oscilloscope screen-shot from the A250F/NF preamplifier using the test PCB from Figure 4.14. The setup was in atmospheric conditions and double screened within two metal boxes. The pulse is from cosmic radiation.

bias, as the photodiode was powered through the preamplifier that has an on-board bias filtering circuit. This product was still under development from CAEN thus additional modifications were requested. The decay time constant was reduced to 50 μs (to avoid pileup events at high rates) and the gain was increased to 200 mV/MeV for two test units and 400 mV/MeV for two others. All the tested A1422 units have 200 pf input capacitance.

The performance of the higher gain version was very good, making it a strong candidate over the A250F/NF and the CR-110. A typical example of a pulse from the output of an A1422 preamplifier is shown in Figure 4.20, where the very good signal quality is evident. The major issue with this device is its size, but from a detailed

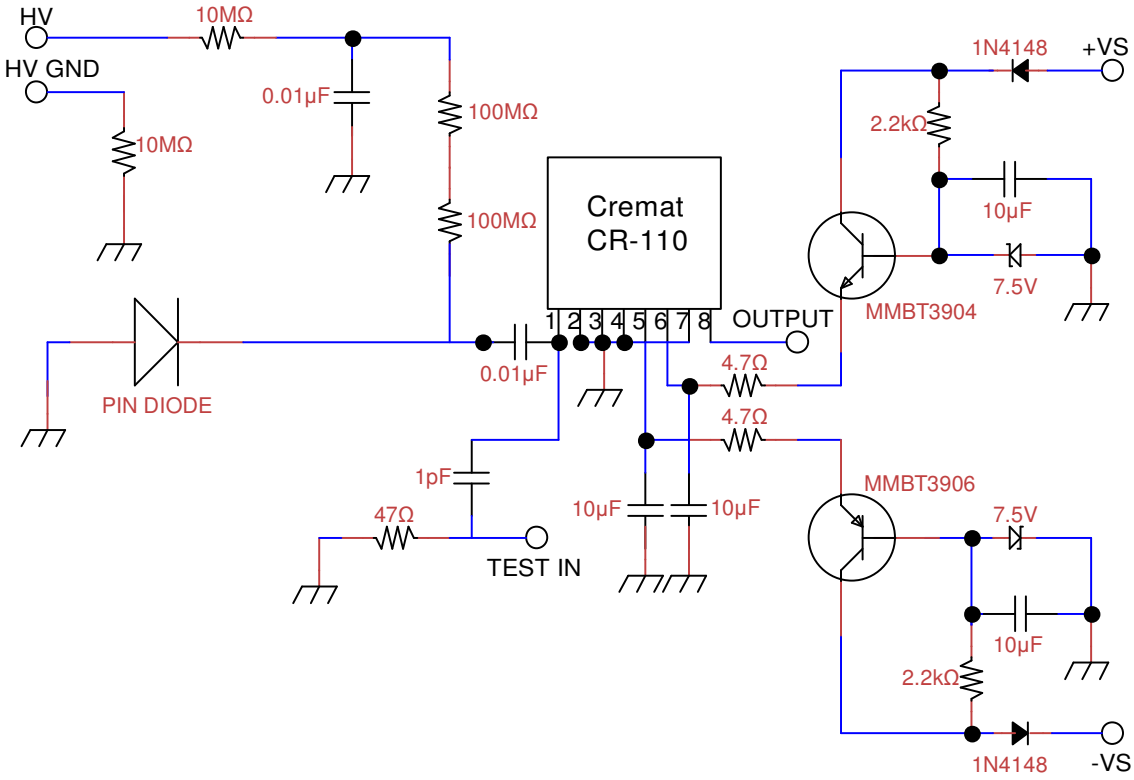

Figure 4.16: The CR-150 evaluation board used for testing the CR-110 preamplifier.

study it was found that 90 of these preamplifiers could be accommodated on the SAGE PCB. Their power dissipation is also higher than the other tested preamplifiers but this is unlikely to be an issue as they will be sufficiently cooled.

A summary of the results from the preamplifier tests can be seen in Tables 4.3 and 4.4. The first table shows the test results using an open ^{133}Ba source and the second the outcome of the ^{241}Am tests that were made to see how the preamplifiers perform at the low energy range.

From these results one can observe that the A1422 is consistently better than the CR-110 and A250F/NF. In fact the A250F/NF showed the poorest performance. The results also show that the TNT2 cards worked better than the Lyrtech, but this is not unexpected as the development of the TNT2 cards was almost complete at the time of the tests whereas the Lyrtech firmware was still under development, the

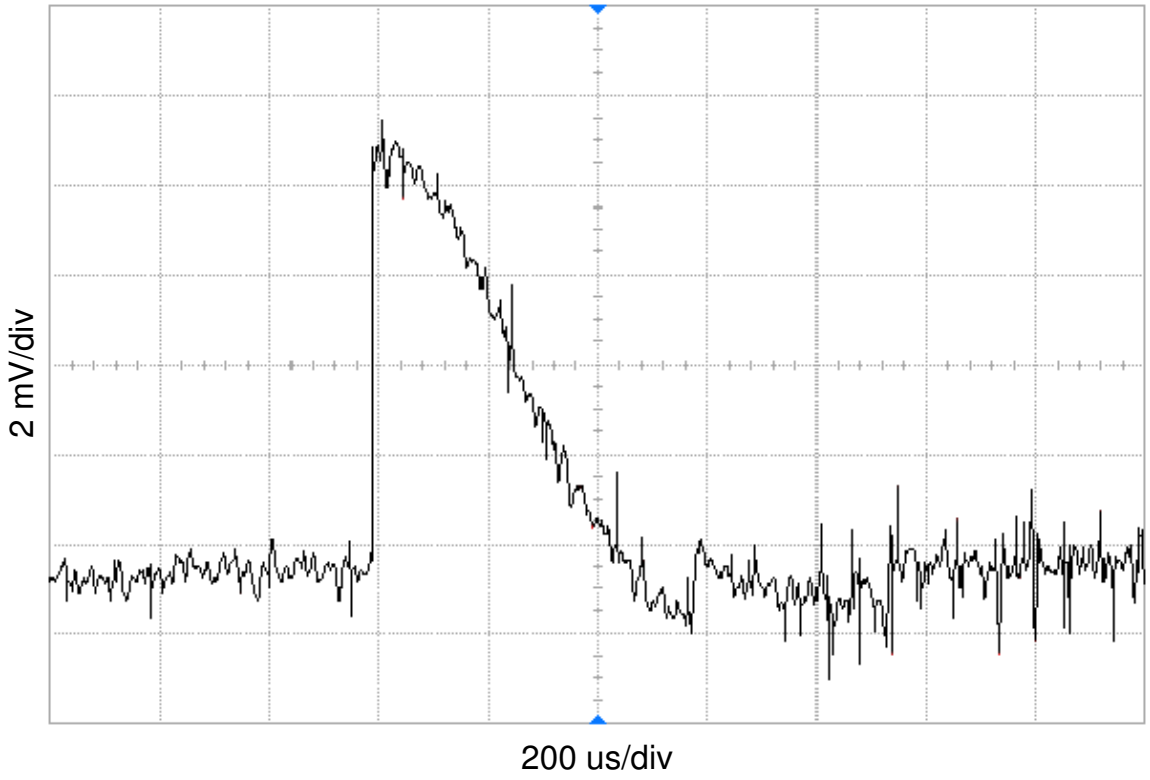

Figure 4.17: An oscilloscope screen-shot from the CR-110(61) preamplifier using the ^{133}Ba source. The setup was cooled at -30° C, in vacuum and double screened within two metal boxes. The signal shows non-exponential behaviour.

main outstanding issue being the non finalised constant fraction discriminator (CFD) algorithm. The A1422 is also the only one of the three preamplifiers that gave good results with the Lyrtech in its unfinished state. After consideration of all the above mentioned factors the CAEN A1422 with gain 400 mV/MeV and decay time constant of 50 μs was chosen as the preamplifier to be used with the silicon detector of SAGE.

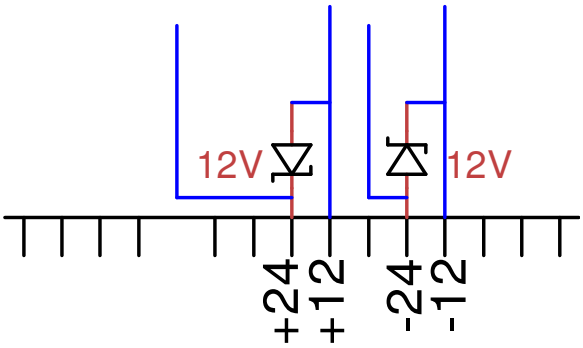

Figure 4.18: The Zener voltage regulator diodes, mounted on the A422 preamplifier, used to provide ±12 V from the ±24 V inputs.

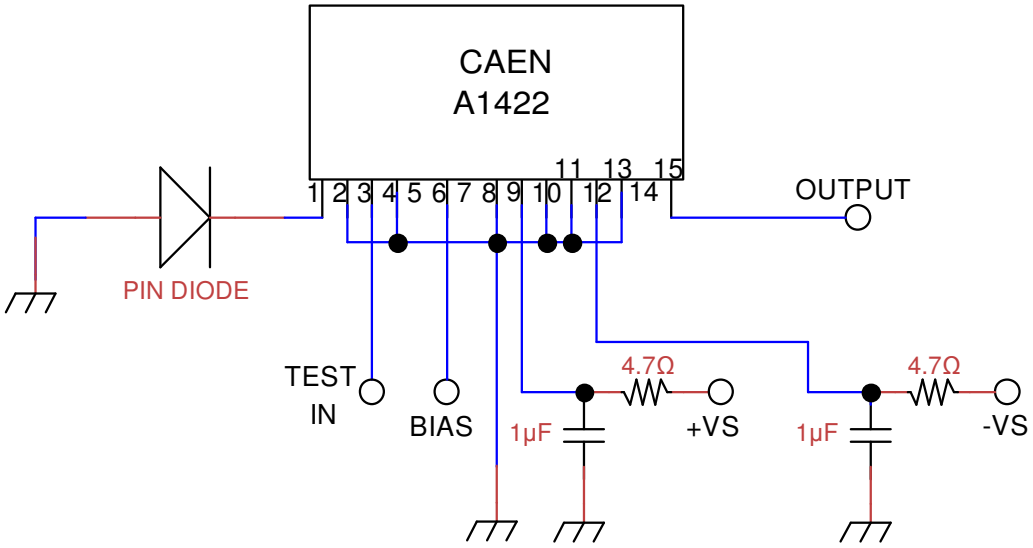

Figure 4.19: Circuit diagram of the test board built for testing the A1422 preamplifier.

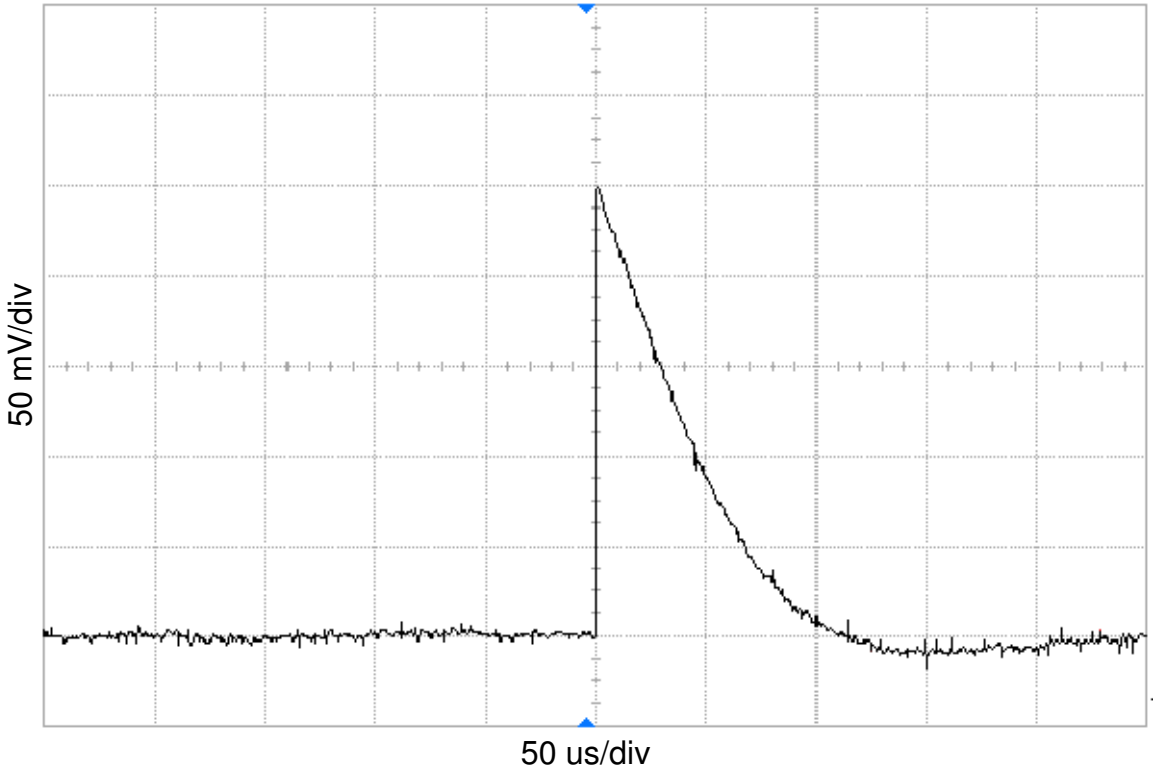

Figure 4.20: The output from an A1422(400) preamplifier on the oscilloscope, taken using cosmic radiation. The setup was in atmospheric conditions and double screened within two metal boxes.

Table 4.3: Preamplifier test results using analogue and digital electronics with a ^{133}Ba source. The full width at half maximum (FWHM) for the 320.03 keV electron peak is shown for each case.

Preamplifier	A250F/NF	CR-110(61)	A1422[a]
Analogue [keV]	4.84	4.41	4.17
TNT2 [keV]	4.97	4.53	4.67
Lyrtech [keV]	7.93	7.16	5.44

[a]TNT2 results taken with the 90 mV/MeV version and Lyrtech with the 400 mV/MeV.

Table 4.4: Preamplifier test results using analogue and digital electronics with an ^{241}Am source. The FWHM for the 59.54-keV γ-ray peak is shown for each case.

Preamplifier	A250F/NF	CR-110(61)	A1422(400)
Analogue [keV]	3.20	2.85	2.61
Lyrtech [keV]	7.73	Not available[a]	3.03

[a]The internal trigger of the Lyrtech VHS-ADC was not finalised at the time of these tests and the software could not trigger correctly making the measurements with this low gain preamplifier impossible at low energies.

4.3 Gain and offset Cards

To be able to use the full dynamic range of ±1.1 V of the Lyrtech VHS-ADC, gain and offset adjustments are needed for both the silicon and germanium signals. Different options were investigated and it was decided that a Gain and Offset card (GO-card) should be used.

The two different GO-cards tested were the SmartPET GO-card (SGO-card) and the Liverpool GO-card (LGO-card). These cards were tested with signals from germanium and silicon detectors and a pulse generator.

The SGO-card is a NIM module developed and built by the Rutherford Appleton Laboratory (RAL). It is remotely controlled via Ethernet using a control interface implemented in the Multi Instance Data Acquisition System (MIDAS) [Pu]. Each module consists of 32 individually controlled channels, but the option of reducing them to 16 per card exists, in order to suppress electronic noise.

The SGO-card is a non-inverting unit that allows the buffering of detector signal, the removal of input offset, and the adjustment of gain and offset on the output signal. From the two offset level adjustments, one precedes (input bias) and one follows (output offset) the gain stage and a combination of the two allows very precise offset adjustment. The card has an input impedance of 50 Ω, thus if a preamplifier signal is to be directly connected to it, the preamplifier needs to have 50 Ω output impedance. The bandwidth of the SGO-card is independent of gain and limited to about 26 MHz.

A gain calibration of this card was performed using a 60 mVpp tail pulse, with 200 ns rise time and 1 ms fall time. The outcome of the calibration shown in Figure 4.21 indicates the mainly logarithmic character of the gain stage. Hexadecimal values are used on the gain axis as the SGO-card control interface requires input in hexadecimal values.

The LGO-card (a prototype unit at the time of the tests mentioned here) is designed by the University of Liverpool. It consists of a mother board, accommodating the connector sockets, and daughter boards with the gain and offset circuits. It is

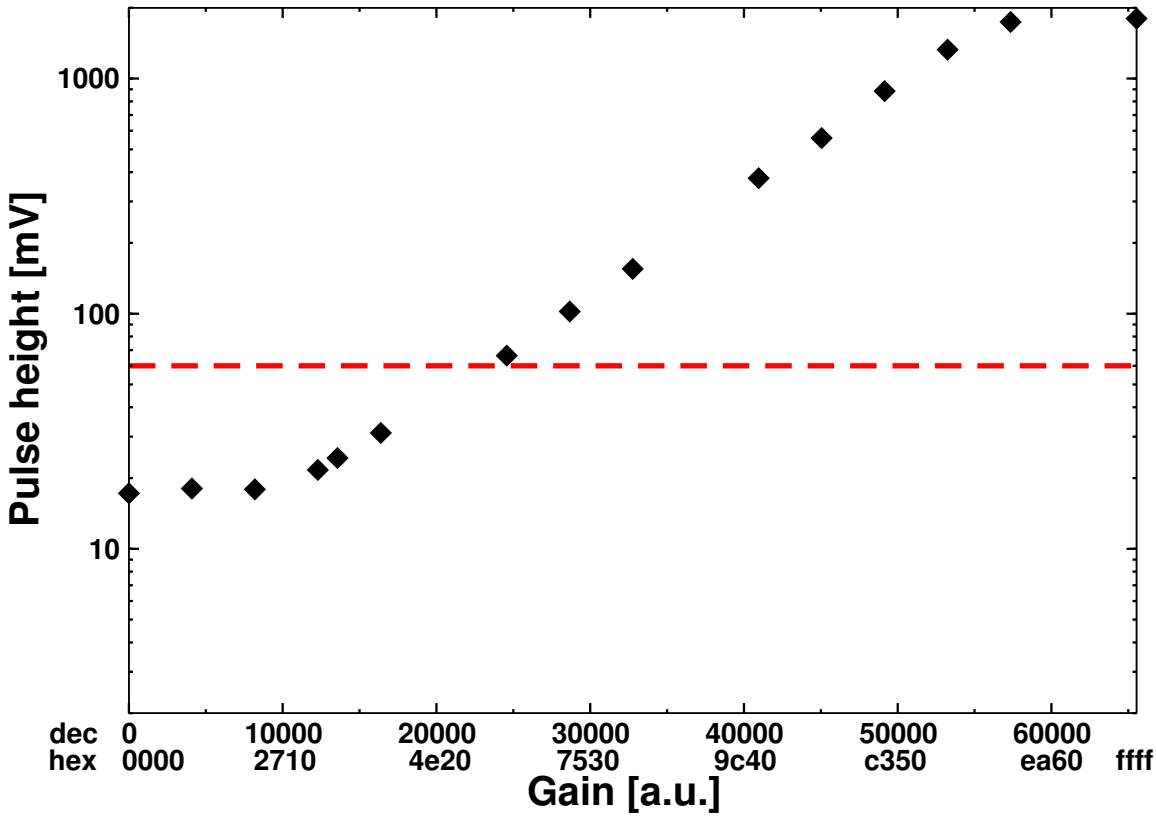

Figure 4.21: Gain calibration of SGO-card using 60 mVpp tail pulse, indicated by the red dashed line. Both decimal and hexadecimal values are shown on the gain axis.

an inverting unit with all the channels having fixed gain but adjustable offset via a potentiometer. The gain of each channel can be modified by changing the gain adjustment components, or alternatively daughter boards with different gains can be built, a more preferable option. The input impedance of the card is 1 kΩ allowing the direct connection of signals from sources that are unable to drive 50 Ω loads e.g. the A250F/NF preamplifier. The bandwidth of the LGO-card is not dependent on gain over the gain ranges of interest and is limited to about 20 MHz.

The finalised version consists of two different types of motherboards. One with SMA connectors, for the silicon detector, that can accommodate three 4-channel daughter boards, and one with MMCX (micro-miniature coaxial) connectors, for the

germanium detectors, in which four 4-channel daughter boards can be connected. Up to four mother boards (48 channels in the SMA version and 64 channels in the MMCX one) can be placed in an individual, purpose-built box containing all the electronics needed (including power supplies), thus a NIM crate is not required.

Both the GO-cards were thoroughly tested mainly using a p-type germanium detector with a ^{133}Ba source. The main ^{133}Ba γ-ray energies are 53.2 keV, 79.6 keV, 81.0 keV, 160.6 keV, 223.2 keV, 276.3 keV, 302.8 keV, 356.0 keV and 383.8 keV [Tr90]. The detector signal was fed through the GO-card to a spec-amp and then to an MCA. Analogue electronics were used in most of the cases as the Lyrtech digital electronics were still under development. The gain on the spec-amp was adjusted so that the 356.01 keV γ ray of ^{133}Ba was always at channel 7000 on the MCA. FWHM values were measured for the 53.16 keV and 356.01 keV γ rays.

The next set of tests was made using a tail pulse, obtained from a pulse generator. The tail pulse amplitude was adjusted so that in each case the resulting peak on the MCA was positioned at approximately the same position as the 53.16 keV and the 356.01 keV peaks from the germanium tests using the same spec-amp settings. This ensured that the MCA and the spec-amp settings did not affect the test results.

To check how the resolution depends on the gain, the offset of the buffer cards was set to 0 V. For the SGO-card both the offset settings were adjusted to setpoint 0x8000 (the middle of the range) which gave the required 0 V offset. The gain was adjusted using a tail pulse and comparing the output with that of the relevant LGO-card channel. The cards were considered to have the same gain when their output pulses had the same amplitude when measured on the oscilloscope. To make the two cards directly comparable the input signal of the LGO-card was 50 Ω terminated, but measurements were also made using 1 kΩ input impedance. A reference measurement was made without using a GO-card, i.e. the germanium detector or the pulse generator signals were directly connected to the spec-amp. The input of the spec-amp was 50 Ω terminated, to match the input impedance of the Lyrtech system.

A summary of the results of the tests is shown in Tables 4.5 and 4.6 and Fig-

ures 4.22 and 4.23. The LGO-card performs better than the SGO-card independent of energy, throughout the examined gain range. In Figure 4.24 a comparison of the 356.01 keV γ ray from the reference measurement and the SGO-card x8, LGO-card x8 50 Ω and 1 kΩ measurements is made.

It should be noted that for the same gain on the LGO-card with 50 Ω input impedance the input signal is attenuated to approximately half of that with 1 kΩ impedance. To compensate for this the gain on the spec-amp was increased, introducing additional noise in the system. This makes the LGO-card x1 1 kΩ measurement directly comparable with the LGO-card x2 50 Ω rather than the LGO-card x1 50 Ω and so on.

It was also investigated whether for a set gain the resolution achieved is offset dependent. Both GO-cards were tested at gain factors of 1 and 8 (LGO-card 1 kΩ input impedance). The germanium detector with a ^{133}Ba source was used and the FWHM for the 356.01 keV γ ray was measured. The gain settings on the spec-amp were kept constant for each module.

For the LGO-card it was found that the FWHM is constant within 2% for the x1 gain and 3.5% for x8 gain throughout the offset range. For the SGO-card it varied up to 20% for both gains. Both GO-cards have an offset range of $\pm$2 V for gain greater than x1. When the SGO-card is studied in the attenuation region the offset range reduces gradually down to $\pm$1 V. If the LGO-card is used as an attenuator then the offset range can be kept at $\pm$2 V if required.

It should be noted that the two offset stages of the SGO-card cannot be individually monitored. A combination of the two stages gives the desired offset in each case, hence the same offset can be achieved using different settings. To further investigate this, more thorough testing was made by using the SGO-card at x4 gain and setting the offset at -800 mV using different offset settings.

The output signal of the SGO-card was fed to a spec-amp adjusted so that the 356.01 keV γ ray was positioned at channel 7000 of the MCA; when both SGO-card offset settings were adjusted at the centre of their range (0x8000). From Table 4.7

Table 4.5: Performance of the GO-cards for a 53.16 keV γ ray compared to a reference measurement in which no GO-card was used. Due to the good peak-to-background ratio the error on the FWHM calculation is not greater than 5% in any case.

GO-card	Germanium detector		Pulse generator	
	FWHM [keV]	FWHM [ch]	$\approx$ FWHM [keV]	FWHM [ch]
Reference	0.73	14.30	2.23	43.39
SGO-card x1	3.28	64.51	3.38	67.32
LGO-card x1 50 Ω	1.39	27.33	3.57	70.36
LGO-card x1 1 kΩ	0.76	14.92	1.10	21.73
SGO-card x2	2.20	43.28	2.63	51.95
LGO-card x2 50 Ω	0.91	17.80	1.36	26.89
LGO-card x2 1 kΩ	0.68	13.33	0.43	8.56
SGO-card x4	2.06	40.56	2.37	46.94
LGO-card x4 50 Ω	0.92	18.17	0.74	14.77
LGO-card x4 1 kΩ	0.71	13.99	0.95	18.98
SGO-card x8	2.33	45.79	2.45	48.39
LGO-card x8 50 Ω	0.65	12.77	0.62	12.35
LGO-card x8 1 kΩ	0.70	13.72	0.59	11.57

can be seen that the resolution varies a lot with the offset. The output offset seems to introduce most of the noise. A higher offset level, obtained by keeping the output offset at 0x8000 and increasing the input bias, gave a FWHM of around 2.6 keV in all cases.

Noise is introduced to the system when the offset levels are set further away from the middle of the range. To avoid this and to try to make the overall performance of the SGO-card better, filtering capacitors can be implemented at both offset stages.

To test how the GO-cards work with digital electronics an additional test was

Table 4.6: Performance of the GO-cards for a 356.01 keV γ ray compared to a reference measurement taken without a GO-card. Due to the good peak-to-background ratio the error on the FWHM calculation is not greater than 5% in any case.

GO-card	Germanium detector		Pulse generator	
	FWHM [keV]	FWHM [ch]	$\approx$ FWHM [keV]	FWHM [ch]
Reference	1.03	20.18	2.18	42.95
SGO-card x1	3.59	70.60	3.33	65.08
LGO-card x1 50 Ω	1.57	30.84	3.99	78.37
LGO-card x1 1 kΩ	1.06	20.80	1.01	19.93
SGO-card x2	2.82	55.56	2.71	53.25
LGO-card x2 50 Ω	1.16	22.79	1.38	27.24
LGO-card x2 1 kΩ	1.01	19.90	0.45	8.95
SGO-card x4	2.67	52.60	2.41	47.47
LGO-card x4 50 Ω	1.15	22.69	0.77	15.11
LGO-card x4 1 kΩ	1.02	20.00	0.52	10.18
SGO-card x8	2.50	49.14	2.43	47.70
LGO-card x8 50 Ω	0.99	19.51	0.64	12.67
LGO-card x8 1 kΩ	1.00	19.69	0.60	11.74

made with a germanium detector and ^{60}Co source (observing the 1332 keV γ-ray) using the LGO-card at x8 gain. The results from this test are shown in Table 4.8. The measurements made with the LGO-card at x8 gain where consistently better than the reference measurements.

Another issue of importance is whether the pulse characteristics change because of the GO-cards. This was tested mainly using square or tail pulses from a pulse generator and also with a germanium detector. The results of this study are presented in Table 4.9. The fast fall time of a square pulse is affected by both the GO-cards

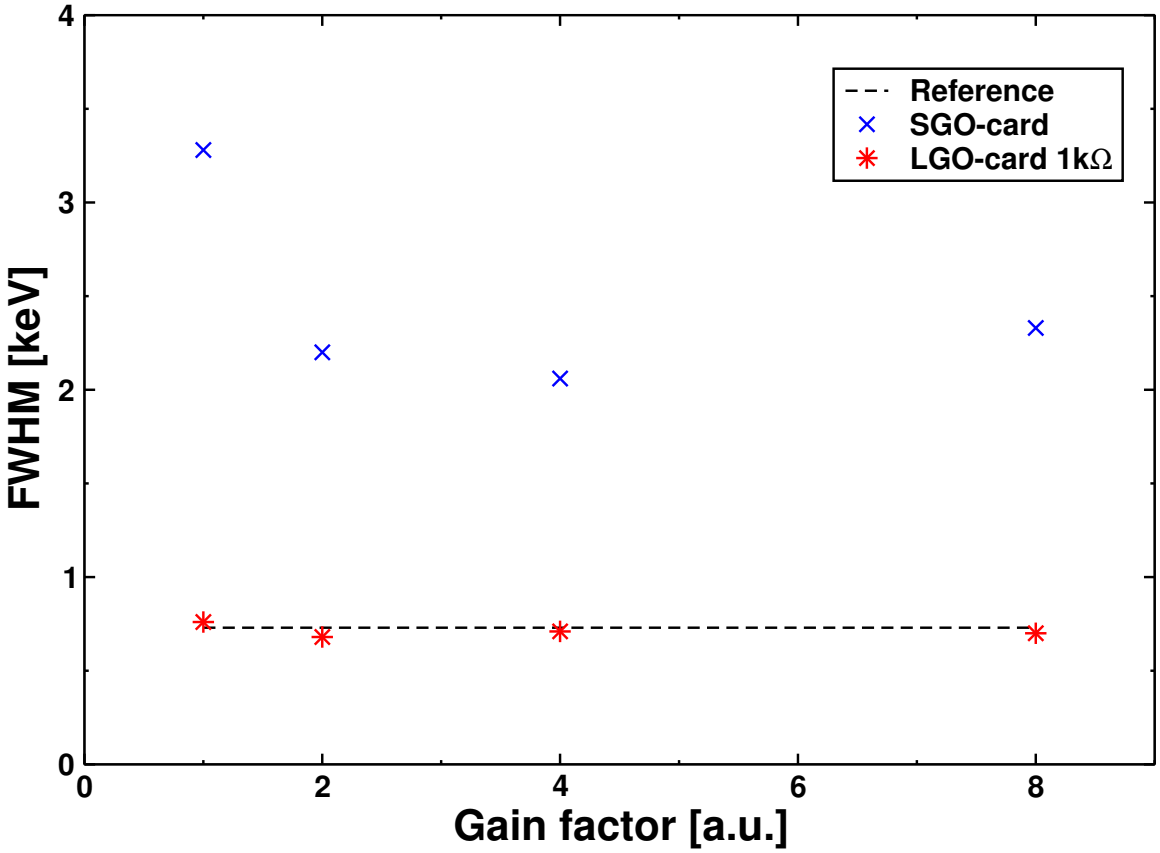

Figure 4.22: The FWHM of the 53.16 keV γ ray for the measurements employing the different GO-cards with a germanium detector. The LGO-card outperforms the SGO-card throughout the examined gain range and performs equally well or even better than the reference. The errors are smaller than the data points in most cases so they were not included in the graph.

but the longer fall times of tail pulses remain mainly unaffected. The rise times of the output signals increase slightly more for the LGO-card than for the SGO-card.

Precise rise times were measured with the square pulse. The rise times of the germanium detector are approximations because the signal quality was not optimum due to signal reflections.

The overall results of the tests showed that the LGO-card outperforms the SGO-card throughout the gain range over which they were tested, so it was selected to be

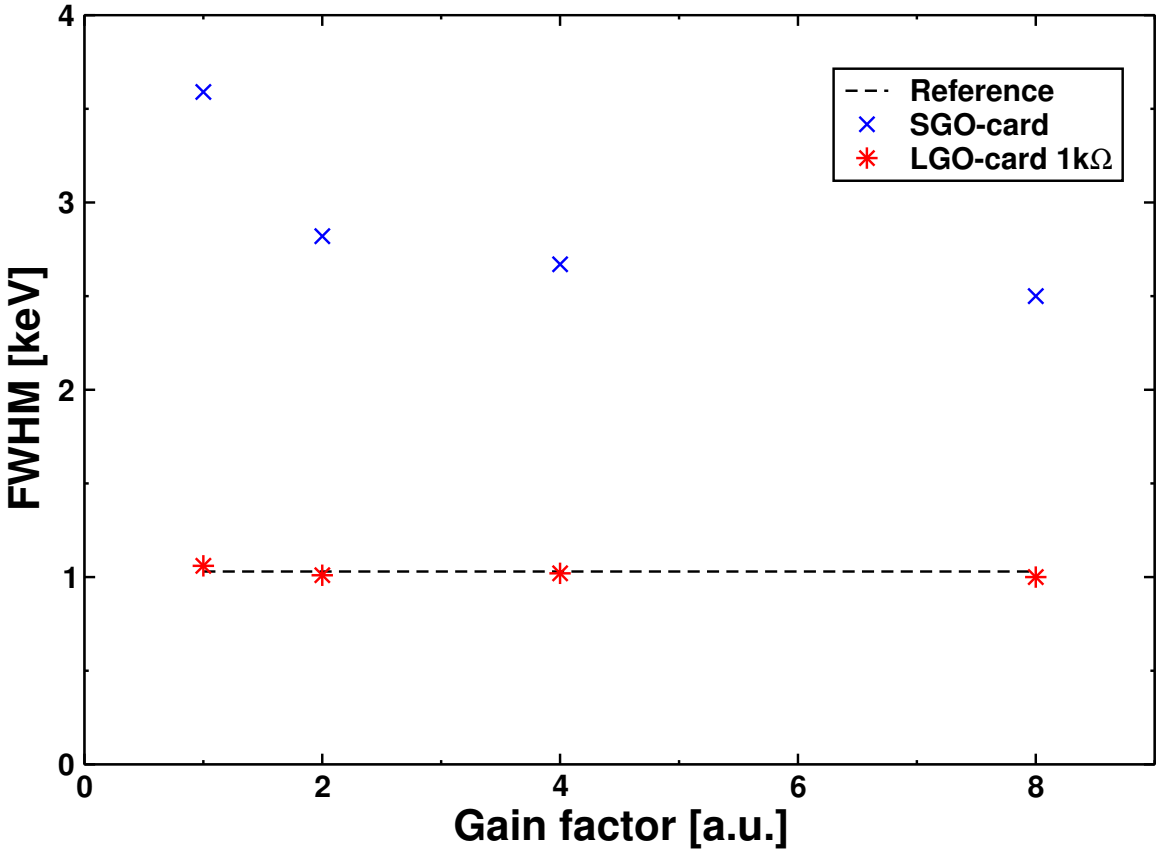

Figure 4.23: Comparison of the FWHM of the 356.01 keV γ ray for the measurements employing a germanium detector with different GO-cards. The LGO-card outperforms the SGO-card throughout the examined gain range is equally good as the reference. The errors are smaller than the data points in most cases so they were not included in the graph.

used in SAGE. For that purpose an adequate number of GO-boxes was build that can fully accommodate all the silicon and germanium channels of SAGE. Because these cards perform so well other groups will also use them for gain and offset adjustments or signal buffering.

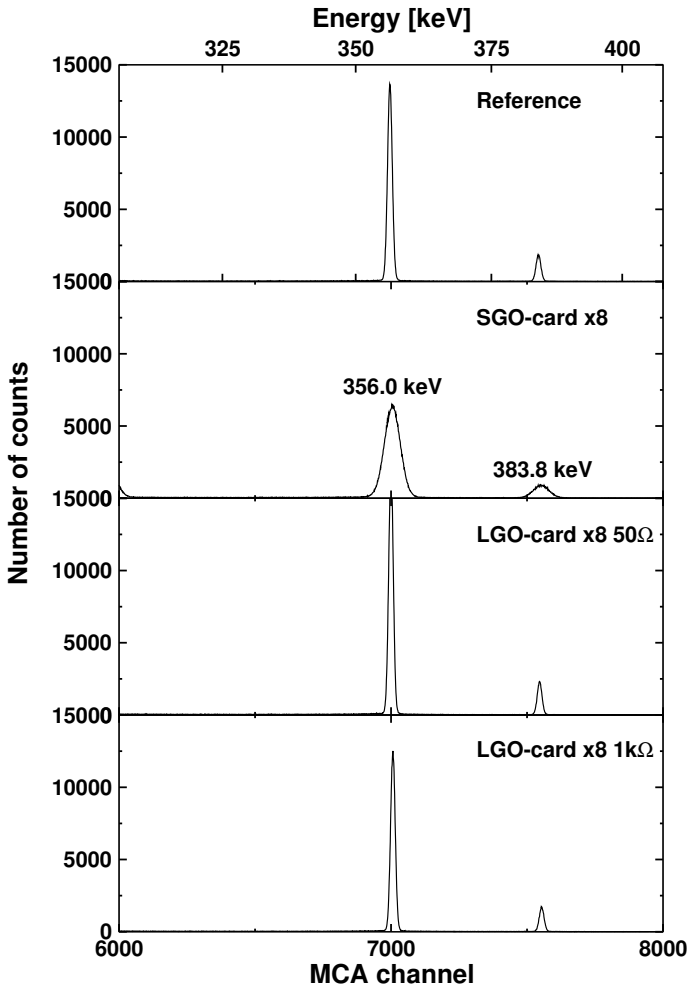

Figure 4.24: A comparison of the 356.01 keV γ ray from the reference measurement and the SGO-card x8, LGO-card x8 50 Ω and 1 kΩ measurements.

Table 4.7: Resolution with respect to offset settings for the SGO-card.

Input bias	Output offset	Peak position	FWHM	
0x	0x	[ch]	FWHM [keV]	FWHM [ch]
9d00	0000	6946.39	3.39	66.20
8fff	8000	6984.97	2.65	51.97
8d00	a000	6990.82	3.42	67.06
8500	f000	6999.43	3.33	65.44
8390	ffff	7000.05	3.08	60.56

Table 4.8: Results from tests using the Lyrtech VHS-ADC in combination with the LGO-card x8 and a ^{60}Co source.

Setup	ADC	Energy [keV]	FWHM [keV]
Ge	Lyrtech	1332	3.82
Ge + LGO-card x8	Lyrtech	1332	2.43
Ge	MCA	1332	2.29
Ge + LGO-card x8	MCA	1332	2.20

Table 4.9: Effect of GO-card on pulse characteristics. A comparison is made with different types of pulses studied either straight from the source or through one of the GO-cards. The tabulated values for the pulse generator signals are accurate within 1%.

	t_{rise}	t_{fall}		t_{rise}	t_{fall}		t_{rise}	t_{fall}
Square pulse			Tail pulse			Germanium detector signal		
Directly from the pulse generator	4.73 ns	4.59 ns	Directly from the pulse generator	201.7 ns	358.0 μs	Directly from the Ge	300.0±50 ns	130.0±10 μs
Through the SGO-card x4	12.47 ns	12.17 ns	Through the SGO-card x8	202.4 ns	368.0 μs	Through the SGO-card x8	330.0±50 ns	150.0±10 μs
Through the LGO-card x4	17.20 ns	17.10 ns	Through the LGO-card x8	203.7 ns	351.0 μs	Through the LGO-card x8	350.0±50 ns	120.0±10 μs

4.4 Signal chain

In SAGE there are 196 outputs from individual detectors/detector segments, 90 from the silicon and 106 from the germanium detectors. All of these channels are connected to a digital data acquisition system employing the Lyrtech 16-channel VHS-ADC cards.

The signal chain from the preamplifier output of the detectors to the Lyrtech VHS-ADC is shown in Figure 4.25. In this figure output for the germanium detectors is considered to be the preamplifier output and for the silicon detectors the output of the D-type to SMA adaptor boxes on the detector chamber.

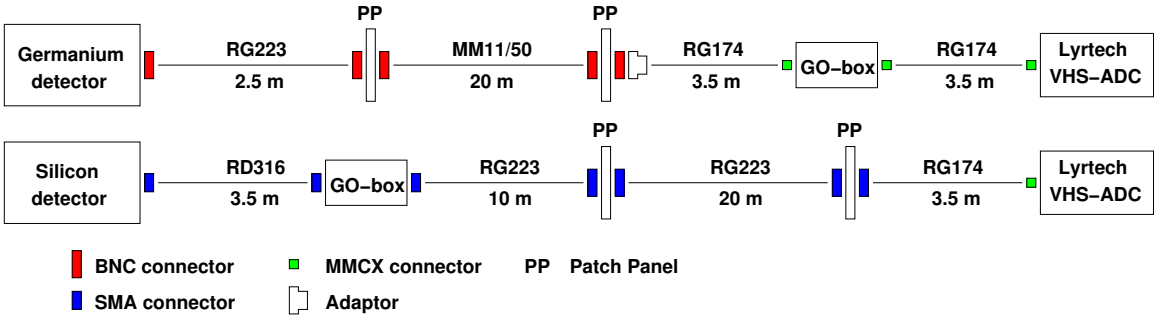

Figure 4.25: Schematic diagram of the signal chain from the output of the detectors to the input of the Lyrtech VHS-ADCs.

The germanium detectors have BNC outputs that are connected to a patch panel on the JUROGAM II support frame using short double-screened RG223 cables. Other connections, like bias shutdown, bias voltage and temperature monitoring are made through the same patch panel.

From this patch panel longer super-screened MM11/50 cables take the signals to a second patch panel inside the air-conditioned electronics cabinets. The GO-boxes for the germanium detectors are positioned inside these cabinets and the connection from the last patch panel to them is made through short single-screened RG174 cables. The same type of cables is used to connect the output of the GO-boxes to the input of the Lyrtech VHS-ADCs.

From the silicon detector's preamplifier outputs the signal is taken to the feed-through flange using 26-way ribbon cables (one of the 26 cables from each ribbon cable is not used). The 25-way D-type connectors on the flange are converted to SMA connectors through the use of custom made adaptor boxes. The SMA outputs are connected to the GO-boxes through short double-screened RD316 cables, meaning the GO-boxes are not located inside the electronics cabinets. Longer cables could be used but this would mean that the preamplifiers might be affected by the 50 Ω impedance of the long cable at their output. Their performance is not influenced by the 1 kΩ input impedance of the GO-cards. The longer cable would require more output current to charge up its greater capacitance than a shorter one, putting a higher load on the output of the preamplifier. This would cause increased heating and affect performance and stability as some amplifiers do not perform well with large capacitive loads on their output. For these reasons the GO-boxes are preferred for driving the longer line.

From the GO-boxes, RG223 cables take the signal to a patch panel inside the electronics cabinets. Short RG174 cables connect the patch panel to the Lyrtech VHS-ADC.

Table 4.10 lists the technical specifications of the cables used in the signal chain. The block diagram in Figure 4.26 shows the structure of the data acquisition system after the signals enter the Lyrtech VHS-ADCs.

The triggerless Total Data Readout (TDR) method [La01] is used in SAGE. In this system no hardware trigger is applied to start the data collection but all the channels run independently and are associated in software to reconstruct the events. This virtually eliminates the dead time issues arising when a common hardware trigger is used and when wide time gates are applied at the focal plane electronics.

Sixteen detector signals can be connected to each Lyrtech VHS-ADC. All the signals are timestamped using a universal clock produced by a Metronome (not shown in the figure) connected to the total data readout interface card (TDRi card) and are tagged with an address to identify which ADC channel they originate from and thus

Table 4.10: Technical specifications of cables.

	RG174	RG223	RD316	MM11/50
Inner conductor	Copper clad steel	Silver plated copper	Silver plated copper clad steel	Silver plated copper
Dielectric	PE	PE	PTFE	PE
Outer conductor 1	Tinned copper braid	Silver plated copper braid	Silver plated copper braid	Silver plated copper braid
Outer conductor 2	None	Silver plated copper braid	Silver plated copper braid	Silver plated copper braid
Shielding	None	None	None	mu-metal
Jacket	PVC	PVC	FEP	PVC

which associated detector signal they represent.

Up to seven ADC cards are connected to a CPCI CPU (Compact Peripheral Component Interconnect Central Processing Unit) which is used for setup and control of the ADCs and readout of the parameters. Two CPCI crates are used to fully accommodate the ADC cards needed for SAGE. One TDRi card is responsible for providing the initial clock signal and a synchronisation pulse to all the ADC cards of one crate. The synchronisation pulse is used to ensure that the individual clock of each ADC card is synchronised with the rest. Each ADC card has an external trigger input that in the case of SAGE is used for the sync input from the TDRi card since a separate software trigger is responsible for triggering each channel.

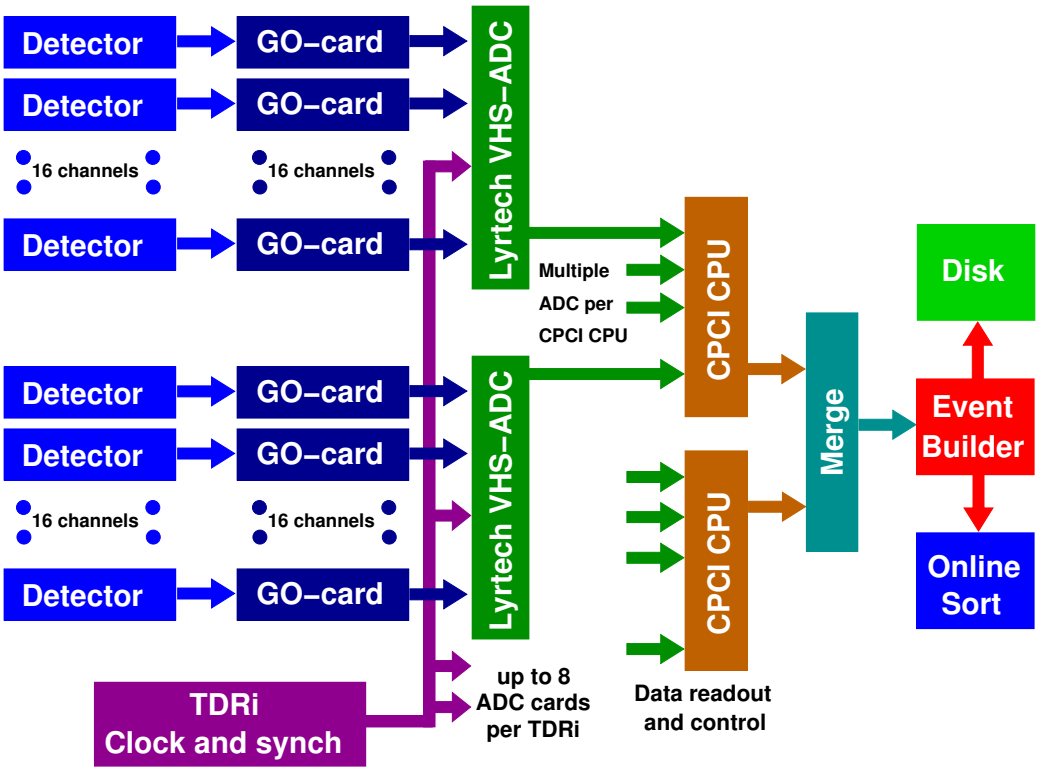

Figure 4.26: Block diagram of the digital electronics used in SAGE.

The timestamped parameters from all the individual ADC channels are sent from the CPCI CPUs to the Merge. Here the timestamped data words are merged into

chronological order. The data are then filtered using a software trigger to reduce their size so they can be saved on disk or passed through to the on-line sort code. From the Merge the parameters can be optionally read into the Event Builder where the events are reconstructed in real time using temporal and spatial correlations defined by the physics of the experiment.

The software trigger is applied either to the focal plane or to the prompt detectors. In the first case whenever any data are detected in any of the focal plane detectors then any data that are present within a certain time window are recorded. In the latter case the trigger is placed on the multiplicity of a prompt event. For example it can be required that only fold-two or fold-three events are recorded. The two different triggers can be used in conjunction.

Chapter 5

Summary and Conclusion

The SAGE spectrometer was designed and built by a collaboration from the Universities of Liverpool in the UK and Jyväskylä in Finland and the STFC Daresbury Laboratory. SAGE allows cross-coincidence measurements of γ rays and internal conversion electrons by combining a germanium detector array with a silicon detector and an electron transport system. The spectrometer is coupled with the RITU gas-filled recoil separator and the GREAT focal-plane spectrometer for recoil-decay tagging studies.

The individual parts of the setup, such as the solenoid coils, high-voltage barrier and detector electronics, are optimised for electron transmission efficiency, recoil acceptance in RITU and spectral response. The spectrometer employs fully digital front-end electronics and high-gain hybrid preamplifiers.

SAGE was successfully commissioned in the University of Jyväskylä and electron-γ cross-coincidences were observed. Figure 5.1 shows SAGE during the final preparations before getting beam on target for the first time. In Figure 5.2 the collaborators right after the first electron spectrum was observed.

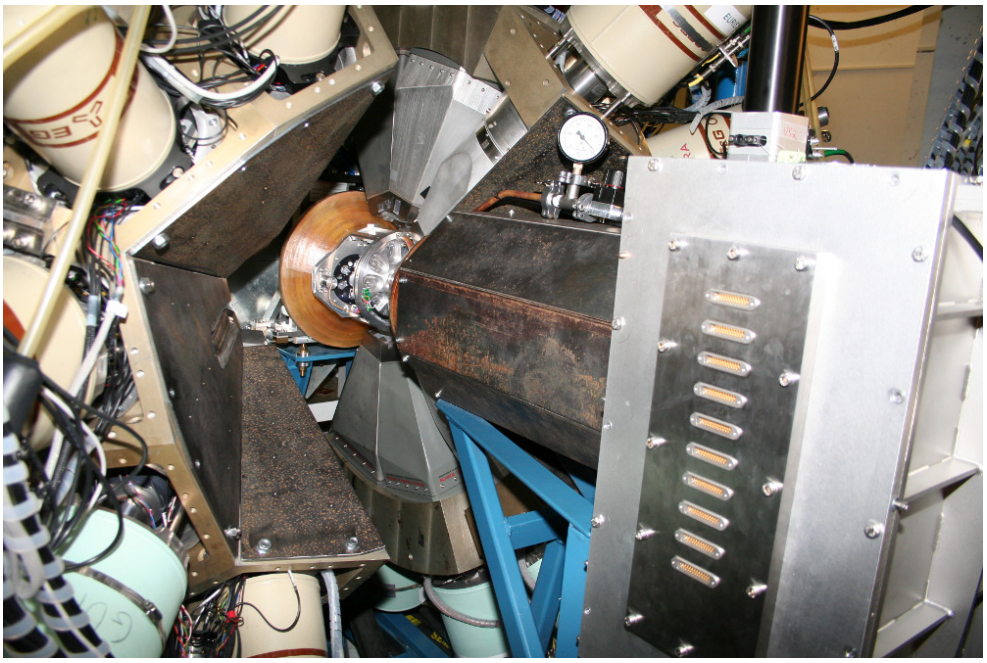

Figure 5.1: The SAGE spectrometer during the final preparations before being fully commissioned.

Figure 5.2: After the first electron spectrum was observed.

One reaction tried during the commissioning was ^{168}Er(^{16}O,4n)^{180}Os. Osmium has electron binding energies of B_K=73.87 keV, B_{L_I}=12.97 keV, $B_{L_{II}}$=12.38 keV and $B_{L_{III}}$= 10.87 keV. The decay scheme of the lower transitions of the ground-state band in ^{180}Os is shown in Figure 5.3. The energies are a weighted average of the values reported in [Li99] using a ^{150}Nd(^{36}S,6nγ) reaction, [Dr82, Li88] using ^{166}Er(^{18}O,4nγ) and [Dr82, Dr90] where the reaction ^{168}Er(^{16}O,4nγ) was used. The ICCs for the E2 transitions under study in osmium are presented in Table 5.1.

Figure 5.3 shows the ICE spectrum obtained when gating on the 386.4 keV and 510.1 keV γ rays, as shown in the inset. Gating on the 132.1 keV L electrons the γ-ray spectrum shown in Figure 5.4 is observed. No Compton suppression or recoil gates were used in these spectra.

Table 5.1: ICCs of the ground-state band transitions of ^{180}Os [Ki08].

E_γ [keV]	α	α_K	α_{L_I}	$\alpha_{L_{II}}$	$\alpha_{L_{III}}$
132.1	1.468	0.473	0.0527	0.390	0.308
276.5	0.1175	0.0732	0.00918	0.01552	0.00896
386.4	0.0445	0.0315	0.00414	0.00391	0.00192
462.2	0.0278	0.0205	0.00275	0.00192	0.000866
510.1	0.0217	0.01637	0.00221	0.001306	0.000564
541.2	0.0188	0.01435	0.00194	0.001042	0.000438
566.1	0.01690	0.01299	0.001758	0.000878	0.000362

A different reaction studied during the commissioning was ^{144}Sm(^{40}Ar,4n)^{180}Hg. For ^{180}Hg the lower transitions of the ground-state band are shown in Figure 5.5 [Ko00]. The electron binding energies of mercury are B_K=83.10 keV, B_{L_I}=14.84 keV, $B_{L_{II}}$=14.20 keV and $B_{L_{III}}$= 12.28 keV, and the ICCs for the ground-state band transitions are listed in Table 5.2.

An ICE recoil-gated spectrum obtained when gating on the 272.4 keV and 434.3 keV

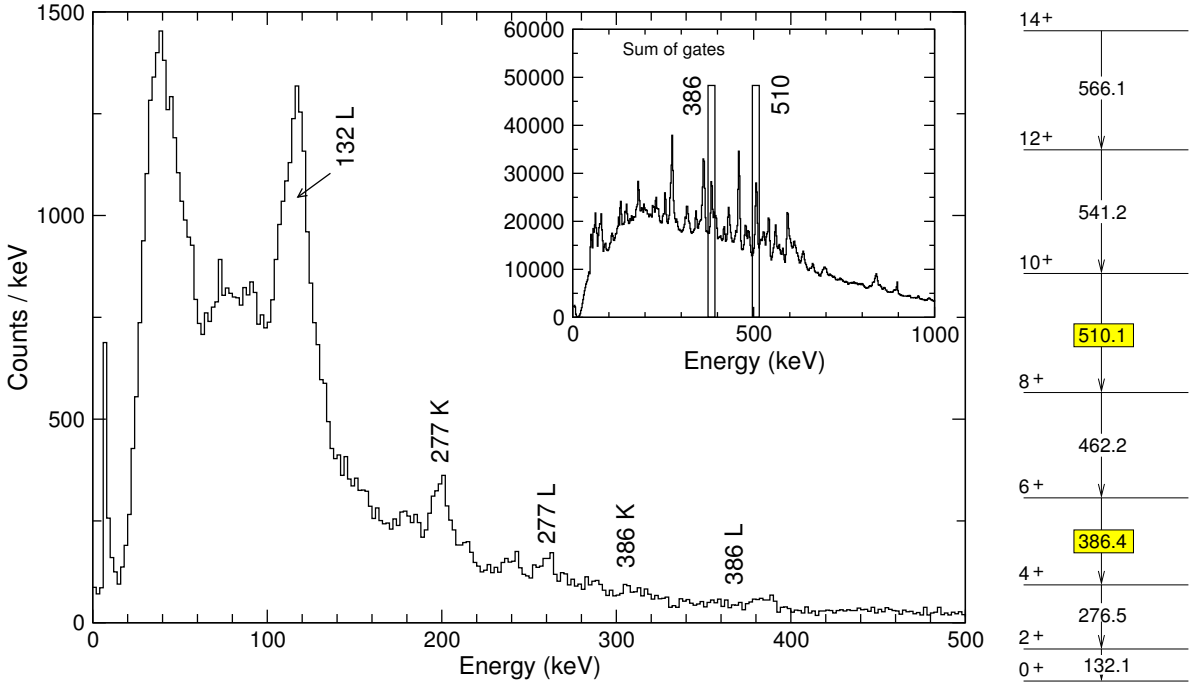

Figure 5.3: An ICE spectrum of ^{180}Os obtained when gating on the 386.4 keV and the 510.1 keV γ rays of the ground-state band as shown in the inset. On the right-hand side a partial level scheme of ^{180}Os is displayed with the gated transitions highlighted.

γ rays, is shown in Figure 5.5. Gating on the 272.4 keV K electrons gives the γ-ray recoil-gated spectrum shown in Figure 5.6.

Table 5.2: ICCs of the ground-state band transitions of ^{180}Hg [Ki08].

E_γ [keV]	α	α_K	α_{L_I}	$\alpha_{L_{II}}$	$\alpha_{L_{III}}$
434.3	0.0382	0.0266	0.00375	0.00358	0.001512
272.4	0.1426	0.0797	0.01075	0.0238	0.01276
326.0	0.0835	0.0517	0.00712	0.01132	0.00554
404.5	0.0460	0.0312	0.00438	0.00475	0.00208

When studying electron-γ cross coincidences in both the reactions described here,

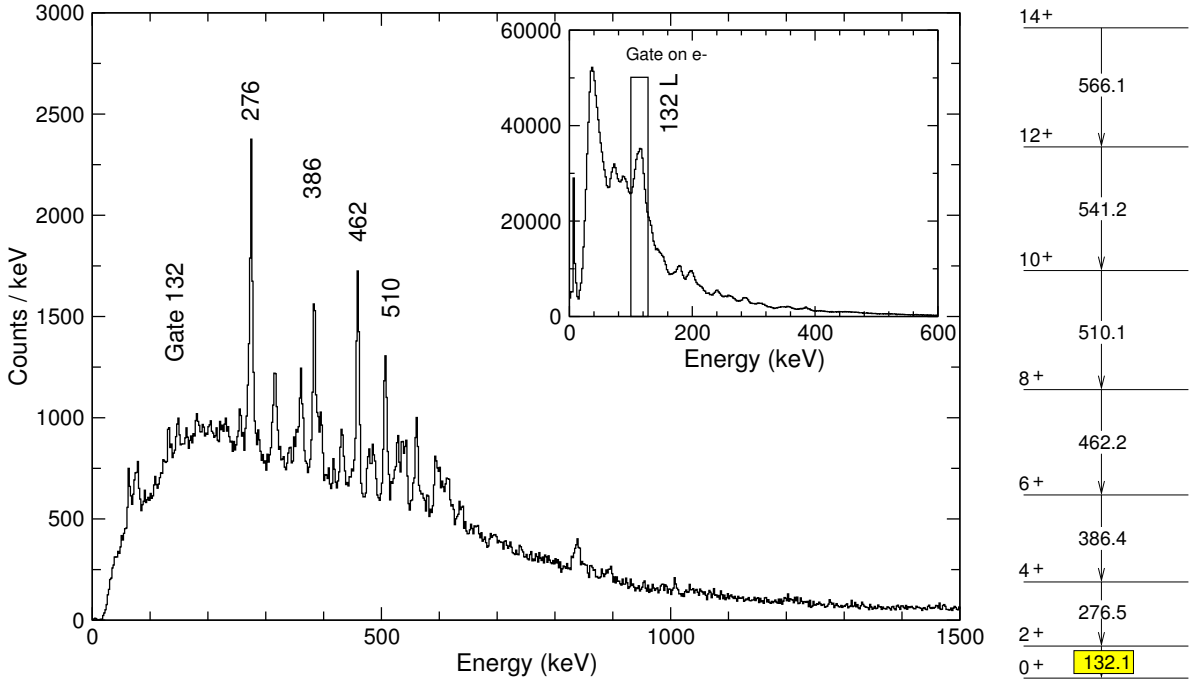

Figure 5.4: A γ-ray spectrum of ^{180}Os obtained when gating on the 132.1 keV L γ ray. The gate is shown in the inset and also on the level scheme on the right-hand side of the figure.

applying different electron or γ-ray gates yields spectra showing the desired behaviour. That is by gating on one of the ground state band electrons, in the resulting γ-ray spectrum the corresponding γ-ray peak is suppressed whereas the other ground state band decays are clearly seen. Additionally transitions belonging to side bands feeding into the ground-state band can be seen. Equivalently gating on a ground-state γ ray gives ICE spectra where the corresponding electron peaks are suppressed but other ground-state band decays are present.

For example in the spectrum in Figure 5.4 where a gate was placed on the 132 keV L electrons, the 132 keV peak is not present in the γ-ray spectrum but the other ground state-band transitions are clearly present. The same behaviour is observed in the spectrum of Figure 5.6 when gating on the 272 keV K electrons. The same is true for electron spectra obtained when gating on γ rays.

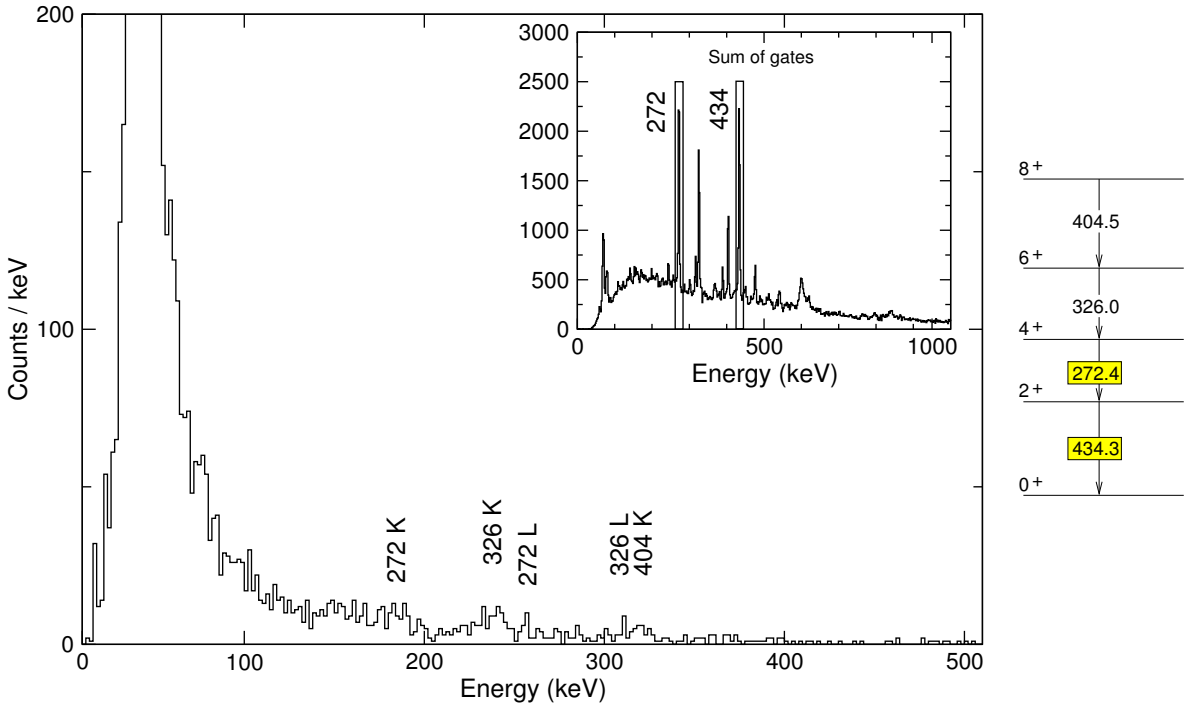

Figure 5.5: The recoil-gated ICE spectrum in ^{180}Hg obtained when gating on the 272.4 keV and 434.3 keV γ rays of the ground-state band. The gates are shown in the inset and the level scheme on the right.

When gates are placed on the background in the γ or ICE spectra the resulting spectrum has no apparent structure. This proves that the peaks in the presented spectra are from true cross-coincidences and not random events.

The spectra presented in Figures 5.3, 5.4, 5.5 and 5.6 are preliminary and cleaner spectra with increased statistics can be obtained from detailed offline analysis. It is important to note that the observed ground-state band decays agree well with the previously published values.

The purpose of these spectra is to highlight that the electron and γ-ray parts of the SAGE spectrometer work well both independently and in conjunction, without the one interfering with the other. Recoil gating using GREAT and RITU was successfully employed during the commissioning.

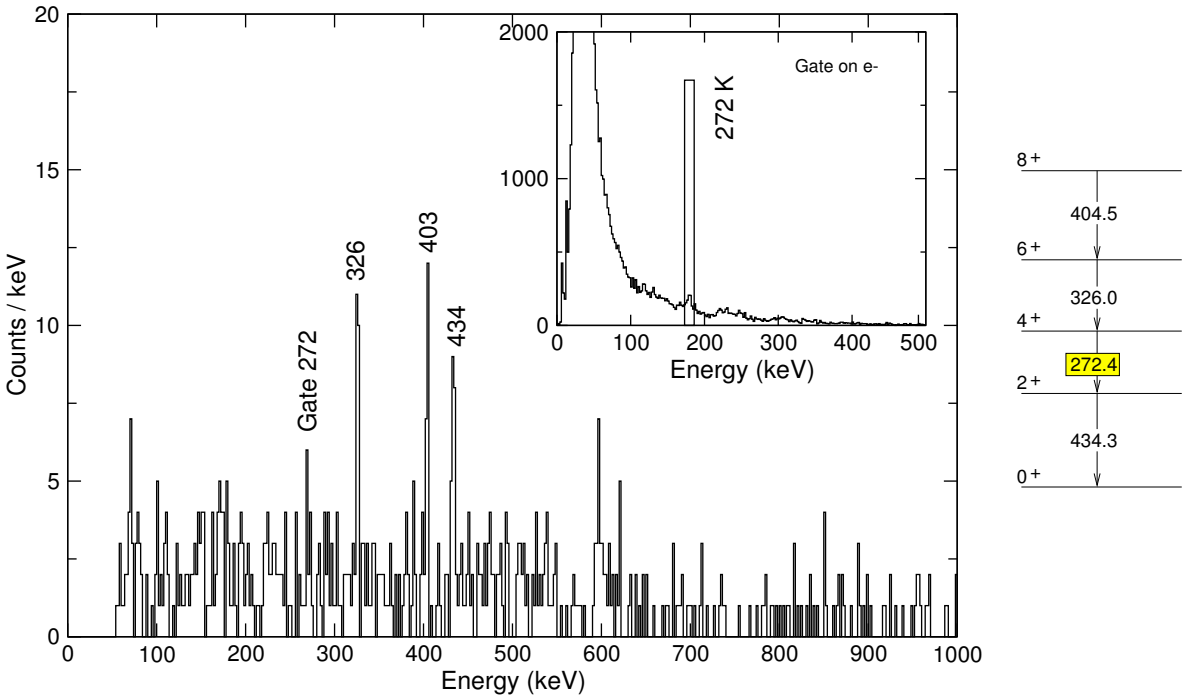

Figure 5.6: Recoil-gated γ-ray spectrum in ^{180}Hg when gating on the 272.4 keV K component of the ground-state band as shown in the inset.

The outcome of the commissioning experiments is that the main requirements and design goals set for SAGE have been achieved. Checking the list presented in Section 3.2 one can see that the γ-ray detection efficiency and resolution have not been affected by the electron part, the low-energy electron background is successfully suppressed and the electron transmission efficiency agrees within error bars with the predicted values. The measured transmission efficiency is not presented in this thesis as not all the required measurements were performed by the time of publication.

On the data acquisition front the digital front-end electronics operate almost flawlessly allowing measurements at high rates with no energy deterioration. Rates of up to 45 kHz at the Phase I detectors were achieved without difficulty.

Even though the spectrometer works according to the design specifications there are still some electronics issues that need addressing. A course of action has been

decided and a series of tests and optimisations will be performed before the next SAGE experimental campaign.

A number of experiments have been approved related both with the superheavy nuclei project and the search for shape coexistence in lead and mercury nuclei. Already before submitting the final version of this thesis two SAGE experiments were performed to look for shape coexistence in radon and lead nuclei. No results are presented here from these experiments as the analysis is ongoing. A brief analysis of the data proves that SAGE works well within the design criteria and that by further improving the stability and resolution characteristics of the electron part some wonderful experimental results can be expected in the future.

Appendices

Appendix A

Electromagnetism basics related to the simulations

This section does not try to explain electromagnetism but rather to present the equations useful for simulating electric and magnetic fields from given charge or current distributions, respectively[1].

Electromagnetism is based on Maxwell's equations that in SI units are expressed as:

- Coulomb's Law

$$\vec{\nabla} \cdot \vec{D} = \rho_f, \tag{A.1}$$

- Absence of free magnetic poles

$$\vec{\nabla} \cdot \vec{B} = 0, \tag{A.2}$$

- Faraday's Law

$$\vec{\nabla} \times \vec{E} = -\frac{\partial \vec{B}}{\partial t}, \tag{A.3}$$

- Ampère's Law with Maxwell's correction

$$\vec{\nabla} \times \vec{H} = \vec{j_f} + \frac{\partial \vec{D}}{\partial t}. \tag{A.4}$$

[1]Information from books [Gr90, Ja99, Gr99, Gr00, St01] were used in this appendix.

Where D is the electric flux density or electric displacement, ρ_f is the free charge density, B is the magnetic flux density, E the electric field intensity, H the magnetic field intensity and j_f the current density.

In the case where static electric and magnetic fields are considered Maxwell's equations are reduced to:

$$\vec{\nabla} \cdot \vec{D} = \rho_f, \tag{A.5}$$

$$\vec{\nabla} \cdot \vec{B} = 0, \tag{A.6}$$

$$\vec{\nabla} \times \vec{E} = 0, \tag{A.7}$$

$$\vec{\nabla} \times \vec{H} = \vec{j_f} \tag{A.8}$$

and the solution to a general static electromagnetic problem can be derived simply by solving the electrostatic and magnetostatic equations individually and combining the results.

The equation of continuity (Equation A.9) relates the total macroscopic charge and current densities at each point and it expresses the conservation of charge in differential form,

$$\frac{\partial \rho}{\partial t} + \vec{\nabla} \cdot \vec{j} = 0. \tag{A.9}$$

When Maxwell's equations are combined with the Lorentz force equation (Equation A.10) and Newton's second law of motion the classical dynamics of interacting charged particles and EM fields can be completely described.

$$\vec{\mathbf{F}} = q(\vec{E} + \vec{v} \times \vec{B}), \tag{A.10}$$

with q being the charge of a particle moving with velocity $\vec{v}$.

Besides Maxwell's equations other useful formulae can be used in the study of electromagnetic fields. For example, the magnetic field of a steady line current is given by the Biot-Savart Law,

$$\vec{B}(\vec{r_0}) = \frac{\mu_0 I}{4\pi} \oint_C \frac{d\vec{l'} \times \vec{r}}{r^3}, \tag{A.11}$$

where the integration is along the current path in the direction of the flow, $\vec{dl'}$ is an element of length along the path at $\vec{r_c}$ and $\vec{r}$ is the vector from the source to the point $\vec{r_0}$, where $\vec{r} = \vec{r_0} - \vec{r_c}$, as shown in Figure A.1.

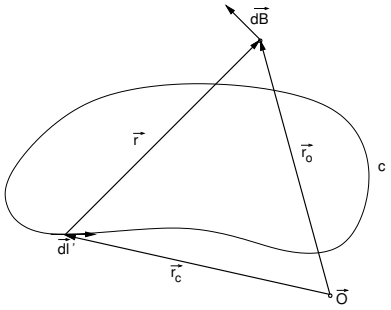

Figure A.1: Geometry used to determine the magnetic field of a current loop with the Biot-Savart Law.

The electric scalar potential of a given stationary charge distribution can be calculated using Poisson's equation (Equation A.12) or if no charge is present in the area of interest this is reduced to Laplace's equation (Equation A.13),

$$\nabla^2 V = -\frac{\rho}{\epsilon}, \tag{A.12}$$

$$\nabla^2 V = 0. \tag{A.13}$$

The constant ϵ in Equation A.12 is the dielectric constant of the material of interest. Using the dielectric constant the electric displacement $\vec{D}$ is related to the electric field $\vec{E}$:

$$D = \epsilon E. \tag{A.14}$$

In the case of magnetostatic problems, Equations A.6 and A.8 must be obeyed. To achieve this easily a magnetic vector potential $\vec{A}$ is defined as:

$$\vec{B} = \vec{\nabla} \times \vec{A}. \tag{A.15}$$

As for the dielectric constant, the magnetic permeability, μ, can be defined that combines the magnetic field flux density, $\vec{B}$, with the field's intensity, $\vec{H}$:

$$\vec{B} = \mu \vec{H}. \tag{A.16}$$

From the above equations for the magnetic field an equation similar to Poisson's equation is derived:

$$\vec{\nabla} \times (\frac{1}{\mu}\vec{\nabla} \times \vec{A}) = \vec{j}, \tag{A.17}$$

and if we assume $\vec{\nabla} \cdot \vec{A} = 0$ then Equation A.17 reduces to:

$$\nabla^2 \vec{A} = \mu\vec{j}. \tag{A.18}$$

A.1 Electron motion in electromagnetic fields

To show how electrons move inside an electromagnetic field, the simple example of an electron moving in a uniform, static, magnetic field $\vec{B}$ will be used. The equations of motion in this case can be written as:

$$\frac{d\vec{p}}{dt} = \frac{e}{c}\vec{v} \times \vec{B} \qquad \text{and} \qquad \frac{dE}{dt} = 0, \tag{A.19}$$

where $\vec{v}$ is the particle's velocity. Since the energy is constant in time, the magnitude of the velocity is constant as well.

Solving these equations shows that the particle moves in a circle of radius r perpendicular to the magnetic field. It also has a velocity component parallel to the field meaning that it will move in a helix along the field lines, as the circular and the linear motions combine.

The gyration radius r of the particle is given by:

$$r = \frac{cp_\perp}{eB}, \tag{A.20}$$

where $p_\perp$ is the transverse momentum of the particle.

In the case where the particle moves in combined electric and magnetic fields then the motion is the same as described above with the difference that the electric field will add additional acceleration to the particle.

In the case of SAGE the electrons move along a helical path in the direction of the magnetic field lines. The less energetic ones are deflected by the high-voltage barrier

and the more energetic are decelerated when approaching it and then accelerated with an equal amount when moving away from it.

A detailed analysis on the motion of charged particles in electric and/or magnetic fields is made in [Ja99].

Appendix B

The simulation packages

The Vector Fields OPERA 3D simulation environment [VF07] contains a series of analysis programs including "TOSCA magnetostatics" and "TOSCA electrostatics" that were used in the simulations made for SAGE. Electromagnetic simulations are provided by independently solving the electric and magnetic equations and combining the results.

A modeller is available in OPERA 3D for the construction of a model in three-dimensional space using geometric primitive volumes and Boolean operations. A model can also be extracted from a two-dimensional cross-section. The coils of SAGE were modelled using conductors, which are available for modelling in different shapes and sizes. Any symmetries present in the model can be exploited for simplifying the model and making the simulation faster.

The user can define properties for each type of material used in the model. If a magnetic field analysis is desired then a series of options for the permeability is available. For non-linear permeability a curve of magnetic flux density versus the magnetic field intensity (BH curve) can be assigned from the available library which allows the user to add new materials if needed. When analysing an electric field problem the conductivity and relative permittivity of each material can be defined.

Before proceeding to the analysis the model needs to be meshed. A two step procedure is followed where initially the surface is meshed and then the volume. The

user can define for the surface the maximum mesh element size, maximum angle between elements and maximum deviation from the surface, and for both surface and volume mesh the absolute tolerances.

When the model is fully defined and meshed the analysis database is prepared and solved. The results of the simulation are viewed in the "Post-Processor" where one can project a number of parameters on different surfaces or axes or output the values for analysis or representation using different software.

A similar procedure (building of model, meshing, defining border and material properties and setting up and solving the problem) is used in the Finite Element Method Magnetic (FEMM) [Me06] simulation package. FEMM is a suite of programs for solving low frequency electromagnetic problems on two-dimensional planar and axisymmetric domains. A problem can be solved quickly in two dimensions with FEMM and the results have been shown to agree with the ones from OPERA 3D.

For comparison Figure B.1 shows plots of the magnetic field on the solenoid axis for the same geometry using OPERA 3D and FEMM. In these simulations a 700 A current through the coils was used. The 3.2° angle between the beam and solenoid axes was incorporated only in the OPERA 3D simulation. This is because in FEMM calculations are axisymmetric, so the angle would produce conical coils instead of solenoids. This leads to a difference in the calculated fields between the target and detector positions. This effect disappears at the region where the two axes are collinear.

FEMM was used to quickly see effects of changes in coil geometry, whereas OPERA 3D was used to simulate almost finalised geometries or cases where no symmetries could be applied to extend the two dimensional space to three dimensions in FEMM.

For solving electrostatic problems both OPERA and FEMM solve Poisson's equation (Equation A.12) in the frame of the user-defined conditions. Following this the electric field intensity and flux density are calculated.

For magnetostatic problems FEMM solves Equation A.17 and by differentiating $\vec{A}$; $\vec{B}$ and $\vec{H}$ are deduced. This process is more complicated in the case of OPERA. The program uses a combination of total (for regions were currents do not flow) and

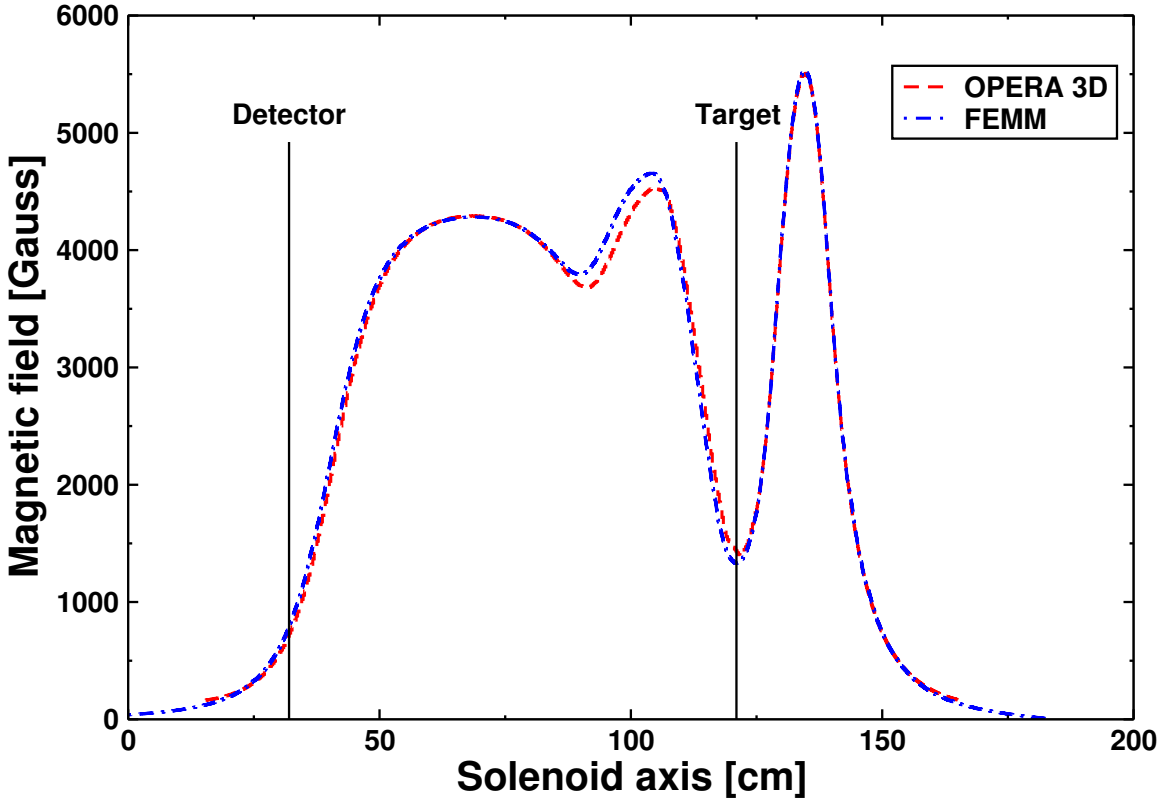

Figure B.1: A comparison of the magnetic field on the solenoid axis calculated using OPERA 3D and FEMM.

reduced scalar potentials (in regions where currents flow i.e. conductors) to overcome any difficulties.

In the regions where currents flow, the total field intensity can be defined by summing the reduced (H_m) and conductor (H_s) field intensities, namely:

$$\vec{H_m} = -\nabla\phi \tag{B.1}$$

and

$$\vec{H_s} = \int_{\Omega_J} \frac{\vec{J} \times \vec{R}}{\left|\vec{R}\right|^3} d\Omega_J. \tag{B.2}$$

In the volumes where no currents are flowing a total field intensity is represented

using the total magnetic scalar potential as:

$$\vec{H} = -\nabla\psi, \tag{B.3}$$

where the total magnetic scalar potential satisfies:

$$\nabla \cdot \mu\nabla\psi = 0. \tag{B.4}$$

Appendix C

Technical specification of magnetic coils

The coils are made from winding glass/epoxy impregnated copper conductors. There is 1 mm of epoxy between two conductors (0.5 mm around each conductor) and 1.5 mm on the outside of each coil (0.5 mm from the external conductors plus 1 mm around the whole coil). Individual conductors have the geometry shown in Figure C.1 and specifications as in Table C.1. The diameter indicated by "d" in the drawing is the central hole used for water cooling.

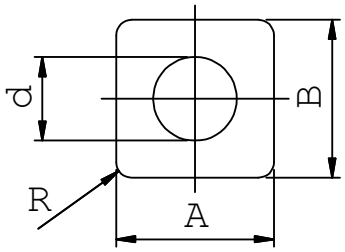

Figure C.1: Cross-section of the solenoid coil conductors.

Figure C.2 shows the cross-section of the SAGE solenoid coils. In this figure the green squares demonstrate where one conductor crosses-over to the next loop. In the case of the main coil they denote how neighbouring conductors are coupled. The

Table C.1: Specifications of the solenoid coils and the individual conductors dimensions as shown in Figure C.1.

	Main coil	Upstream coil	Downstream coil
A [mm]	9	9	8
B [mm]	9	9	8
d [mm]	∅5	∅6	∅5
R [mm]	1	1	1
Weight [kg]	79.4	39.5	33.1
Resistance at 20° C [Ω]	0.05	0.02	0.02

arrows show the individual cooling circuits. The effect of water cooling in the main and upstream coils is clearly visible in the infrared camera shot shown in Figure C.3.

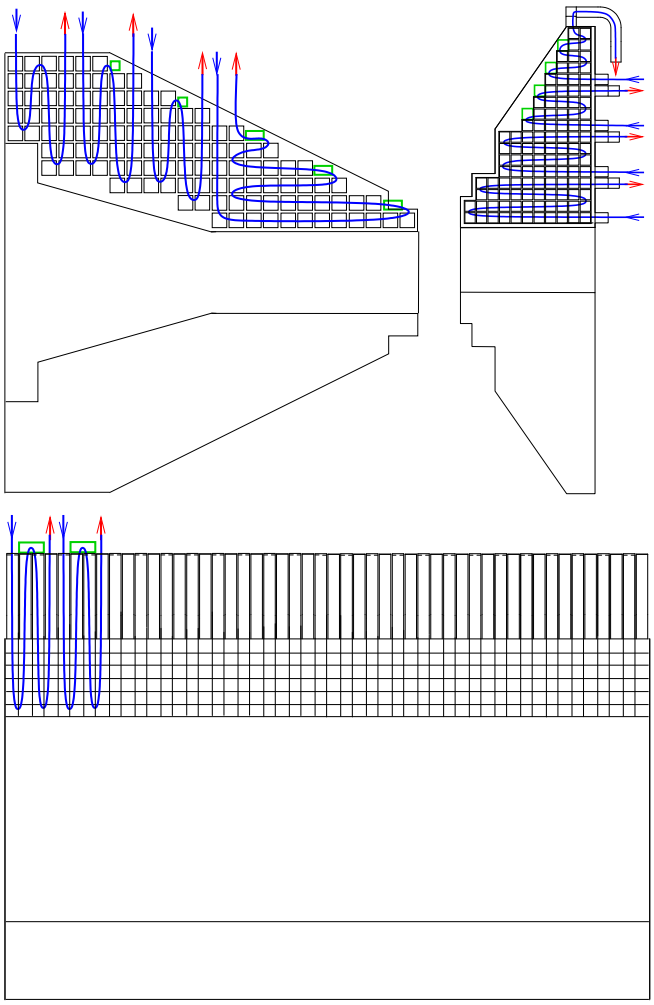

Figure C.2: Cross-section of the magnetic coils of SAGE. Individual cooling circuits are indicated with continuous lines. Clockwise from top: Upstream, downstream and main coil. The arrows indicate where the cool water (blue) enters the cooling circuit and where the warm water (red) exits. The green squares show cross-overs or coupling of different conductors.

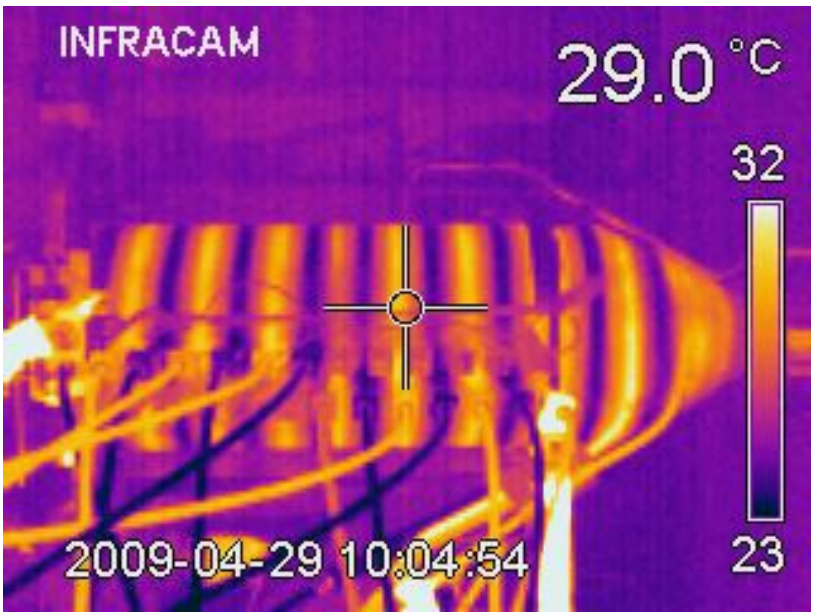

Figure C.3: Infrared camera picture showing the effect of water cooling on the main and upstream coils. 600 A current was used through the coils. Temperature scale is shown in the vertical bar on the right.

Appendix D

List of publications

1. **Towards combining in-beam γ-ray and conversion electron spectroscopy**
   P. Papadakis, R.-D. Herzberg, J. Pakarinen, P.A. Butler, P.J. Coleman-Smith, J.R. Cresswell, P.T. Greenlees, P. Jones, R. Julin, I.H. Lazarus, S.C. Letts, R.D. Page, E. Parr, P. Peura, V.F.E. Pucknell, P. Rahkila, D.A. Seddon, J. Simpson, J. Sorri, J. Thornhill, D. Wells,
   AIP Conference Proceedings **1090**, pp. 14-20 (2009).

2. **Spectroscopy of Very Heavy Elements**
   P.T. Greenlees, R.-D. Herzberg, S. Ketelhut, D. Ackermann, P.A. Butler, A. Chatillon, S. Eeckhaudt, B.J.P. Gall, T. Grahn, C. Gray-Jones, A. Görgen, F.-P. Hessberger, U. Jakobsson, G.D. Jones, P. Jones, R. Julin, S. Juutinen, T.-L. Khoo, W. Korten M. Leino, S. Moon, M. Nyman, J. Pakarinen, P. Papadakis, P. Peura, P. Rahkila, M. Richer, D. Rostron, C. Santos, J. Sarén, C. Scholey, J. Sorri, S.K. Tandel, Ch. Theisen, J. Uusitalo, M. Venhart
   AIP Conference Proceedings **1012**, pp. 56 (2007).

3. **γ-Ray Spectroscopy at the Limits: First Observation of Rotational Bands in ^{255}Lr**
   S. Ketelhut, P.T. Greenlees, D. Ackermann, S. Antalic, E. Clment, I.G. Darby,

O. Dorvaux, A. Drouart, S. Eeckhaudt, B.J.P. Gall, A. Görgen, T. Grahn, C. Gray-Jones, K. Hauschild, R.-D. Herzberg, F.P. Hessberger, U. Jakobsson, G.D. Jones, P. Jones, R. Julin, S. Juutinen, T.-L. Khoo, W. Korten, M. Leino, A.-P. Leppänen, J. Ljungvall, S. Moon, M. Nyman, A. Obertelli, J. Pakarinen, E. Parr, P. Papadakis, P. Peura, J. Piot, A. Pritchard, P. Rahkila, D. Rostron, P. Ruotsalainen, M. Sandzelius, J. Sarén, C. Scholey, J. Sorri, A. Steer, B. Sulignano, Ch. Theisen, J. Uusitalo, M. Venhart, M. Zielinska, M. Bender, and P.-H. Heenen,

Phys. Rev. Lett. **102**, 212501 (2009).

4. **Bridging the nuclear structure gap between stable and super heavy nuclei**

   D. Seweryniak, T.-L. Khoo, I. Ahmad, F.G. Kondev, A. Robinson, S.K. Tandel, M. Asai, B.B. Back, M.P. Carpenter, P. Chowdhury, C.N. Davids, S. Eeckhaudt, J.P. Greene, P.T. Greenlees, S. Gros, K. Hauschild, A. Heinzg, R.-D. Herzberg, R.V.F. Janssens, D.G. Jenkins, G.D. Jones, S. Ketelhut, T. Lauritsen, C.J. Lister, A. Lopez-Martens, P. Marley, E.A. McCutchan, T. Nakatsukasa, P. Papadakis, D. Peterson, J. Qian, D. Rostron, I. Stefanescu, U.S. Tandel, X.F. Wang and S.F. Zhu,

   Nucl. Phys. A **834** (2010) 357c-361c.

Bibliography

[Af03] A.V. Afanasjev, T.L. Khoo, S. Frauendorf, G.A. Lalazissis and I. Ahmad, "Cranked relativistic Hartree-Bogoliubov theory: Probing the gateway to superheavy nuclei", *Phys. Rev.* C **67** (2003) 024309

[Ar00] P. Armbruster, "On the Production of Superheavy Elements", *Annu. Rev. Nucl. Part. Sci.* **50** (2000) 411

[Ar06] L. Arnold *et al.*, "TNT Digital Pulse Processor", *IEEE Transactions on Nuclear Science* Vol.**53** No.3 (2006) 723

[An00] A.N. Andreyev *et al.*, "A triplet of differently shaped spin-zero stated in the atomic nucleus ^{186}Pb", *Nature* **405** (2000) 430

[An08] J. Andrzejewski *et al.*, "Electron spectrometer for in-beam spectroscopy", *Nucl. Instr. and Meth.* A **585** (2008) 155

[Ba78] I.M. Band and M.B. Trzhaskovkaya, "Tables of the gamma-ray internal conversion coefficients for the K, L, M shells, 10<Z<104", *Leningrad Nuclear Physics Institute Report* (1978)

[Ba02] I.M. Band *et al.*, "Dirac-Fock Internal Conversion Coefficients", *At. Data Nucl. Data Tables* **81** (2002) 1

[Ba06] J.E. Bastin *et al.*, "In-beam gamma ray and conversion electron study of ^{250}Fm", *Phys. Rev.* C **73** (2006) 024308

[Be84] F.A. Beck, "Proc. of Intern. Conf. on Instr. for Heavy Ion Nucl. Research", ed. D. Shapira *Nucl. Sci. Research Conf. Series* **7** (1984) 129

[Be92] C.W. Beausang *et al.*, "Measurements on prototype Ge and BGO detectors for the EUROGAM array" *Nucl. Instr. and Meth.* A **313** (1992) 37

[Be99] M. Bender, K. Rutz. P.-G. Reinhard, J.A. Maruhn and W. Greier, "Shell structure of superheavy nuclei in self-consistent mean-field models" *Phys. Rev.* C **60** (1999) 034304

[Be01] M. Bender, W. Nazarewicz and P.-G. Reinhard, "Shell stabilization of super- and hyperheavy nuclei without magic gaps" *Phys. Lett.* B **515** (2001) 42

[Be03] M. Bender, P.-H. Heenen and P.-G. Reinhard, "Self-consistent mean-field models for nuclear structure" *Rev. Mod. Phys.* **75** (2003) 121

[Be85] T. Bengtsson and I. Ragnarsson, "Rotational bands and particle-hole excitations at very high spin" *Nucl. Phys.* A **436** (1985) 14

[Bl07] M. Block *et al.*, "Towards direct mass measurements of nobelium at SHIPTRAP" *Eur. Phys. J.* D **45** (2007) 39

[Bl10] M. Block *et al.*, "Direct mass measurements above uranium bridge the gap to the island of stability" *Nature* **463** (2010) 785

[Bo37] N. Bohr and F. Kalckar, *Mat. Fys. Medd. Dan. Vid. Selsk.* **14** (1937) no. 10

[Bo69] A. Bohr and B.R. Mottelson, "Nuclear Structure Volume I", *World Scientific* (1999)

[Bo75] A. Bohr and B.R. Mottelson, "Nuclear Structure Volume II", *World Scientific* (1999)

[Br83] K.-P. Brieger, W. Gerlach and J. Pelka, "Blocking capability of planar devices with field limiting rings", *Solid-State Electr.* **26** No. 8 (1983) 739

[Bü04] T. Bürvenich, M. Bender, J.A. Maruhn and P.-G. Reinhard, "Systematics of fission barriers in superheavy elements", *Phys. Rev.* C **69** (2004) 014307

[Bu87] P.A. Butler *et al.*, *Daresbury Annual Report* (1987/88) p. 120

[Bu96] P.A. Butler *et al.*, "Electron spectroscopy using a multi-detector array", *Nucl. Instrum. Meth.* A **381** (1996) 433

[Bu02] P.A. Butler *et al.*, "Conversion Electron Cascades in $^{254}_{102}$No" *Phys. Rev. Lett.* **89** (2002) 20

[Ca86] A. Carrington and H.W. Nicholson, "Electron Backscattering from a Silicon Detector from 0.182 to 0.579 MeV", *Nucl. Instrum. Meth* A **248** (1986) 425

[Ch97] R.R. Chasman and I. Ahmad, "Nuclear structure at A∼250 and the stability of the superheavy elements", *Phys. Lett.* B **392** (1997) 255

[Ch07] A. Chatillon *et al.*, "Observation of a Rotational Band in the Odd-Z Transfermium Nucleus $^{251}_{101}$Md", *Phys. Rev. Lett.* **98** (2007) 132503

[Ch56] E.L. Church and J. Weneser, "Electric-Monopole Transitions in Atomic Nuclei", *Phys. Rev.* **103** (1956) 1035

[Cu66] S.C. Curran and H.W. Wilson, "Proportional Counters and Pulse Ion Chambers", in "Alpha-, Beta-, Gamma-Ray Spectroscopy" ed. K. Siegbahn, *North-Holland* (1966)

[Ćw87] S. Ćwiok, J. Dudek, W. Nazarewicz, J. Skalski and T. Werner, "Singleparticle energies, wave functions, quadrupole moments and g-factors

in an axially deformed Woods-Saxon potential with applications to the two-centre type nuclear problems", *Comp. Phys. Comm.* **46** (1987) 379

[Ćw96] S. Ćwiok *et al.*, "Shell structure of the superheavy elements", *Nucl. Phys.* A **611** (1996) 211

[Ćw05] S. Ćwiok, P.-H. Heenen and W. Nazarewicz, "Shape coexistence and triaxiality in the superheavy nuclei", *Nature* **433** (2005) 705

[Da12] J. Danysz, "Sur les rayons β de la famille du radium", *Le Radium* **9** (1912) 1

[Da13] J. Danysz, "Sur les rayons β des radiums B, C, D, E", *Le Radium* **10** (1913) 4

[De06] J.-P. Delaroche, M. Girod, H. Goutte and J. Libert, "Structure properties of even-even actinides at normal and super deformed shapes analysed using the Gogny force", *Nucl. Phys.* A **771** (2006) 103

[Di84] R.M. Diamond and F.S. Stephens, "Proc. of Intern. Conf. on Instr. for Heavy Ion Nucl. Research", ed. D. Shapira *Nucl. Sci. Research Conf. Series* **7** (1984) 259

[Di91] J.S. Dionisio *et al.*, "Influence of target properties on prompt in-beam electron spectra", *Nucl. Instr. Meth.* A **303** (1991) 9

[Di95] J.S. Dionisio *et al.*, "Target structure and in-beam electron spectra", *Nucl. Instr. Meth.* A **362** (1995) 122

[Di99] J.S. Dionisio *et al.*, "Recent developments of multi e-γ spectrometers", *Nucl. Instr. Meth.* A **437** (1999) 282

[Dö83] F. Dönau and S. Frauendorf, "High angular moment properties of nuclei", ed. N.R. Johnson, *Proceedings of the Conference on High Angular Momentum Properties of Nuclei, Oak Ridge, 1982* (1983) 143

[Dö87] F. Fönau, "Electromagnetic radiation of rotational nuclei", *Nucl. Phys.* A **471** (1987) 469

[Dr82] G.D. Dracoulis *et al.*, "High-spin yrast and non-yrast bands in ^{176}Os, ^{178}Os and ^{180}Os", *Nucl. Phys.* A **383** (1982) 119

[Dr90] G.D. Dracoulis *et al.*, "Conversion coefficients and yrast state spins in ^{180}Os", *Nucl. Phys.* A **509** (1990) 605

[Eb92] J. Eberth *et al.*, "Development of a Composite Ge Detector for EUROBALL", *Prog. Part. Nucl Phys.* **28** (1992) 495

[Ee06] S. Eeckhaudt, *University of Jyväskylä, PhD thesis* (2006)

[Ej89] H. Ejiri and M.J.A. de Voigt, "Gamma-Ray and Electron Spectroscopy in Nuclear Physics", *Oxford Science Publications* (1989)

[Fi96] R.B. Firestone, "Table of Isotopes", ed. V.S. Shirley, *John Wiley and Sons*(1996)

[Fr96] P. Fröbrich and R. Lipperheide, "Theory of Nuclear Reactions", *Clarendon Press* (1996)

[Ga01] D. Gassmann *et al.*, "Conversion electron spectroscopy of superdeformed minimum of ^{240}Pu", *Phys. Lett.* B **497** (2001) 181

[Ge08] J. Gerl *et al.*, "Internal conversion coefficients of high multipole transitions: Experiment and theories" , *At. Data Nucl. Data Tables* **94**, (2008) 701

[Gi66] W.M. Gibson, G.L. Miller and P.F. Donovan, "Semiconductor Particle Spectrometers", in "Alpha-, Beta-, Gamma-Ray Spectroscopy" ed. K. Siegbahn, *North-Holland* (1966)

[Go66] M. Goldhaber and A.W. Sunyar, "Classification of Nuclear Transition Rates", in "Alpha-, Beta-, Gamma-Ray Spectroscopy" ed. K. Siegbahn, *North-Holland* (1966)

[Go98] Goodfellow, "Catalogue 1998/99", *Goodfellow* (1998)

[Gr60] R.L. Graham *et al.*, "A one-meter-radius iron-free double-focusing $\pi\sqrt{2}$ spectrometer for β-ray spectroscopy with a precision of 1:10^5", *Nucl. Instr. and Meth.* **9**, (1960) 245

[Gr90] I.S. Grant and W.R. Phillips, "Electromagnetism", *John Wiley and Sons* (1990)

[Gr08] P.T. Greenlees *et al.*, "High-K structure in ^{250}Fm and the deformed shell gaps at N=152 and Z=100", *Phys. Rev.* C **78**, (2008) 021303(R)

[Gr00] D. Green, "The Physics of Particle Detectors", *Cambridge University Press* (2000)

[Gr99] D.J. Griffiths, "Introduction to Electrodynamics", *Prentice Hall* (1999)

[Gr67] J.R. Grover, "Shell-Model Calculations of the Lowest-Energy Nuclear Excited States of Very High Angular Momentum", *Phys. Rev.* **157**, (1967) 832

[Ha24] O. Hahn and L. Meitner, *Z. Phys.* **29** (1924) 161

[Ha68] R.S. Hager and E.C. Seltzer, *Nucl. Data Tables* A **4** (1968) 1

[Ha09] F. Hartman, "Basic Principles of a Silicon Detector", in "Evolution of Silicon Sensor Technology in Particle Physics" *Springer*(2009)

[He01] R.-D. Herzberg *et al.*, "Spectroscopy of transfermium nuclei: ^{252}No" *Phys. Rev.* C **65** (2001) 014303

[He02] R.-D. Herzberg *et al.*, "In-beam spectroscopy of ^{253,254}No" *Eur. Phys. J* A **15** (2002) 205

[He06] R.-D. Herzberg *et al.*, "Nuclear isomers in superheavy elements as stepping stones towards the island of stability" *Nature* **442** (2006) 896

[He08] R.-D. Herzberg and P.T. Greenlees, "In-beam and decay spectroscopy of transfermium nuclei" *Prog. Nucl. Part. Phys.* **61** (2008) 674

[He09] R.-D. Herzberg *et al.*, "Structure of rotational bands in ^{253}No" *Eur. Phys. J.* A **42**, 3 (2009) 333

[He94] K. Heyde, "Basic Ideas and Concepts in Nuclear Physics", *IOP Publishing Ltd*, (1994)

[Hu32] H.R. Hulme, "The Internal Conversion Coefficient for Radium C", *Proc. R. Soc. Lond.* A **138** (1932) 643

[Hu36] H.R. Hulme, "On the Interaction of Two Particles", *Proc. R. Soc. Lond.* A **154** (1936) 487

[Ja83] M. Jääskeläinen *et al.*, "The spin spectrometer: Design, instrumentation and response characteristics of $4\pi\gamma$-ray multidetector system", *Nucl. Instrum. and Meth.* **204** (1983) 385

[Ja99] J.D. Jackson, "Classical Electrodynamics", *John Wiley and Sons* (1999)

[Ka01] H. Kankaanpää, "In-beam spectroscopy of very heavy elements", *University of Jyväskylä, PhD Thesis* (2001)

[Ka04] H. Kankaanpää *et al.*, "In-beam electron spectrometer used in conjunction with a gas-filled recoil separator", *Nucl. Instrum. and Meth.* A **534** (2004) 503

[Ka57] H. Kanter, "Zur Rückstreuung von Elektronen im Energiebereich von 10 bis 100 keV", *Ann. Phys.* **20** (1957) 144

[Ka67] Y.C. Kao and E.D. Wolley, "High-Voltage Planar *p-n* Junctions", *Proceedings of the IEEE* **55** No. 8 (1967) 1409

[Ke92] C. Kelbch *et al.*, "Delta-electron emission in fast heavy ion-atom collisions: observations of new phenomena and breakdown of common scaling laws", *A. Phys. D -Atoms, Molecules and Clusters* **22** (1992) 713

[Ke09] S. Ketelhut *et al.*, "γ-Ray Spectroscopy at the Limits: First Observation of Rotational Bands in ^{255}Lr", *Phys. Rev. Lett.* **102** (2009) 212501

[Ki05] T. Kibédi and R.H. Spear, "Electric monopole transitions between 0^+ states for nuclei throughout the periodic table", *At. Data Nucl. Data Tables* **89**, (2005) 77

[Ki08] T. Kibédi *et al.*, "Evaluation of Theoretical Conversion Coefficients using BrIcc", *Nucl. Instrum. and Meth.* A **589** (2008) 202

[Ki97] M. Kidera *et al.*, "Development of a compact multi-electron detector for in-beam spectroscopy", *Nucl. Instrum. and Meth.* A **397** (1997) 304

[Kl69] B. Klank and R.A. Ristinen, "Proc. Int. Conf. on Radioactivity in Nuclear Spectroscopy", ed. J.H. Hamilton and J.C. Manthuruthil, (1969)

[Kl72] J.Van Klinken and K. Wisshak, "Conversion Electrons Separated from High Background", *Nucl. Intsr. and Meth.* **98** (1972) 1

[Kn00] G.F. Knoll, "Radiation Detection and Measurement", *John Wiley and Sons* (2000)

[Ko65] O.B. Kofoed-Hansen, J. Linhard and O.B. Nielsen, *Kgl. Dansk. Vid. Selsk. Mat. Fys. Medd.* **29** (1965) no. 6

[Ko00] F.G. Kondev *et al.*, "Interplay between octupole and quasiparticle excitations in ^{178}Hg and ^{180}Hg", *Phys. Rev.* C **62** (2000) 044305

[Kr88] K.S. Krane, "Introductory Nuclear Physics", *John Wiley and Sons*, (1988)

[Kr00] A.T. Kruppa, "Shell corrections of superheavy nuclei in self-consistent calculations", *Phys. Rev.* C **61** (2000) 034313

[Ku93] A. Kuhnert *et al.*, "Search for an M0 transition in ^{170}Yb", *Phys. Rev.* C **47** (1993) 2386

[La96] G.A. Lalazissis, M.M. Sharma, P. Ring and Y.K. Gambhir, "Superheavy nuclei in the relativistic mean-field theory", *Nucl. Phys.* A **608** (1996) 202

[La01] I.H. Lazarus *et al.*, "The GREAT Triggerless Total Data Readout Method", *IEEE Transactions on Nuclear Science* Vol.**48** No.3 (2001) 567

[La04] I.H. Lazarus *et al.*, "The GRT4 VME Pulse Processing Card for Segmented Germanium Detectors", *IEEE Transactions on Nuclear Science* Vol.**51** No.4 (2004) 1353

[Le95] M. Leino *et al.*, "Gas-filled recoil separator for studies of heavy elements", *Nucl. Instr. and Meth.* B **99** (1995) 653

[Le90] I-Y. Lee, "The GAMMASPHERE", *Nucl. Phys.* A **520** (1990) 641c

[Le03] I-Y. Lee, M.A. Deleplanque and K. Vetter, "Developments in large gamma-ray detector arrays", *Rep. Prog. Phys.* **66** (2003) 1095

[Li88] R.M. Lieder *et al.*, "Study of band structures and crossings in ^{180}Os", *Nucl. Phys.* A **476** (1988) 545

[Li99] R.M. Lieder *et al.*, "Observation of a $(\nu 7/2^{-}[514])^2$ crossing in ^{180}Os", *Nucl. Phys.* A **645** (1999) 465

[Ma49] M.G. Mayer, "On closed shells in nuclei. II", *Phys. Rev.* **75** (1949) 1969

[Me24] L. Meitner, *Z. Phys.* **29** (1924) 169

[Me06] D.C. Meeker, "Finite Element Method Magnetics, Version 4.0.1 (03Dec2006 Build)", Website: $http://www.femm.info/$

[Me67] H. Meldner, *Ark. Fys.* **36** (1967) 593

[Me93] M.P. Metlay *et al.*, "The ICEBall: a multiple element array for in-beam internal conversion electron spectroscopy" *Nucl. Instr. and Meth.* A **336** (1993) 162

[Mi05] V. Mishra, V.D. Srivastava and S.K. Kataria, "Role of guard rings in improving the performance of silicon detectors", *Pramana -Journal of Physics* **65** No. 2 (2005) 259

[Ml79] M.S. Mladjenović, "Magnetic Electron Spectrometers and Their In-Beam Use", *Nucl. Instr. and Meth.* **162** (1979) 193

[Mo76] H. Morinaga and T. Yamazaki, "In-Beam Gamma-Ray Spectroscopy", *North-Holland* (1976)

[Mo66] S.A. Moszkowski, "Theory of Multipole radiation", in "Alpha-, Beta-, Gamma-Ray Spectroscopy" ed. K. Siegbahn, *North-Holland* (1966)

[Mö92] P. Möller and J.R. Nix, "Stability and decay of nuclei at the end of the periodic system", *Nucl. Phys.* A **549** (1992) 84

[Mö94] P. Möller and J.R. Nix, "Stability of heavy and superheavy elements", *J. Phys. G: Nucl. Part. Phys.* **20** (1994) 1681

[Mo07] S. Moon, *University of Liverpool, PhD thesis* (2007)

[Mo69] U. Mosel and W. Greiner, "On the stability of superheavy nuclei against fission", *Z. Phys.* **222** (1969) 261

[Ne66] J.H. Neiller and P.R. Bell, "The Scintillation Method", in "Alpha-, Beta-, Gamma-Ray Spectroscopy" ed. K. Siegbahn, *North-Holland* (1966)

[Ni55] S.G. Nilsson, *K. Dan. Vidensk. Selsk. Mat. Fys. Medd.* **29** (1955) 16

[Ni68] S.G. Nilsson *et al.*, "On the spontaneous fission of nuclei with Z near 114 and N near 184", *Nucl. Phys.* A **115** (1968) 545

[Ni69] S.G. Nilsson *et al.*, "On the nuclear structure and stability of heavy and superheavy elements", *Nucl. Phys.* A **115** (1968) 545

[No94] P.J. Nolan *et al.*, "Large Arrays of Escape-Suppressed Gamma-Ray Detectors", *Annu. Rev. Nucl. Part. Sci.* **45** (1994) 561

[Og00] Yu. Ts. Oganessian, "Route to Islands of Stability of Superheavy Elements", *Phys. of Atom. Nucl.* Vol. **63**, No.8 (2000) 1315

[Og04] Yu. Ts. Oganessian, "Superheavy elements", *Physics World* July 2004

[Og06] Yu. Ts. Oganessian *et al.*, "Synthesis of the isotopes of elements 118 and 116 in the ^{249}Cf and ^{245}m + ^{48}Ca fusion reactions", *Phys. Rev.* C **74** (2006) 044602

[Ol97] O. Olabisi, "Handbook of thermoplastics", *Marcel Dekker INC.* (1997)

[Pa03a] T. Page, *University of Liverpool, PhD thesis* (2003)

[Pa03b] R.D. Page *et al.*, "The GREAT spectrometer", *Nucl. Instr. and Meth.* B **204** (2003) 634

[Pa07] J. Pakarinen *et al.*, "Investigation of nuclear collectivity in the neutron mid-shell nucleus ^{186}Pb", *Phys. Rev.* C **75** (2007) 014302

[Pa09a] P. Papadakis *et al.*, "Towards combining in-beam γ-ray and conversion electron spectroscopy", ed. A. Blazhev, J. Jolie, N. Warr and A. Zilges, *AIP Conf. Proc.* , **1090** (2009) 14

[Pa04] A. Parkhomenko and A. Sobiczewski, "Proton One-Quasiparticle States of Heaviest Nuclei", *Act. Phys. Pol.* B **35** (2004) 2447

[Pa05] A. Parkhomenko and A. Sobiczewski, "Phenomenological Formula for α-Decay Half-Lives of Heaviest Nuclei", *Act. Phys. Pol.* B **36** (2005) 3115

[Pa89] Z. Patyk, A. Sobiczewski, P. Armbruster and K.-H. Schmidt, "Shell effects in the properties of the heaviest nuclei", *Nucl. Phys.* A **491** (1989) 267

[Pa91] Z. Patyk and A. Sobiczewski, "Ground-state properties of the heaviest nuclei analyzed in a multidimensional deformation space", *Nucl. Phys.* A **533** (1991) 132

[Pa95] E.S. Paul *et al.*, "In-beam γ-ray spectroscopy above ^{100}Sn using the new technique of recoil decay tagging", *Phys. Rev. C* **51** (1995) 78

[Pa09b] E.S. Paul, *private communication*,

[Pa10] E.S. Paul, *private communication*,

[Pu] V. Pucknell and S. Letts, "Multi Instance Data Acquisition System", Website: $http://npg.dl.ac.uk/MIDAS/$

[Ra08] P. Rahkila, "Grain-A Java data analysis system for Total Data Readout", *Nucl. Intsr. and Meth.* A **595** (2008) 637

[Re06] P.-G. Reinhard, M. Bender, W. Nazarewicz and T. Vertse, "From finite nuclei to the nuclear liquid drop: Leptodermous expansion based on self-consistent mean-field theory", *Phys. Rev.* C **73** (2006) 014309

[Re04] P. Reiter *et al.*, *Act. Phys. Hun.* **19** (2004) 127

[Re05] P. Reiter *et al.*, "Structure of Odd-A, Shell-Stabilized Nucleus $^{253}_{102}$No", *Phys. Rev. Lett.* **95** (2005) 032501

[Ri96] P. Ring, "Relativistic mean field theory in finite nuclei", *Rep. Prog. Part. Nucl. Phys.* **37** (1996) 193

[Ro49] M.E. Rose, "Internal Pair Formation", *Phys. Rev.* **76** (1949) 678

[Ro66] M.E. Rose, "Theory of Internal Conversion", in "Alpha-, Beta-, Gamma-Ray Spectroscopy" ed. K. Siegbahn, *North-Holland* (1966)

[Ro78] F. Rösel *et al.*, "Internal Conversion Coefficients for all Atomic Shells", *At. Data Nucl. Data Tables* **21**, (1978) 91

[Ro09] D.C. Rostron, *University of Liverpool, PhD Thesis* (2009)

[Ru97] K. Rutz *et al.*, "Superheavy nuclei in self-consistent nuclear calculations", *Phys. Rev.* C **56** (1997) 238

[Sc92] H. Schmidt-Böcking *et al.*, "δ-electron Emission in Fast Heavy Ion Atom Collisions", *Adv. Space Res.* **12** No. 2-3 (1992) 7

[Se95] R.W. Johnson, "Introduction to Hybrid Microelectronics", in "Hybrid Microelectronics Handbook" ed. J.E. Sergent and C.A. Harper, *McGraw-Hill*, (1995)

[Se06] A.P. Severyukhin, M. Bender and P.-H. Heenen, "Beyond mean field study of excited states: Analysis within the Lipkin model", *Phys. Rev.* C **74** (2006) 024311

[Sh99] S.L. Shepherd *et al.*, "Measurements on a prototype segmented Clover detector", *Nucl. Instr. and Meth. A* **434** (1999) 373

[Si46] K. Siegbahn and N. Svartholm, "Focusing of Electrons in Two Dimensions by an Inhomogeneous Magnetic Field", *Nature* **157** (1946) 872

[Si66] K. Siegbahn, "Beta-ray Spectrometer Theory and Design", in "Alpha-, Beta-, Gamma-Ray Spectroscopy" ed. K. Siegbahn, *North-Holland* (1966)

[Si80] R.S. Simon, "The Darmstadt-Heidelberg Crystal Ball", *J. de Phys.* **41** (1980) C10, 281

[Si86] R.S. Simon *et al.*, "Evidence for Nuclear Shape Coexistence in ^{180}Hg" *Z. Phys.* A **325** (1986) 197

[Si05] J. Simpson, "The AGATA Project" *J. Phys. G: Nucl. Part. Phys.* **31** (2005) S1801

[Sl51] L.A. Sliv, *Zh. Exp. Teor. Fiz.* **21** (1951) 770

[Sm78] R.A. Smith, "Semiconductors", *Cambridge University Press* (1978)

[Sm97] R. Smolańczuk, "Properties of the hypothetical spherical superheavy nuclei", *Phys. Rev.* C **56** (1997) 812

[Sm72] W.R. Smythe, "Definitions, Units, Nomenclature, Symbols, Conversion Tables", in "Electricity and Magnetism" ed. D.F. Bleil in the "American Institute of Physics Handbook" ed. D.E. Gray, *McGraw-Hill Book Company* (1972)

[So07] A. Sobiczewski and K. Pomorski, "Description of structure and properties of superheavy nuclei", *Prog. Part. Nucl. Phys.* **58** (2007) 292

[St01] J.V. Stewart, "Intermediate Electromagnetic Theory", *Worlds Scientific* (2001)

[St06] M.A. Stoyer, "Island ahoy!", *Nature* **442** (2006) 876

[St67] V.M. Strutinsky, " "Shells" in deformed nuclei" *Nucl. Phys.* A **122** (1968) 1

[St68] V.M. Strutinsky, "Shell effects in nuclear masses and deformation energies" *Nucl. Phys.* A **95** (1967) 420

[Ta32] H.M. Taylor and N.F. Mott, "A Theory of the Internal Conversion of γ-Rays", *Proc. R. Soc. Lond.* A **138** (1932) 665

[Ta33] H.M. Taylor and N.F. Mott, "A Theory of the Internal Conversion of γ-Rays. II", *Proc. R. Soc. Lond.* A **142** (1933) 215

[Tr90] W.H. Trzaska, "Recommended data on selected gamma-ray and conversion-electron calibration sources", *Nucl. Instr. Meth.* A **297** (1990) 223

[Tw84] P.J. Twin *et al.*, "First experiments with TESSA at Daresbury", *Il Nuovo Cimento* **81** A (1984) 219

[VF07] Vector Fields, "OPERA, Version 12",
Website: *http* : *//www.vectorfields.com/*

[Vl56] V.V. Vladimirskii, E.K. Tarasov and Yu.V. Trebuhovskii, *Prib. Tek. Eksp.* **1** (1956) 13

[Wa68] M. Waldschmidt and S. Wittig, "Backscattering and Bremsstrahlung of Electrons in a Silicon Detector", *Nucl. Instrum. Meth* **64** (1968) 189

[Wa99] P. Walker and G. Dracoulis, "Energy traps in atomic nuclei", *Nature* **399** (1999) 35

[We51] V.F. Weisskopf, "Radiative Transition Probabilities in Nuclei", *Phys. Rev.* **83** (1951) 1073

[Wi66] R. Wilson, "Internal Pair Formation", in "Alpha-, Beta-, Gamma-Ray Spectroscopy" ed. K. Siegbahn, *North-Holland* (1966)

[Wo92] J.L. Wood *et al.*, "Coexistence in even-mass nuclei", *Phys. Rep.* **215** (1992) 101